Electronic Theses and Dissertations, 2004-2019

2019

Investigation of Coastal Vegetation Dynamics and Persistence in Response to Hydrologic and Climatic Events Using Remote Sensing

Subrina Tahsin
University of Central Florida

INVESTIGATION OF COASTAL VEGETATION DYNAMICS AND PERSISTENCE IN RESPONSE TO HYDROLOGIC AND CLIMATIC EVENTS USING REMOTE SENSING

by

SUBRINA TAHSIN
BURP, Bangladesh University of Engineering and Technology, 2009
MSc, Florida International University, 2014
MSc, University of Central Florida, 2016

A dissertation submitted in partial fulfillment of the requirements
for the degree of Doctor of Philosophy
in the Department of Civil, Environmental and Construction Engineering
in the College of Engineering and Computer Science
at the University of Central Florida
Orlando, Florida

Summer Term
2019

Major Professor: Arvind Singh
&
Stephen C. Medeiros

ABSTRACT

Coastal Wetlands (CW) provide numerous imperative functions and provide an economic base for human societies. Therefore, it is imperative to track and quantify both short and long-term changes in these systems. In this dissertation, CW dynamics related to hydro-meteorological signals were investigated using a series of LANDSAT-derived normalized difference vegetation index (NDVI) data and hydro-meteorological time-series data in Apalachicola Bay, Florida, from 1984 to 2015. NDVI in forested wetlands exhibited more persistence compared to that for scrub and emergent wetlands. NDVI fluctuations generally lagged temperature by approximately three months, and water level by approximately two months. This analysis provided insight into long-term CW dynamics in the Northern Gulf of Mexico. Long-term studies like this are dependent on optical remote sensing data such as Landsat which is frequently partially obscured due to clouds and this can that makes the time-series sparse and unusable during meteorologically active seasons. Therefore, a multi-sensor, virtual constellation method is proposed and demonstrated to recover the information lost due to cloud cover. This method, named Tri-Sensor Fusion (TSF), produces a simulated constellation for NDVI by integrating data from three compatible satellite sensors. The visible and near-infrared (VNIR) bands of Landsat-8 (L8), Sentinel-2, and the Advanced Spaceborne Thermal Emission and Reflection Radiometer (ASTER) were utilized to map NDVI and to compensate each satellite sensor's shortcomings in visible coverage area. The quantitative comparison results showed a Root Mean Squared Error (RMSE) and Coefficient of Determination (R^2) of 0.0020 sr^{-1} and 0.88, respectively between true observed and fused L8 NDVI. Statistical test results and qualitative performance evaluation suggest that TSF was able to synthesize the missing pixels accurately in terms of the absolute magnitude of NDVI. The fusion improved the

spatial coverage of CWs reasonably well and ultimately increases the continuity of NDVI data for

long term studies.

ACKNOWLEDGMENTS

TABLE OF CONTENTS

LIST OF FIGURES

LIST OF TABLES

CHAPTER 1: INTRODUCTION

1.1 Background

Coastal wetlands (CWs) serve as a buffer zone between the uplands and the sea and include a variety of freshwater swamps and marshes, salt marshes, mud flats, mangrove swamps, rocky shorelines, sea-grass beds and sandy beaches (Michener et al., 1997). CWs are therefore among the most dynamic ecosystems on earth due to the regular interaction between coastal marine processes and land-based fluvial (Ericson et al., 2006). They provide valuable ecosystem services to millions of people worldwide (Webb et al., 2013) which include shoreline protection from storm surge, key commercial and recreational fishing, water quality enhancement by nutrient uptake and filtration (Chen et al., 2001). CWs also play a key role in buffering the effects of climate change, thereby supporting climate change adaptation and resiliency. CWs also sequester carbon (Y. Huang et al., 2010), provide habitats for diverse wetland plants and animals. In fact, vegetated and healthy CWs are among the most effective sinks for carbon on the planet (Moomaw et al., 2018). Their value to coastal economies and lifestyles is indispensable. However, they are one of those ecosystems that are most strongly impacted by even slight changes in the climate, particularly through sea level rise (SLR), decreased ground and surface water levels and subsequent deviations in hydrologic regimes. They are sensitive to meteorological, climatic and anthropogenic influences. Cumulative changes in temperature, precipitation, storm frequency, intensity, distribution and timing can have both direct and indirect effects on CWs and inland wetlands. Unfortunately, over the past 50 years, vast areas of CWs have been polluted, drowned, or eroded and as a result have declined in size and health (White & Kaplan, 2017; Yu et al., 2016).

Extreme hydrologic events (EHEs) such as hurricanes, flooding and droughts are increasing in frequency and intensity as a result of climate change (Konisky et al., 2016) while CWs are highly vulnerable to these types of hazards. Under widely accepted climate change projections, CWs are anticipated to experience longer duration and increased depth of inundation due to SLR, changes in distribution of freshwater inputs that are influenced by alteration in precipitation patterns and increased temperature (Schubel & Hirschberg, 1978).

However, there are variety of CWs types for example freshwater and salt-water wetlands (Klemas et al., 1993). Different types of wetlands adapt to climate change differently. A thorough analysis is required to understand the impact of these CWs against the EHEs. Large amounts of information including both spatial and temporal data are required in accurately capturing the spatio-temporal dynamics of CWs. Remote sensing (RS) has aided major advances in understanding CWs and their dynamics by quantifying internal processes and their interaction with spatio-temporal states of the atmosphere, land and ocean. For monitoring CWs, RS has many advantages including recurrent coverage for CWs to be monitored yearly, seasonally, even daily. It is especially appropriate for CWs monitoring in developing countries, where funds are limited and where little information is available on the areas, surrounding land uses and wetland losses over time (Ozesmi et al., 2002). In these inaccessible and ungauged areas, ground truth data is limited therefore techniques developed and refined elsewhere must be applied. Vegetation and water indices are generalizable and widely applicable classes of RS abstraction. Modern improvements in sensor design, evolution of newer generations of former satellites and advanced data analysis methods are making RS systems practical and attractive for monitoring natural and man-induced coastal ecosystem changes. Nevertheless, the relatively short durations of observation series, spatial data

discontinuity and data uncertainties still pose challenges for capturing the robust long-term trends within the ecosystem (Guo et al., 2017). Now it is high time to protect the CWs, which needs regular monitoring and mapping of large tracts of CWs, using existing RS data and computationally efficient yet cost-effective methods.

1.2   Coastal Wetland Types

Coastal wetlands have been classified by the National Oceanic and Atmospheric Administration (NOAA) Coastal Change Analysis Program (C-CAP). The C-CAP classified wetlands along the eastern seaboard and Gulf coasts of the United States. C-CAP is considered a reliable, integrated digital database that enables researchers to track development in coastal regions (Klemas et al., 1993).

C-CAP defines eight sub-classes of wetlands under three major classes. Palustrine wetland includes Palustrine forested wetland (PFW), Palustrine shrub/scrub wetland (PSW) and Palustrine emergent wetland (PEW). Estuarine wetland includes Estuarine forested wetland (EFW), Estuarine shrub/scrub wetland (ESW) and Estuarine emergent wetland (EEW). Submerged Lands includes both Palustrine aquatic bed and Estuarine aquatic bed. While the Estuarine wetland includes both wetlands and deep-water habitats, Palustrine wetland includes only wetland habitats (Cowardin et al., 1979).

All three Palustrine wetlands consisting of PFW, PSW and PEW- contain tidal and non-tidal wetlands in which salinity due to ocean-derived salts is below 0.5 percent. They vary by vegetation types and height generally. The forested type is dominated by woody vegetation taller than or equal to five meters in height and occur in tidal areas. The scrub type is also dominated by woody

vegetation less than five meters in height and are found in tidal areas. Species present range from true shrub, young trees and shrubs, to trees that are small or stunted due to environmental conditions. The emergent wetland type includes tidal and non-tidal wetlands controlled by emergent mosses, persistent emergent vascular plants, and all those wetlands occur in the tidal areas with below 0.5 percent salinity. Plants generally remain standing until the next growing season (NOAA, 2017).

Similar to the Palustrine wetland system, all three estuarine wetlands are situated in tidal areas where salinity due to ocean-derived salts is equal to or greater than 0.5 percent. The EFW is dominated by woody vegetation greater than or equal to five meters in height. The ESW includes all tidal wetlands dominated by woody vegetation and other wetlands less than five meters in height. The EEW includes erect, rooted, herbaceous hydrophytes (excluding mosses and lichens). These wetlands are present for most of the growing seasons in most years. Perennial plants usually dominate these wetlands (NOAA, 2017).

Palustrine aquatic bed contains tidal and non-tidal wetlands and deep-water habitats. This ecosystem's salinity is below 0.5 percent and is controlled by vegetation (i.e. algal mats, rooted vascular plant assemblages) growing and forming a continuous cover mainly on or at the surface of the water. Estuarine aquatic bed contains tidal wetlands and deep-water habitats where salinity is equal or greater than 0.5 percent. This ecosystem is dominated by plants that grow and form a continuous cover principally on or at the surface of the water. These include algal mats, kelp beds, and rooted vascular plant assemblages (NOAA, 2017).

1.3 Normalized Difference Vegetation Index (NDVI)

Phenological differences among terrestrial and CWs vegetation types, reflected in temporal differences in the Normalized Difference Vegetation Index (NDVI) derived from satellite RS data, have been used to map vegetation including land cover at continental scales. Theoretically, NDVI is an index used to characterize the reflective and absorptive features of vegetation in the red and near-infrared (NIR) portions of the electromagnetic spectrum which is calculated from a normalized transform of the NIR and red reflectance ratio. NDVI derived from Landsat has reasonable spatial resolution for many applications compared to other freely available satellite imagery. Landsat NDVI has many environmental applications including the ability to analyze changes in land use, transformation of urban heat islands, and impacts of EHEs. Landsat NDVI carries valuable information since 1984 regarding land surface properties for modeling terrestrial ecosystems on the global, continental, and regional scales. Such a long-time record is unique in the satellite RS community. Nevertheless, there are almost always disturbances in these time series, caused by sun glint, cloud contamination, atmospheric variability, and bi-directional effects. These disturbances greatly affect the monitoring of terrestrial and CWs ecosystems and show up as undesirable noise. Though the most often-used NDVI data sets are the post-processed 16-day Maximum Value Composite (MVC) products, they still include undesirable noise. Therefore, there is an ongoing requirement for methods for reducing noise and constructing high-quality NDVI time series data sets for further analysis in the scientific community to analyze NDVI and conduct research.

1.4 NDVI Application in Wetland Stress Analysis

Advances in RS techniques and advanced data analysis schemes are fetching cutting edge research methods to real world practice and enabling cost efficient, quantitative environmental analysis more accessible. For example, wetland extent mapping, canopy density and closure, leaf area index etc., are making the assessment of environmental parameters doable at regional scales. These great resources however bring new challenges. Managers responsible for environmental monitoring as well as ecosystem modelers are handling large uncertainties in data because of the varieties in season, weather, region and vegetation types. Having comprehensive and up to date information is crucial to optimize CWs and forest management throughout the season especially before and after extreme natural hazards.

NDVI mapping requires detailed imagery that abstracts a measure of the green vegetation existing in their study area. Time series analyses of the trend of greenness in vegetation can play a crucial role in identifying vegetation/CWs stress and relate the impact of hydrologic events. Long term impacts of extreme events on the ecosystem can range from small to massive, depending on the severity and duration of the event. A crucial component to time series analyses is establishing baseline characteristics of the study area so that changes can be identified. One such study was about Hurricane Andrew that made landfall in August 1992 in Louisiana. Researchers used Advanced Very High Resolution Radiometer (AVHRR) imagery which is coarse resolution to evaluate the impacted area of forested wetlands and their changes over time in Louisiana (Ramsey III et al., 1997). A time series of AVHRR images were transformed into NDVI time-series. The comparative analysis among three study sites in three forested wetland ecosystems validated the

anomalous phenology pattern in all sites resulting from the hurricane. NDVI time-series using the Airborne Visible/Infrared Imaging Spectrometer (AVIRIS) data showed salt marsh stress and recovery in Barataria bay, Gulf of Mexico after the deep-water horizon oil spill. Multifarious researches used different sensors or methods for vegetation mapping. Researchers need to select the sensor and method based on their goal about wetland stress detection.

1.5   Cloud Concerns in Optical Sensor Data

RS data has been used to detect and track the wetland dynamics at the local and regional scales. Multiple satellite sensors such as Landsat (Han et al., 2015; B. Tian et al., 2015), Moderate Resolution Imaging Spectroradiometer (Landmann et al., 2013), Formosat (B. Tian et al., 2015), and AVHRR (Ramsey III et al., 1997) provided processed data in the form of vegetation indices for this application.

Predicting missing data is a challenge for time-series analysis, especially optical sensor-based analysis, when the data is derived from satellite imagery. Landsat NDVI is not without the same problem. Missing data is inevitable due to the presence of thick clouds (Gordon & Wang, 1994). In warm coastal regions, water evaporation and frequent storms combine to produce cloud coverage and such analysis become more difficult. Cloud coverage hinders scientific research that depends on optical RS imagery. Moreover, observations are often incomplete because of sensor failure or outliers causing anomalous data. Therefore, it is important to carry out research on the filtering and gap filling of time series satellite images.

1.6 Machine Learning in Data Fusion and Prediction

Machine learning is recognized as one of the most promising technique now a days for quantitative information retrieval from remotely sensed images (C. Zhang et al., 2018). A series of machine learning methods have been evolved, such as support vector machines (SVMs) (Ghamisi et al., 2015), maximum likelihood (ML) (C. Zhang et al., 2018), neural networks (NNs) (W. Jiang et al., 2018), random forest (RF) (Berhane et al., 2018), and so on for data prediction. Among the various machine learning methods, NN-based classifiers gain superiority in terms of robustness, better classification performance and high data error tolerance (W. Jiang et al., 2018). When handling a complex dataset, multilayer perceptron (MLP) NNs (Taravat et al., 2015) are required, which feature more layers with a full connection between all neurons. MLP is designed to learn the nonlinear features, irrespective of their statistical properties, which is widely used in coastal wetland classification (Bao & Ren, 2011). Previous researchers successfully used sensor fusion among Landsat, MODIS, and Sentinel (Kulawardhana et al., 2007; Roy et al., 2008; Walker et al., 2012) while a lot of them utilized machine learning (Liu et al., 2018; Seo et al., 2018).

1.7 Scope of the Study

The current study performed a long-term CWs persistence analysis and explained the CWs dynamics with hydro-meteorological signals fluctuation as a key indicator for climate driven variations in CWs ecosystems. RS data collection and data pre-processing were a significant part of the research. Once the data were prepared, a set of research questions were addressed: Which CW types are more persistent in the temporal domain? Which hydro-meteorological factor has the highest impact on CWs resiliency? Is there a time-lag between the CWs response towards hydro-

meteorological factors forcing on them? Can Landsat pixels obscured by clouds be recovered? In an attempt to compare the resiliency of each wetland types, power spectral density (PSD) and cross-power spectral density (CPSD) were developed for each wetland type. All computation was derived with regard to seasonality removed time series. Seasonality was defined in the current study as monthly mean data over the whole time series. Such long-term study is heavily dependent on optical sensor that is subject to data loss due to cloud coverage.

After observing the limitations imposed on the analysis by cloudy pixels, the study further proposed a novel data fusion method using machine learning techniques based on multi-sensor data to repair missing NDVI values. The unique and novel method was named tri-sensor fusion (TSF). A total of 4 years of time series data were collected for the training and testing of the TSF model. While the TSF method improves spatial data coverage with reasonable accuracy, there were still missing pixels. Therefore, the current study went a step further and proposed a novel data fusion followed by data reconstruction method using RF machine learning techniques based on multi-parameter time series data to repair missing NDVI reflectance values. The unique and novel method was named Optical Cloud Pixel Recovery (OCPR). High spatio-temporal resolution raster-based temperature, precipitation, and spatial locations along with water levels from a nearby tide gage and corresponding month were selected as the feature vector (predictor) components associated with NDVI (label). To reconstruct cloud contaminated pixel values from the time-space-spectrum continuum, the RF machine learning tool was utilized. Approximately 30 years of time series data were collected for the training and testing of the OCPR model. All of these variables contained periods of missing data that were filtered out of the training and test data. RF is used to model the data distribution which is adapted to handle missing values. The RF, and linear

9

regression models, was assessed using the root mean square error (RMSE) between the reconstructed and the observed NDVI values in the test data set. The result is a robust, functioning model that can be used on Landsat as well as other satellite images worldwide, subject to further adjustment and testing.

CHAPTER 2: ASSESSING THE RESILIENCE OF COASTAL WETLANDS TO EXTREME HYDROLOGIC EVENTS USING VEGETATION INDICES: A REVIEW

Tahsin, S., Medeiros, S.C., & Singh, A. (2018). Assessing the Resilience of Coastal Wetlands to Extreme Hydrologic Events Using Vegetation Indices: A Review. Remote Sensing, 10(9), 1390.

2.1   Introduction

Coastal wetlands (CWs) stand as a highly productive buffer zone between the uplands and the sea and include a diverse assemblage of freshwater swamps and marshes, salt marshes, mangrove swamps, hyper-saline lagoons, mud flats, rocky shorelines, sandy beaches, and sea-grass beds (Hardisky et al., 1986; Michener et al., 1997). CWs provide numerous ecosystem services to millions of people worldwide (Webb et al., 2013). Some valuable ecosystem services provided by CWs include shoreline protection from storm surge, key commercial and recreational fishing, and water quality enhancement by nutrient uptake and filtration (Chen et al., 2001). They also sequester carbon (E. B. Barbier et al., 2011; Y. Huang et al., 2010; Langley & Megonigal, 2010) and provide habitats for wetland plants and animals. In addition, CWs are among the most productive and dynamic ecosystems on earth due to the frequent interaction between land-based fluvial and coastal marine processes (Ericson et al., 2006). Their value to coastal economies and lifestyles cannot be overstated. However, CWs are very sensitive to meteorological, climatic and anthropogenic influences. Cumulative changes in temperature and precipitation, storm frequency, intensity, distribution, and timing can have both direct and indirect effects on CWs and interior wetlands as well. Unfortunately, over the past 50 years, vast areas of CW have been polluted, drowned,

or eroded and as a result have declined in size and health (Guo et al., 2017; Sandhu et al., 2016; White & Kaplan, 2017; Yu et al., 2016).

Extreme hydrologic events (EHEs) such as hurricanes, flooding, and droughts are increasing in frequency and/or intensity as a result of climate change (Konisky et al., 2016). CWs are highly vulnerable to these types of hazards. Under widely accepted climate change projections, CWs are expected to experience increased depth and duration of inundation due to sea level rise (SLR), changes in distribution and intensity of fluvial freshwater inputs that are influenced by changes in precipitation patterns, and increased temperature (Scavia et al., 2002; Schubel & Hirschberg, 1978).

Accurately capturing the spatio-temporal dynamics of CWs requires vast amounts of information. In this context, vast indicates quantity in both space and time. Remote sensing (RS) has enabled major advances in understanding CWs and their changes by quantifying internal processes and their interaction with spatio-temporal states of the atmosphere, land and ocean. For monitoring CWs, RS has many advantages. RS data have recurrent coverage for CWs to be monitored seasonally or yearly. RS is especially appropriate for CW inventories and monitoring in developing countries, where funds are limited and where little information is available on the areas, surrounding land uses, and wetland losses over time (Ozesmi et al., 2002). In these inaccessible areas, ground truth data is limited therefore techniques developed and refined elsewhere must be applied. Vegetation and water indices are prominent examples of generalizable and widely applicable classes of remote sensing abstraction. Modern improvements in sensor design and advanced data analysis techniques are making RS systems practical and attractive for monitoring

natural and man-induced coastal ecosystem changes. Nevertheless, the relatively short durations of observation series and their uncertainties still pose challenges for capturing the robust long-term trends within the landscape (Abed-Elmdoust et al., 2016; Singh et al., 2015) and ecosystem (Guo et al., 2017).

Here we present a literature review of contemporary RS platforms and their associated index products to investigate CW dynamics. RS technology has been used in both coastal and inland wetland research areas such as land use/cover changes, wetland classification (Barbier et al., 2011; Chen et al., 2001; Ericson et al., 2006; Y. Huang et al., 2010; Langley & Megonigal, 2010) and hydrologic processes in wetlands (Day et al., 2008; Nicholls & Cazenave, 2010; Wilcox & Whillans, 1999). However, the existing work is curated to synthesize the most relevant and current trends in RS technology for CW change detection, particularly in response to EHE impacts utilizing RS derived vegetation indices. Therefore, the objectives of this paper are to: (1) present an overview of the threats from EHEs on CWs; (2) highlight different types of RS tools to monitor CW changes using RS-derived indices due to hurricanes, droughts and floods; (3) present contemporary RS approaches (using lower level sensor data rather than abstracted indices) to monitor EHE impacts on CWs and (4) provide suggestions for future research in this area.

2.2   Threat Profile for Extreme Hydrologic Events on Coastal Wetlands

Coastal wetlands collectively include marshes, mangroves, forested wetlands, and estuaries. Survival of CWs depends largely on their ability to adapt and recover from EHEs and in addition to acute and long-term anthropogenic impacts. Once again, the EHEs referenced here include coastal flood/storm surge, hurricane, and drought that cause geophysical changes to the landscape.

The particular changes driven by EHEs include geomorphology (sediment deposition and erosion), geochemical (concentration or dilution of salinity), and biologic (damage and destruction of vegetation, transport and deposition of invasive species). Wilcox, 1999 (Wilcox & Whillans, 1999) found that local scale geomorphic changes such as sedimentation altered wetland hydro-period and internal creek depth. Day et al. (Day et al., 2008) provided a hierarchy of hydrologic pulse events ranging from daily tides, weekly sediment deposition to long term river channel major changes that affected the sustainability of various CWs. Meteorological changes in wetlands such as area change, topographical alteration along with sea level rise, storms, sedimentation, and changing freshwater input can directly impact coastal and estuarine wetlands. The synergistic biological processes can also influence these physical impacts and geomorphological changes to CWs resulting in unanticipated outcomes for the ecosystem (Day et al., 2008).

A 2002 review of the marine resource literature summarized the potential impacts of natural events on coastal wetlands, shorelines, and estuaries (Scavia et al., 2002). The assessment considered several key visible effects of climate change such as SLR, alterations in precipitation patterns and subsequent delivery of freshwater, increased ocean temperature, and changes in frequency and intensity of coastal storms. Global sea levels are documented to have continuously risen through the 20th century and this is projected to accelerate through the 21st century due to global warming. The increase in water temperature along with changes in freshwater delivery and coastal hydro-periods have the potential to alter the trophic state of CW (Nicholls & Cazenave, 2010). Although these impending impacts from climate change will vary in magnitude across CW types, the synergistic intensification of these impacts could trigger other ecosystem stresses such as coastal pollution, habitat destruction, and irrecoverable physical damage (Scavia et al., 2002).

Tahsin et al. (Tahsin et al., 2016) conducted a study in 2016 of the CW system in Apalachicola Bay, Florida. This area has experienced several tropical cyclones and droughts in 2005, 2009 and 2012-2013. Another study was conducted to evaluate the impact of hurricane Andrew on CWs in Louisiana (Cahoon et al., 1995). Both of these studies suggest that marshes and forested wetlands that are less salt tolerant are particularly vulnerable to storm surge impacts. During Hurricane Andrew in Louisiana, large amounts of sediment moved into marshes and low salinity areas and suppressed vegetation. Salinity introduced into fresh water ecosystem zones from the storm surge resulted in salt burn (Cahoon et al., 1995). Similar vegetation suppression was observed in Apalachicola Bay during the hurricane season of 2004-2005 (Tahsin et al., 2016). Although freshwater wetland plants re-establish in three months to a year, more frequent and larger magnitude storms are likely to dampen recovery of these freshwater wetlands and threaten their long-term resilience (Cahoon et al., 1995).

Table 2.1 summarizes potential threats posed by EHEs and also documents recommended methods against the threats. Note that anthropogenic disturbances are not considered in this study and will be a subject of future research. EHEs were arranged according to the change type occurred in landscape.

Table 2.1: Summary of Threats in Coastal Wetlands and Recommended Actions for Recovery

Threat Types	Brief Description	Recommended methods
Extreme events- Meteorological Changes		
Wetland acreage decrease	SLR (Assembled with human activities)	Wetland protection, restoration (removing exotic plants, removing bulkheads and fill, elevation grading, creating flushing channels, and planting native vegetation) and improvement of stressed systems (Klemas, 2013b)
Wetland shrinkage	SLR converts CW into open water	Artificial wetland creation, conservation of potential migration areas (Kentula, 2015)
Surface elevation of CW cannot keep pace with SLR	SLR threatens coastal salt-marshes and mangrove forests	Coastal climate change adaptation policy and expansion of monitoring (Webb et al., 2013)
Topographically alteration in the Watershed	Alterations can damage the natural hydrology of watershed area, including concentration pits, terraces, diversions, stream channelization, ditches, and others.	New Wetland Creation; Channel Excavation or Backfill (Kentula, 2015).

Geomorphological Changes		
Alteration of CW's geomorphology	Intense and frequent hurricanes, SLR, changes in sediment, nutrient inputs and freshwater	Changes in human behavior for dependency on wetland (Chen et al., 2001)
Sediment accumulation	Culturally-accelerated sedimentation alters the natural depths and hydro-periods of wetlands	Filled Wetland Construction (Wilcox & Whillans, 1999);
Biological Changes		
Invasive species	Intrusion of invasive species can reduce habitat diversity	Biological Removal; Prescribed burn; (Wilcox & Whillans, 1999)

2.3   Remote Sensing Vegetation Indices Used to Monitor EHEs Impacts

Scientists and engineers have developed indices for quantitatively and qualitatively evaluating vegetation cover, vigor, and growth dynamics using spectral measurements. Vegetation indices (VI) have been derived using multiple airborne and satellite platforms, including a recent increase in the use of data acquired by Unmanned Aerial Systems (UAs). To the best of authors' knowledge, there is no integrated mathematical expression to unify all VIs because of the use of different light spectra combinations, platforms, and resolutions. Therefore, customized algorithms tried over a variety of applications expressed in specific mathematical frameworks have been developed. To obtain proxy quantifications of the vegetation surface, the frameworks often use visible light

reflectance, mainly red and green spectral regions, from vegetation, and combine it with nonvisible

spectra such as near infrared (Xue & Su, 2017). However, while each VI is developed using

specific techniques, the end user (ecologist, coastal engineer, geographer) bases their decision on

the attributes of their particular use case such as target, spatial and temporal resolution

requirements, and desired deliverables (see Table 2.2). Therefore, remote sensing scientists and

engineers would be well served by involving end users in research projects from the start in order

to identify and meet their needs.

Table 2.2 List of Remote Sensing (RS) systems derived vegetation indices (Via) used in past studies on coastal wetland (CW) resiliency under extreme hydrologic events (EHEs) driven impacts

Index	RS System/ Images	Spatial Resolution (m)	Research Topics	Image used	References
			EHE – Hurricane		
NDVI	Landsat-5	30 m	Impacts of Hurricane Katrina at 2005 at coastal vegetation at Weeks Bay Reserve and surrounding area of coastal AL	3 Images -before landfall, -after landfall, -8 months after landfall	(Rodgers et al., 2009)
NDVI	MODIS-Terra	1 km	Recovery rate of mangrove after the two major hurricanes in South Florida	10 years (2001 to 2010) time series	(Y. Wang, 2012)

Index	RS System/ Images	Spatial Resolution (m)	Research Topics	Image used	References
NDVI	AVHRR	1.1 km	To assess the impacted area of forested wetlands at Louisiana	2 years (1991-1993) time-series between June and November, plus a Composite image during 1993 June	(Ramsey III et al., 2001)
SR, NDVI, ARVI, SAVI, SARVI, EVI	Landsat - MSS, TM, ETM+, OLI; ASTER; AVHRR; MODIS; SPOT; SENTINEL -2 MSI	Multiple (30 m 15 m, 1.1 km 1 km 10 m 20 m)	Biomass mapping of a marsh CW		(Mo et al., 2018)
NDVI	Landsat 5 and 7	30 m	CW resilience under EHEs from 1984 to 2015 at Apalachicola Bay	30-year time-series	(Tahsin et al., 2016)
EVI	MODIS	1 km	The temporal severity of disturbance caused by hurricane Maria compared to other events	17-year (2000-2017) time-series	(Feng et al., 2018)
EVI	MODIS-Terra and Aqua	250 m	Hurricane Dean (August 2007) damage map to the forests in the Yucatán Peninsula of Mexico	Pre-hurricane EVI composites: 20 July (Aqua), 28 July (Terra),	(Rogan et al., 2011)

Index	RS System/ Images	Spatial Resolution (m)	Research Topics	Image used	References
				5 August (Aqua), 13 August (Terra). Post-hurricane composites: 21 August (Aqua), 29 August (Terra), 6 September (Aqua), 14 September (Terra) 22 September (Aqua).	
mNDVI	AVIRIS	20 m	To investigate the ability of the saltmarshes in Barataria Bay, Louisiana, USA, to recover hurricane Isaac in 2012	3 images -14 September 2010 (Deepwater Horizon oil spill) -15 August 2011 -19 October 2012 (Hurricane Isaac)	(Khanna et al., 2017)
NDII	MODIS	1 km	Identify and estimate forest damage impacted by Hurricane Katrina	3 years (2003-2006) time series of vegetation indices Total 24 images were available	(Wang et al., 2010)

Index	RS System/ Images	Spatial Resolution (m)	Research Topics	Image used	References
			EHE – Drought		
VCI	AVHRR	1.1 km	Detect drought onset and measure the intensity, duration, and impact of drought	5-year (1985–1990) time-series	(Kogan, 1995)
VCI, PDSI, SPI, percent normal, deciles	AVHRR	8 km	Monitoring drought at Texas	Images of 18 growing-seasons (March to August 1982–1999)	(Quiring & Ganesh, 2010)
NDVI	MODIS	250 m	agricultural drought monitoring and early warning system for the farmers	10 years (2002-2012) monthly	(Sruthi & Aslam, 2015)
NDVI, EVI, NDWI, LST.	MODIS	1 km and 0.5 km	impacts of the 2009/2010 drought in southwestern China on vegetation	4 sets of 11 years (2000-2011) time-series	(Zhang et al., 2017)
VIUPD derived VCI	MODIS	250 m	longer-term drought monitoring, such as agricultural droughts	2011 (April–October)	(Jiao et al., 2016)

			EHE – Flood		
N/A	K-band radar images	N/A	standing water is present beneath the vegetation canopies		(Waite & Macdonald, 1971)
N/A	SAR	N/A	Flood detection in wetland with a limited number of scenes	limited scenes after 29 August 2005	(Kiage et al., 2005; Rykhus & Lu, 2005)
N/A	IRS LISS III, 1999 and Landsat TM, 1995	Multiple (2.5 m; 30 m)	mapping the flood-affected areas in Koa catchment, Bihar	Landsat TM: -27 May 1995 -18 October 1995 IRS-1C LISS III: -March 1999 -December 1999	(Jain et al., 2005)
NDWI	Landsat TM, ETM+	30 m	to identify flood inundated in New South Wales	21 years (1989–2010) time-series data: Landsat 5 TM and Landsat 7 ETM+ images	(Thomas et al., 2015)
mNDWI	LANDSAT	30 m	spectral analysis for flooded area prediction		(Ho et al., 2010)

More than 100 VIs are currently in use (Xue & Su, 2017). Again, with the use of high resolution spectral instrumentation in remote sensing, the number of available channels is increasing, while their bandwidth is getting narrower (Honkavaara et al., 2013). One index calculated from multispectral information is the normalized ratio between the red (R) and near infrared (NIR) bands, known as the Normalized Difference Vegetation Index (NDVI) (Karnieli et al., 2010), that characterizes canopy growth or vigor. Among the earliest basic VIs, Ratio Vegetation Index (RVI), Difference Vegetation Index (DVI), and NDVI depend on R and NIR bands, while Perpendicular Vegetation Index (PVI) depends on soil reflectance and vegetation reflectivity. These VIs have limitations, mainly attributed to sensitivities to sparse vegetation (RVI, PVI); soil background (DVI, NDVI, PVI) (Major et al., 1990); and atmospheric effects (NDVI). Later, new VIs was developed to address different issues. For example, Atmospherically Resistant Vegetation Index (ARVI) has been developed to account for atmospheric effects and Transformed Soil-Adjusted Vegetation Index (TSAVI), Soil-Adjusted Vegetation Index (SAVI), and modified SAVI (MSAVI) were established to account for the effect of soil background. Different environments have their own complex characteristics so for practical applications; the suitability of a particular VI must be scrutinized for the target scenario. To assist in that determination, we present a review of recent studies on VIs used to monitor EHE driven impacts such as hurricane, drought and flood in CWs. There is also a category of studies that used RS spectral information or primary data directly to identify EHE impacts, which will be discussed in the following section.

2.3.1   Vegetation indices to assess hurricane impacts in coastal wetlands

2.3.1.1 Normalized Difference Vegetation Index Derived Studies

Extreme hydrologic events play a central role in the dynamics of CWs. NDVI is one of the most widely used VIs to monitor plant growth and vegetation cover and thus it is a good candidate to assess long term CW changes. Both medium (LANDSAT (Rodgers et al., 2009)) and coarse resolution (Advanced Very High Resolution Radiometer (AVHRR)) (Ramsey III et al., 1997), MODIS (Ramsey et al., 2011)) satellite remote sensors have been used successfully in the past providing CW changes or recovery from hurricanes. For example, medium resolution Landsat 5 NDVI data were obtained to investigate coastal vegetation changes before and after Hurricane Katrina in 2005 for the Weeks Bay Natural Estuarine Research Reserve (NERR) and surrounding areas of coastal Alabama. Three NDVI images for selected dates before landfall (March 24, 2005), after landfall (September 16, 2005), and 8 months after landfall (April 28, 2006) showed that the NDVI values of coastal emergent wetland continued to decrease by 27% from September 2005 to April 2006 indicating prolonged hurricane damage in the study area (Rodgers et al., 2009). NDVI is often used to determine the effects of hurricanes on CW, including mangrove ecosystems that can vary from minor defoliation of a few trees to disastrous blow-down of an entire stand. An NDVI time series from 2001 to 2010 with an 8-day interval derived from the coarse resolution satellite image MODIS Terra to detect the recovery rate of mangrove after the two major hurricanes in South Florida. They found that it took around 2 to 3 years for mangrove ecosystem to recover to their phonological tempos (Y. Wang, 2012).

In August 1992, Hurricane Andrew made landfall in Louisiana and provided researchers the opportunity to use the coarse resolution AVHRR imagery to assess the impacted area of forested wetlands in Louisiana (Ramsey III et al., 1997). To better understand the phenology, a time series of AVHRR images were transformed into NDVI. The comparative analysis among three study sites (Site 1: a fairly open canopy; Site 2, a hardwood area; and Site 3, a hardwood area with the highest canopy closure) in the Atchafalaya Basin validated the anomalous phenology pattern of all sites in 1992 resulting from the hurricane. The differences in damage across three sites were correlated with the forest canopy structure. A recent study using VIs at multiple spatial resolutions, closely monitored the vulnerability of coastal marshes in Louisiana (Mo et al., 2018). They found that linear models derived from NDVI and Enhanced vegetation index (EVI) are most effective for assessing Leaf Area Index (LAI). They studied various optical remote sensors including Landsat MSS, TM, ETM+, and OLI; ASTER; AVHRR; MODIS; SPOT, and SENTINEL-2 multispectral instrument (MSI) derived VIs such as Simple Ratio (SR), NDVI, ARVI, SAVI, Soil and Atmosphere Resistant Vegetation Index (SARVI), and EVI. The study also highlighted the effect of spatial resolution on biomass mapping of CW and found that sensors with high spatial resolution are preferred for mapping biomass in areas with dense water networks and areas along shorelines.

2.3.1.1.1   A Case-study of CW dynamics: 30-year Landsat NDVI time-series analysis to monitor EHE impacts

The health and vigor of the vegetation in the lower marshes of Apalachicola Bay have been detectably altered as a result of hurricanes and droughts. These changes were illustrated in an

analysis of 15 years of NDVI data for this region. Tahsin et al. derived NDVI derived using Landsat 5,7 and 8 sensors from 2000 to 2015 and investigated the external stresses incurred by hurricanes and droughts on Saltwater Wetland (SWW), Freshwater Forested Wetland (FFW), and Freshwater Emergent Wetland (FEW) ecosystems using both annual averaged and monthly NDVI from 1984 to 2000. The CW ecosystem boundary was consolidated from the 23 wetland classifications of the National Oceanic and Atmospheric Administration (NOAA) Coastal Change Analysis Program (C-CAP) down to 3 the classes of wetlands mentioned above. Probability density functions (PDF) and NDVI difference computations against each year showed that SWW was more resilient than the other two ecosystems (Tahsin et al., 2016).

Using the same data set, we generated Figure 2.1 to demonstrate the spatial NDVI variability averaged annually, from 2001 to 2015. Low NDVI values represent wetland with less greenness; high NDVI values represent wetland with more greenness. While 2002 was a regular non-event year, 2004 and 2005 had significant storm surges from Hurricanes Frances, Ivan and Dennis. 2012 was classified as a drought year (Hatter, 2015). The mean annual NDVI values in the study area were found to be 0.52, 0.49, 0.34 and 0.41 in 2002, 2004, 2005 and 2012, respectively. The aftermath of each hurricane mentioned above was observed for a year from the month it made landfall. 2004 and especially 2005 showed the least greenness or most stress for CW in Apalachicola Bay due to repeated hurricane strikes. Drought also impacted the average NDVI range in 2012-2013.
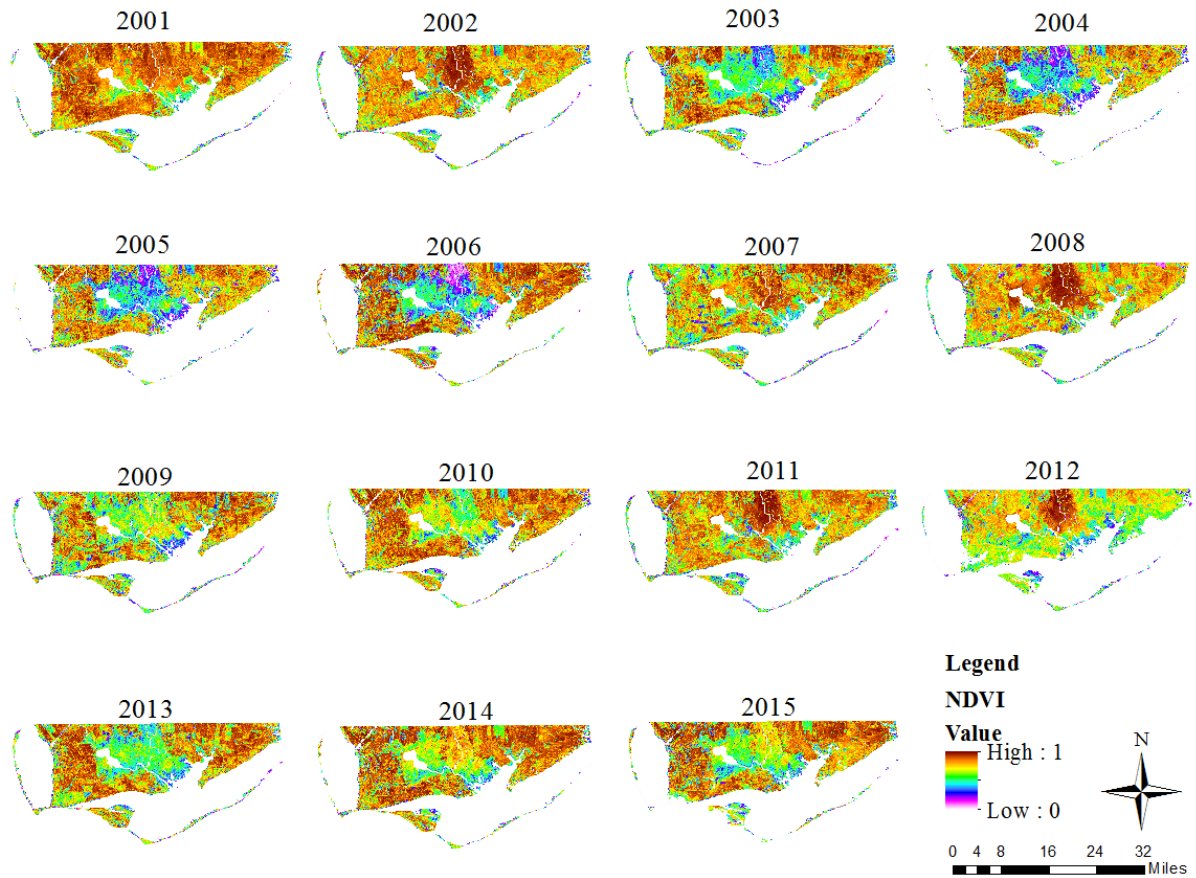
Figure 2.1: Temporal pattern of annual averaged NDVI from 2001 to 2015. Low NDVIs were observed during 2003-2005 (known hurricane years), 2009 (known hurricane year) and 2012-2013 (known drought and tropical storm years)

In this paper, we extended the Apalachicola Bay NDVI time-series back by an additional fifteen years from 1984 to 1999; bring the temporal extent of the data to 30 years. The data are similar except that the ecosystems were previously reclassified into three classes, based on the relatively minor differences between the two freshwater classes; they were now reclassified into two: saltwater wetland (SW) and freshwater wetlands (FW). FWs are the dominant type in the study

27

area and are characterized by woody vegetation that is 6 m tall or taller. All hydro period regimes were included except sub tidal. This rough categorization is important since each wetland type has different "typical" NDVI ranges. To illustrate this, the monthly average NDVI were computed for both wetland types from 1984 to 2015 and the results are shown in
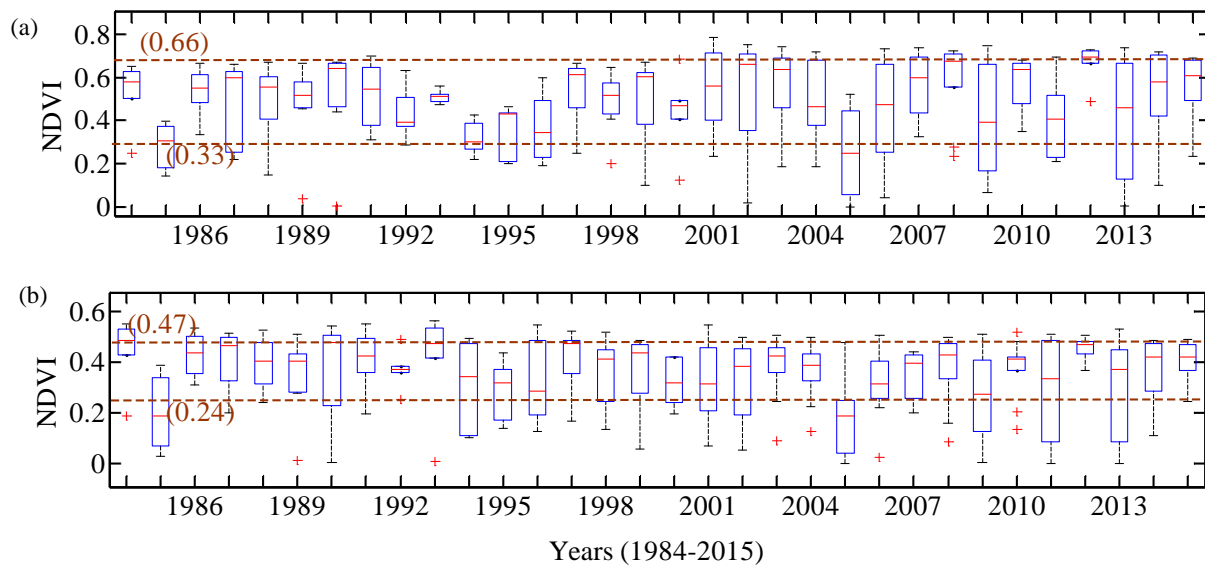
Figure 2.2: Boxplots of 30 Years of Vegetation Dynamics (NDVI) at Apalachicola Bay for the Freshwater Wetland (FW) (a) and Saltwater Wetland (SW). Horizontal line (red line) in a and b, in each box indicates median demarcating 50% data either above or below the median whereas the dashed (brown) horizontal lines represent the average 25th and 75th percentiles for the two types of the wetlands studied here (corresponding percentile values are written inside parenthesis adjacent to the dashed brown lines)

Figure 2.2 shows the extension of the previous work to include 30 years of CW dynamics at Apalachicola Bay during repeated EHEs. 25th percentile NDVI values were calculated for both FW and SW which are 0.33 and 0.24, respectively. Figure 2.2 also note that the data ranging from 2000-2015 has all months of data from January to December while data ranging from 1984-2000 has several months of missing data in each year. The data gaps caused by cloudy/missing data may

have resulted in a narrower range of box plots for some years from 1984 to 2000. For example, 1992 has only 6 months of data for both FW and SW.

The time series in Figure 2.2 indicates that NDVI of both FW and SW were below the 25th percentile range during 1985, 1994, 1995, 1996, 2005, 2007, 2009, 2011-2012, 2013 suggesting wetland stresses in those years. Apalachicola Bay was impacted by Hurricane Elena, Hurricane Dennis, Hurricane Claudette in 1985, 2005 and 2013, respectively. Tropical storms followed by flood impacted Apalachicola Bay during 1994-1996, and droughts were intermittently observed from 2011-2013 (Leitman et al., 2016). Note that Tahsin et al. (Tahsin et al., 2016) reported similar findings regarding NDVI dynamics showing drops at 2005, 2009 and 2011- 2012.

2.3.1.2 Enhanced Vegetation Index Studies

EVI is a vegetation index that enhances the vegetation signal in areas with high biomass. Using MODIS Near InfraRed (NIR), Red (R) and BLUE (B) surface reflectance, EVI can be expressed as equation 2.1.

$$EVI = \frac{G \times (NIR-R)}{(NIR + a \times R - b \times B + L)} \qquad (2.1)$$

The coefficients adopted in the MODIS-EVI algorithm are; L (Canopy background adjustment factor) =1, a = 6, b = 7.5, and G (gain factor) = 2.5 (Justice et al., 1998). A time series of MODIS EVI (from 2000 to 2017) was produced over Puerto Rico to determine the severity of the disturbance caused by Hurricane Maria compared to other events over the same period (Feng et al., 2018). Analysis of the MODIS EVI vegetation index demonstrated a steep decline in vegetation greenness outside of the historical range since 2000 when compared with September 13th (post

Hurricane Irma), with a much steeper decline in at September 29th (post Hurricane Maria). Wang and D'Sa in 2010 (Wang & D'Sa, 2010) revealed the usefulness of MODIS EVI product for long-term CW monitoring after a hurricane disturbance in Mexico. Also, the EVI product can detect both disturbed and non-disturbed CW by the hurricanes. Using MODIS EVI product again, another study mapped Hurricane Dean (August 2007) damage to the forests in the Yucatán Peninsula of Mexico using a two-step vetting procedure. Capitalizing on the favorable timing of the MODIS Aqua EVI compositing, relative to the hurricane event, they revealed highest damage detection ranging from 95% (Saffir–Simpson hurricane wind scale zone 5) to 87% (zone 3) (Rogan et al., 2011). A comparative study between MODIS and Landsat TM VIs illustrated that Landsat TM-derived NDVI imagery was more sensitive to terrain properties than EVI. However, both indices either under or over-estimated VI values in areas of steep topography, especially when the sun elevation angle was less than 40° (TM images). An additional limitation of TM imagery is that fewer cloud-free images are typically available compared to MODIS composite images. Also, MODIS NDVI outperforms MODIS EVI in areas of steep topography particularly during seasons with poor viewing geometry (Matsushita et al., 2007; Sesnie et al., 2012).

2.3.1.3 Soil Adjusted Vegetation Index (SAVI) Studies

SAVI was developed as a modification of NDVI to account for the influence of soil brightness when vegetative cover is low (Huete, 1988). In response to the need for effective restoration of threatened estuarine wetlands in the Gulf Coast, a study for mapping biophysical health of the area was initiated. The study used multiple VIs consisting NDVI, EVI, SAVI, Chlorophyll Index (CIred), Wide Dynamic Range Vegetation Index (WDRVI), and Visible Atmospheric Resistant

Index (VARI) utilizing reflectance at Red and NIR bands for MODIS. Another study aimed to generate a remote sensing model of coastal marsh aboveground biomass density to represent nationally diverse tidal marshes within the conterminous United States (Byrd et al., 2018). Using the random forest machine learning algorithm, imagery from multiple sensors including Sentinel-1 C-band SAR, Landsat, and the National Agriculture Imagery Program (NAIP), the model performance was improved. SAVI was identified as the most important VI among the six Landsat VIs that successfully predicted biomass density for a range of marsh plants.

2.3.1.4 Other VIs Derived Studies

Among other VIs, a recent study by Khanna et al. used a modified NDVI (mNDVI) to evaluate the recovery of the salt marshes in Barataria Bay, Louisiana, USA, after Hurricane Isaac in 2012 and the Deepwater Horizon oil spill in 2010 (Khanna et al., 2017). In 2012, after Hurricane Isaac, there was a significant loss of green vegetation to water, soil and non-photosynthetic vegetation (NPV) in both oiled and oil-free sites. Also, vegetation in narrow stands of the Bay was considerably more stressed than vegetation in block stands. Another study developed an approach for identifying and estimating forest damage from Hurricane Katrina (Wang et al., 2010). The statistical analysis and comparison with the damage severity revealed that Normalized Difference Infrared Index (NDII) was an optimal indicator for detecting hurricane-induced forest damage among the five commonly used VIs, including NDVI, EVI, NDII, LAI and Fraction of Photosynthetically Active Radiation (FPAR).

2.3.2 RS systems and indices to monitor drought impacts

According to the American Meteorological Society, a meteorological drought is defined by the magnitude (with respect to normal) and duration (e.g., weekly, monthly, seasonal, or annual time scales) of a precipitation deficit (Orville, 1990). Many drought indices have been developed for monitoring drought conditions due to their importance in assessing agricultural and wildfire risks (Quiring, 2009). Satellite image-based drought indices such as the NDVI-based Vegetation Condition Index (VCI), have proven to be useful for detecting drought onset and measuring the intensity, duration, and impact of drought in regions around the world (Ji & Peters, 2003; Kogan, 1995; Seiler et al., 2000). Mo et al. (Mo et al., 2017) used Landsat-derived NDVI and field-based environmental data during the past 30 years to study the drought-associated phonological changes of Louisiana coastal marshes. They found correlation between drought in southeast Louisiana and La Niña. They also pointed out the sensitivity of saline marshes to drought. Another study applied change analysis method using high-resolution IKONOS and WorldView-2 satellite imagery to identify the annual rates of change from mudflat to vegetation in a coastal wetland (Tidal march) restoration area. Not only the effects of wet years and drought, the trends of the vegetation in that tidal marsh area were likely influenced by a combination of other factors such as sedimentation rates (Chapple & Dronova, 2017).

A number of researches used satellite image-derived VIs for drought monitoring other than coastal wetlands that paved the path to use the VIs for drought monitoring in CWs as well. For example, the combination of MODIS derived NDVI as well as Land surface temperature (LST) provided very useful information for agricultural drought monitoring and early warning system for farmers

(Sruthi & Aslam, 2015). Zhang et al. (Zhang et al., 2017) examined the impacts of the 2009/2010 drought in southwestern China on vegetation by calculating the standardized anomalies of NDVI, EVI, Normalized Difference Water Index (NDWI), and LST. The indices were derived by MODIS satellite images. The results implied that the NDVI, EVI, and NDWI declined, while LST increased in the 2009/2010 drought-stricken vegetated areas during the drought period. Zi and Peters, (Ji & Peters, 2003) established that while NDVI is a useful variable for monitoring vegetation conditions, the nature of the relationship between the NDVI and drought conditions varies based on the seasonal timing and variations in vegetation and soil type (Ji & Peters, 2003).

2.3.3   RS systems and indices to monitor flood impacts

Flood impacts resulting from heavy rainfall, storm surge and drainage system failures are regularly experienced in coastal and inland areas. Remote sensing has played an important role in characterizing these hazards and assessing their effects. Waite and MacDonald first spotlighted flooded forests during "leaf off" conditions in Arkansas where they showed up as anomalously bright areas on K-band Radio Detection and Ranging (Radar) images (Waite & Macdonald, 1971). During that time, many studies relied on the fact that when standing water is present beneath the vegetation canopies, the radar backscattering signal changes with water level, depending on vegetation type and structure. Therefore, they used SAR backscatter to monitor temporal variations in the hydrological conditions of wetlands, including floods (Bourgeau-Chavez et al., 2005; Costa, 2004; Costa et al., 2002; Grings et al., 2006; Hess et al., 1995; Kiage et al., 2005). Previous studies using satellite SAR imagery over coastal Louisiana were focused on flood detection in wetlands with a limited number of scenes (Kiage et al., 2005; Rykhus & Lu, 2005). A study on the Louisiana

coast investigated the feasibility of using Radarsat-1 SAR imagery to detect flooded areas in coastal Louisiana after Hurricane Lili, October 2002. Arithmetic differencing and multi-temporal enhancement techniques were employed to detect flooding and investigate relationships between backscatter and water level changes (Kiage et al., 2005).

Jain et al. (Jain et al., 2005) mapped the flood-affected areas in Koa catchment, Bihar in India using remote sensing satellite data (IRS LISS III, 1999 and Landsat TM, 1995). They derived water indices using image processing techniques and indicated that a NDWI based approach was able to identify flood inundation. NDWI derived from Landsat TM and ETM+ images were also used to map the inundation in New South Wales, Australia (Thomas et al., 2015). Another study generated a flood inundation map using a geomorphologic approach employing Shuttle Radar Topographic Mission (SRTM) DEM and satellite image data (ASTER and Landsat). They integrated both landform classification and spectral analysis for flooded area prediction by applying modified NDWI (MNDWI) and elevation range to assess flood inundation condition of an alluvial plain in central Vietnam (Ho et al., 2010). The study suggested that the extraction of moist soil by MNDWI can help to detect flooded sites; results were also compared with the landform classification map, SRTM DEM elevation ranges and land cover classification (Ho et al., 2010).

2.4   Satellite/Airborne Imagery and Remote Sensors Primary Data for Assessing the Impacts of Extreme Hydrologic Events

In addition to abstracted indices, the primary data generated by aerial and remote sensors have been used to develop flood maps. Different techniques for flood mapping using active and passive

RS systems have been developed and applied in several studies. Flood mapping of hurricane storm surge or inland flooding by passive RS systems includes identifying the water verses non-water areas and determining flooded area during the flood event. Table 2.3 lists the satellites used in past studies to identify EHE impacts on CWs based on spectral reflectance or primary data obtained from corresponding RS system. The order of satellites in Table 2.3 is presented based on spatial resolution (high/medium/low). Active sensors such as RADARSAT-1 are usually classified as medium resolution and therefore are placed in that resolution category (Chaouch et al., 2012). The advantages and disadvantages of each sensor are discussed briefly at the end of each category.

Table 2.3: Remote sensors used in past studies on CW resilience under EHEs

Satellite	Sensor	Date/Decom mission	Spatial Resolution (m)	Spectral Resolution	Repeat cycle (days)
High Resolution Sensor					
WorldView -1 & 2 (Hassan et al., 2014)	*PAN, *MS	September 18th, 2007;	0.46 m (both 1 and 2)	PAN (0.40-0.90 µm);	1.7 days (= <1 m GSD)
				MS (0.40-1.04 µm)	5.9 days (0.51 meter *GSD);
		October 8, 2009			1.1 days (= <1 m GSD
					3.7 days (0.52-meter GSD)

Satellite	Sensor	Date/Decom mission	Spatial Resolution (m)	Spectral Resolution	Repeat cycle (days)
QuickBird (Kumar & Sinha, 2014),	BGIS 2000 sensor	October 18, 2001	PAN: 0.65 m (nadir) to 0.73 m (20° off-nadir) MS: 2.62 m (nadir) to 2.90 m (20° off-nadir)	PAN (0.45-0.90 µm); MS (0.45-0.52 µm; 0.52-0.60 µm; 0.63-0.69 µm; 0.76–0.90 µm)	1-3.5 days, depending on latitude (30° off-nadir)
IKONOS (Jollineau & Howarth, 2002)	laser sensors, imagers, radar sensors, electro-optical astronomical sensors, planetary sensors	September 24, 1999	PAN: 0.82–1 m; MS: 3.2–4 m	PAN (0.49 – 0.90 µm); MS band 1,2,3,4 (0.45 – 0.52 µm; 0.52 – 0.60 µm; 0.63 – 0.69 µm; 0.76 – 0.90 µm)	14 days (max)
OrbView-3 (Klemas, 2013b)	PAN, MS	June 26, 2003	PAN: 1 m MS: 4 m	PAN (1 m); MS (4 m).	3 day
Medium resolution Sensor					
RADARSAT (Chaouch et al., 2012)	SAR	November 4, 1995	8–100 m (26–328 ft)	RADARSAT-1: Band C (5,3 Ghz); RADARSAT-2: Band C (5,405 Ghz)	24 days

Satellite	Sensor	Date/Decommission	Spatial Resolution (m)	Spectral Resolution	Repeat cycle (days)
JERS-1 (Jung, 2011)	-An L-band SAR; -A nadir-pointing optical camera (OPS); -A side-looking optical camera (AVNIR).	February 11, 1992	18 m	MS: Band 1,2 (0.52 - 0.60 µm; 0.63 - 0.69 µm); NIR band 3,4 (0.76 - 0.86 µm; 0.76 - 0.86 µm); SWIR: Band 5,6,7,8 (1.60 - 1.71 µm; 2.01 - 2.12 µm; 2.13 - 2.25 µm; 2.27 - 2.40 µm)	44 days
SENTINEL -1 (Muro et al., 2016)	C-synthetic aperture radar (SAR)	April 2014	5m	Band-C (8400 to 8450 MHz)	6 days
LANDSAT 8 (W.-T. Wu et al., 2017)	*OLI, *TIRS	February 2013	30m	PAN (0.50 – 0.67 µm); MS (0.43-0.67 µm); NIR (0.85-0.87 µm); SWIR (1.55-2.2 µm); Cirrus (1.36-1.38 µm);	16 days

Satellite	Sensor	Date/Decommission	Spatial Resolution (m)	Spectral Resolution	Repeat cycle (days)
				Thermal (10.60-12.51 µm).	
Landsat (ETM+) (Mueller et al., 2016)	Opto-mechanical	April 15, 1999	30 m	MS: Band 1-3 (0.45 um- 0.69 µm);	16 days
				NIR: Band 4 (0.77-0.90 µm);	
				SWIR: Band-5,7 (1.55-1.75, 2.09-2.35 µm);	
				Thermal: Band-6 (10.40-12.50 µm);	
				PAN: Band 8 (.52-.90 µm).	
Landsat 5 (Michishita et al., 2012)	TM	March 1984 to January, 2013	30 m	MS: Band 1-3 (0.45 - 0.69 µm);	16
				NIR: Band 4: (0.76-0.90 µm);	
				SWIR: Band-5,7 (1.55-1.75, 2.08-2.35);	
				Thermal: Band-6 (10.40-12.50)	

		Low Resolution Sensor			
MODIS (Michishita et al., 2012)	Aqua/Terra	December 18, 1999.	1 Km	36 spectral bands ranging from 0.4 µm to 14.4 µm (band at varying spatial resolutions: 2 bands 0.6µm - 0.9µm, 5 bands at 0.4µm - 2.1µm and 29 bands at 0.4µm - 14.4µm	1 day

*Multispectral = MS; Panchromatic= PAN; Micrometers = µm; Gigahertz. = Ghz; Near Infrared = NIR; Shortwave Infrared = SWIR; Ground sample distance = GSD, Operational Land Imager = OLI, Thermal Infrared Sensor =TIRS.

2.4.1   Airborne imagery

The very first aerial photograph was taken in 1858 by French photographer commonly known as Nadar, (Aber, 2004). Since then is has become one of the most important tools for science, engineering, and outreach. Aerial imagery portraying flood and storm surge impacts was an important initiative in assessing damage due to hurricane events. Recently, Adams et al. provided a foundation for data collection practices using unmanned aerial systems (UAS) and their potential for integration with damage assessment techniques using other aerial imagery (Adams et al., 2009). Among satellite, aerial, and ground based imagery types, each has its own advantages such as breadth for satellite imagery, resolution for aerial imagery, and obliqueness for ground based

imagery. Advances in UAS technology and its capability for coupling with aerial imagery may decrease overall costs while increasing the usefulness and applicability of the data. This method provides a strong basis for post hurricane event reconnaissance needs (Adams et al., 2009) due the increased safety compared with putting photographers into the affected area on foot or in ground vehicles. UAS enable flexible data acquisition for required time periods at low cost and is therefore well-suited for targeted monitoring of specific sites while satellite imagery provides the best solution for larger areas (Müllerová et al., 2017).

Coastal communities in the southeastern United States have regularly experienced severe hurricane impacts. To better facilitate recovery efforts in these communities following natural disasters, state and federal agencies must respond quickly with information regarding the extent and severity of hurricane damage and the amount of debris volume. To this end, a tool was developed to detect downed trees and debris volume to better aid disaster response efforts and tree debris removal. The tool estimates downed tree debris volume in hurricane affected urban areas using a Leica Airborne Digital Sensor (ADS40) camera and its high resolution digital images (Szantoi et al., 2012).

A multi-hazard hurricane event that brings high winds, high precipitation and storm surge complicates the development of robust automated assessment methods. To detect damage resulting from an event, we typically define threshold values selected from the target attribute's data distribution. Jiang and Friedland, (S. Jiang & Friedland, 2016) presented a mono-temporal image classification methodology using IKONOS panchromatic satellite and NOAA aerial color imagery collected in 2005 after Hurricane Katrina. The classification quickly and accurately differentiated

urban debris from non-urban debris using post-event images. However, aerial photography in CW studies mostly suffers from limitations due to daylight only acquisition times and weather factors that often accompany storm events such as clouds. Though issues associated with daylight and clouds can be mitigated with flight planning for airborne acquisitions, time sensitive data during storm seasons is likely to be obstructed by clouds resulting radiometric error and data loss (Morgan et al., 2010).

2.4.2   Low, moderate and high spatial resolution remote sensors (passive and active)

Spatial ground resolution is a measure of the length of the smallest dimension on the Earth's surface that can be captured by the sensor. RS systems with spatial resolution greater than 1 km are generally classified as low or coarse resolution systems (J. B. Campbell & Mryka Hall-Beyer, 1997). Coarse resolution and passive RS systems such as MODIS and AVHRR have been used in studies to examine phenomena occurring on scales larger than the ground resolution. For example, MODIS, combined with ecological field studies, Landsat and empirical based models, was used to quantify Hurricane Katrina's impact on U.S. Gulf Coast forests (Chambers et al., 2007). Mapping large areas impacted by flooding would be feasible by using low resolution data instead of high-resolution data. In a study in India, Jain et al. (Jain et al., 2006) used NOAA (National Oceanographic and Atmospheric Administration) AVHRR data for annual flood monitoring at the river Brahmaputra flowing through the state of Assam (India). The months of July and August were found to be flooded 25-30% of the time. However, a significant limitation of coarse resolution RS data is spectral similarity between distinctly different features such as dark water and shade (Michishita et al., 2012). Therefore, utilization of multi-sensor monitoring techniques that can

capture both the spatial details of middle-to-high resolution data and the temporal continuity of coarse spatial resolution data is needed to better understand spatio-temporal wetland dynamics.

Imagery with a spatial resolution of 5-100 m are classified as medium resolution systems (J. B. Campbell & Mryka Hall-Beyer, 1997). Passive sensors such as Landsat are categorized as medium resolution (on the order of 30 meters) satellite imagery and have been used in variety of applications such as wetland flood studies and flood model development (Barras et al., 2010; Chaouch et al., 2012; Nghiem et al., 2017; Robinove, 1978). Other medium resolution and passive satellite imagery such as Landsat 5 TM, SPOT 5, Landsat 7 ETM+, ASTER and PALSAR were used to identify storm surge-impacts from Hurricanes Gustav and Ike on Louisiana's wetlands and the interior coastal wetlands in southeastern Texas (Barras et al., 2010). Robinove (Robinove, 1978) used Landsat images to map floods in Queensland, Australia and interpreted dark areas as wet soils rather than flooded regions. In a 2017 study, Sentinel SAR satellite data (10 m resolution) has been used to detect, map, and monitor inundation including newly flooded areas and pre-existing water bodies. The flood inundation was assessed in August 2017, four days after Hurricane Harvey made landfall near Houston, Texas as well as the Florida Panhandle and the Florida Keys in September 2017 after Hurricane Irma made landfall as a Category 5 storm (Nghiem et al., 2017).

High spatial resolution data (5 m or less) have been available since data from commercial satellite systems became publicly available. Dramatic deformation occurs on coastal areas when coastal storms like hurricanes bring strong winds and waves that alter the topography and near-shore

bathymetry of the coast. A study by Seker (Seker et al., 2013) utilized InSAR to conduct a spatio-temporal analysis to investigate the effects of strong winds and waves on the coast of Karasu in Black Sea Region of Turkey. InSAR is capable of determining sub-cm level surface deformation under ideal conditions. The analysis showed the distinct changes to the landscape over time. During 2004, two strong tropical cyclones (hurricanes Frances and Jeanne) passed directly over the northern coast of the Bahamas. Comparisons of high resolution (2.4 m) QuickBird imagery and a quantitative wave model concluded that both the storms had limited effects on the sub-tidal platforms and the storm systems did not significantly alter the system. Instead, daily processes (winds, waves, and tides) were determined to be more plausible sources of geomorphic feature alterations (Reeder & Rankey, 2009).

2.4.3   Hyperspectral remote sensor (HRS)

Hyperspectral data are obtained using spectrometers that provide complete and continuous spectral information with a large number (224 for AVIRIS) of narrow wavelength bands. Available medium resolution hyperspectral sensors are AVIRIS (20 m); ALI (30 m); and Hyperion (30 m). Even with many new hyperspectral data available from both commercial and government programs worldwide, the airborne AVIRIS sensor is still considered the most useful hyperspectral sensor (Goetz, 2009). Although orbital sensors such as MODIS, MERIS and ASTER are sometimes classified as hyperspectral, these sensors lack the spatial (MODIS and MERIS) and spectral (ASTER) resolution desired for truly hyperspectral applications (Dor et al., 2012).

As stated previously, Barataria Bay in Louisiana was severely impacted in consecutive years by both the Deepwater Horizon oil spill in 2010 and Hurricane Isaac in 2011. Khanna et al. (Khanna et al., 2017) used AVIRIS hyperspectral imagery over this area just after the oil spill in September 2010, a year later in August 2011 and post-hurricane in October 2012. They found that after hurricane Isaac the oiled shorelines (up to the 7 m topographic contour) experienced a 17.8%, while the land loss on oil-free shorelines was 13.6%. Zhang (H. Zhang et al., 2014) combined AVIRIS hyperspectral imagery and Light Detection and Ranging (Lidar) data to map the vegetation of the Florida Everglades. While the combined method produced an overall classification accuracy of 86% compared to ground truth, the hyperspectral images alone were 76% accurate. Though not directly related, a similar comparative analysis study of EO-1 ALI / Hyperion and Landsat ETM+ Data for Mapping Forest Crown Closure (CC) and LAI described that the Hyperion sensor outperforms the non-hyperspectral sensors. Hyperion has high spectral resolution including SWIR data which are able to construct optimal VIs that are less affected by the atmosphere. Between ALI and ETM+, ALI performed better for mapping forest CC and LAI since ALI data have more bands and higher signal-to-noise ratios than ETM+ data. The study indicated that Hyperion has the potential for productive before-after analysis of impacts in CW.

Hyperspectral acquisition and analysis are often costly for large areas and can generate large amounts of data to store and process. Due to the variety of sun angles for every flight strip, separate solar and atmospheric adjustments are required in addition to the standard adjustments made to compensate for aircraft pitch, roll and yaw (Porter et al., 2006).

2.4.4 Active remote sensors (Radar and Lidar)

2.4.4.1 Radar

Radar remote sensing is a useful tool for monitoring CWs over large geographic areas due its 30 m (or better) spatial resolution and ability to penetrate clouds that frequently obscure coastal areas. Chaouch et al. (Chaouch et al., 2012) detected inundation between semi-diurnal low and high water conditions using satellite imagery from Radarsat-1 and Landsat along with aerial photography in the northern Gulf of Mexico. The inundation maps were validated using historical aerial photography and achieved a classification accuracy, measured by Probability of Detection (POD) of 83% (Chaouch et al., 2012). The combination of SAR data and optical images, when coupled with a high resolution (2 m) digital elevation model, was shown to be useful for inundation mapping and demonstrated potential for the follow-on application of evaluating wetting/drying algorithms in coastal hydrodynamic models. This method was successfully applied to tidal simulation results produced by the ADCIRC model (Medeiros et al., 2013)(Medeiros & Hagen, 2013). The differences between modeled and RS derived synoptic inundation extents indicated specific geographic areas in the model where performance was weak and therefore enabled the modelers to make targeted revisions to the input data, especially the terrain characterization (Medeiros & Hagen, 2013).

SAR has distinct responses to open water and water with varying emergent vegetation coupled with all-weather capability, making the SAR sensors a promising choice for monitoring wetland ecosystems in storm prone regions with frequent cloud cover. SAR systems are useful for mapping floods because of their independence from the sun as the illumination source, their all-weather

functionality, and ability to penetrate forest canopy at certain frequencies and polarizations (Kiage et al., 2005; Townsend, 2002). All of these attributes allow SAR systems to provide medium resolution flood inundation extents free of cloud cover contamination compared to Landsat TM or MSS. Imhoff et al. (Imhoff et al., 1987) presented SAR imagery as more effective than Landsat MSS for monsoon flood mapping in Bangladesh. Henry et al. (Henry et al., 2006) used multi-polarized SAR data for flood mapping of Elbe river basin, Central Europe. Horrit et al. (Horritt et al., 2001) delineated flood from the SAR imagery by applying a statistical active contour model. Thus, emergency mapping and flood management is a very useful and practical application of SAR. SAR images have 24 hour (i.e. day or night) capabilities as an active microwave satellite sensor that can penetrate clouds thereby making them valuable for flood monitoring (Grings et al., 2006) since cloud cover is typically associated with flood events.

2.4.4.2 Lidar

Lidar is an RS technology used mainly to conduct topographic surveys (Hladik & Alber, 2012; Hooshyar et al., 2017; Medeiros et al., 2015) from an airborne platform. It measures the range between the target and the sensor using a pulsed laser. Lidar is useful to estimate the threat of SLR to coastal ecosystems and also to analyze the intensity and level of impact from raised water elevation and salt water penetration to coastal ecosystems (Moeslund et al., 2011). For example, Huang et al. (Huang et al., 2014) monitored wetland inundation using Landsat and Lidar data. Lidar is also useful for detecting water surfaces, even small channels, due to its fine spatial resolution and strong absorption of light energy by water surfaces. Integrating Lidar elevations

and signal intensity of ground returns were utilized to map the wet channel networks of several watersheds near Lake Tahoe (Hooshyar et al., 2015).

Lidar is known for its ability to cover large geographic locations at a relatively low cost compared to traditional land surveying. Digital Elevation Models (DEMs) derived from Lidar are generally recognized to produce topographic surfaces that are accurate enough for a variety of modeling, mapping and civil engineering applications (Medeiros et al., 2015). Real Time Kinematic (RTK) topographic survey data still outperforms Lidar in terms of vertical accuracy, especially in areas of dense low vegetation such as coastal marshes (Hladik & Alber, 2012; Medeiros et al., 2015). This is mainly due to the inability of the laser to penetrate the marsh grasses and reflect off of the true marsh surface. In addition, raw (unadjusted) Lidar intensity data are usually incomparable between Lidar collections and are sensitive to the angle at which the laser interacts with ground surface (Kim et al., 2009).

2.5   Future Wetland Remote Sensing Studies

Future opportunities for RS research in CW will involve both maximum utilization of existing high-resolution sensors such as Hyperion and investigation / development of new sensors. There is both significant potential and emerging environmental challenges that RS is suitable to address such as the global monitoring of mangrove forests, the ecological effects of SLR (Medeiros et al., 2015), and the progress and effectiveness of restoration efforts. There is also potential for future studies in finding both spatial and temporal changes in ecosystems and linking them with

global/regional climatic or hydrologic events. Alongside these potential RS based advances, innovative ground truth techniques that validate them will also be necessary.

2.5.1 Algorithms for multi sensor integrations in wetland studies

Remote sensing has been used widely for wetland classification for more than 50 years, achieving a wide range of effectiveness. Some have used single source data such as photography, medium-resolution images, high-resolution images (Tahsin et al., 2017), hyperspectral images (Barducci et al., 2009), radar and lidar data (Hooshyar et al., 2015; Zhang, 2010) with conventional or improved methods of data mining to model or classify wetland ecosystems. Others used a combination of remote sensing and field survey data for the same purpose (Medeiros et al., 2015). A few studies suggested that integrating different data sources can increase the classification accuracy (Klemas, 2013a; Klemas et al., 1993). Integration is especially useful when sensor types such as combining optical images with radar or Lidar data. Additionally, multi-season RS can increase classification accuracy (Wu et al., 2017) by presenting data for the same location in two or more phenological states. Scientists and engineers must be rigorous when combining sensor data from different time periods to detect expected (growth, color change) and unexpected (land clearing, storm damage) effects. All areas with emergent vegetation, such as wetlands, have high heterogeneity in reflectance due to water level, turbidity and vegetation density (for example), so merging data acquired at different times needs careful attention and defensible / reproducible methods with transparent parameter selection based on plausible physical factors. Development of validated algorithms for unifying different spatio-temporal resolution sensors to a common basis would be a useful tool for RS studies, especially those of wetlands.

2.5.2   <u>Large spatial scales</u>

A very few past studies have focused on using remote sensors on a global scale. Hydrologic impacts and changes to ecosystems are better understood at larger spatial scales. Since global scale studies require onerous data collection and management processes, they tend to be very expensive which necessitates choosing imagery carefully to meet the objective under budget and computational constraints. Generally, low resolution images are used only when a gross level of vegetation classes is sufficient, whereas higher resolution images are used for fine vegetation classifications. Therefore, both from mapping scale point of view and cost efficiency, vegetation mapping at local/small scale generally needs high-resolution images, while low-resolution images are used for a large-scale mapping. MODIS data are a common source of coarse-resolution data that have the capability to map global wetland change. MODIS derived secondary data have been used in several studies mentioned previously. Radar RS offers a global perspective for several hydrological parameters. The all-weather capable satellite radar altimetry is used to delineate water bodies and wetland levels and infrared imagery can be used to detect visible wet areas. A program to globally and continuously monitor all large inland water bodies at the Mullard Space Science Laboratory (MSSL) showed an accuracy of 5 cm root mean square (RMS) of these waterbodies level variation (Birkett, 1995). The development of ScanSAR technologies made it possible to monitor the impact of climate change in permafrost transition zones. For example, using ENVISAT ASAR Global mode (GM, 1 km resolution), climate and environmental data (up to 2012) from boreal environments are available for research and analysis. Research as identified up to 75% of oligotrophic bogs in the seasonal permafrost zone (Bartsch et al., 2009). Also, the high

seasonal and inter-annual dynamics of the sub-tropic Okavango Delta in Botswana, Africa, were captured by GM time series (Bartsch et al., 2009).

Although the understanding and quantifying of wetland dynamics has been advanced, the validation of large-scale wetland monitoring is still challenging and needs to be extended using auxiliary data from secondary sources such as in-situ measurement and unmanned aerial vehicles. Coarse-resolution can be used to globally map wetlands using the decomposition of mixed pixel technology (Guo et al., 2017). NOAA and MODIS coarse-resolution data and their derived vegetation indices can map global wetland changes. High performance computing opens many opportunities for fine resolution classification, prediction of missing/obstructed wetland hydrologic data, and modeling wetland hydrology temporal dynamics.

2.5.3 New data and methods

The prime weakness of optical data is the data loss due to clouds, haze, and shadows. In some regions, especially coastal areas, clouds and rain events are frequent and these wet periods are important for plant growth and aquatic ecosystem balance. During this period, hydrologic events such as storms, hurricanes, and high precipitation occur and the need of large spatial coverage using RS arises to monitor the intensity of these hydrologic events and subsequent vegetation change. However, while the objectives may be clear, difficulties can still occur. For example, the optical sensor on board Landsat 7 occasionally showed anomalies such as Late Start Anomalies (LSAs) that was observed from 2006 to April 2007. Then, Landsat 7 switched to bumper mode and the LSAs cannot occur in bumper mode and the problem resolved. Another issue with optical images is that they usually fail to monitor vegetation types within wetlands because the dense

vegetation cover leads to signal saturation. Previous studies explored several methods as well as different sensors to overcome these limitations. To mitigate the data loss due to cloud cover, the Optical Cloud Pixel Recovery (OCPR) method was developed (Tahsin et al., 2017) to repair missing remote sensor pixels using information from the time-space-spectrum continuum. Using a Random Forest (RF) model trained using over fifteen years of Landsat imagery and local hydrologic data, NDVI values for cloud obscured pixels were able to be recovered with sufficient accuracy so that images that would have been previously discarded can now be used in the long-term time series. The OCPR model performed well in a dynamic wetland ecosystem in the northern Gulf of Mexico. If optical images are obstructed by clouds, they are unable to accurately describe the extent of saturated areas in wetlands. Marechal et al. (Marechal et al., 2012) overcame this by employing time series Radarsat-2 data to monitor the seasonal changes of wetlands using SAR data and new supervised PolSAR segmentation methods, taking advantage of the radar data's ability to penetrate clouds.

Landsat 8 launched in 2013 is the most evolved platform of the Landsat lineage. Landsat 9 is planned to be launched in 2020 and will continue to evolve as did Landsat 8. Both Landsat 8 and 9 have the Operational Land Imager (OLI) and the Thermal Infrared Sensor (TIRS) (Irons, 2018). Landsat 8 has further capabilities to investigate water resources and for the detection of cirrus clouds and also provides information on the presence of features such as clouds, water, and snow. The innovative designs of Landsat 8 and Landsat 9 make them more sensitive and more reliable than earlier Landsat satellites.

They can be used to detect more subtle details in the images. The multispectral sensors on board Landsat 8 and Sentinel-2 offer the possibility to perform high-frequency time series analyses. They have the potential to carry out multi-temporal change detection before and after significant events such as mapping for disaster management. The end user must still pay particular attention to the impact of the radiometric differences between the images (Landsat 8 and Sentinel-2) acquired by the two sensors (Mandanici & Bitelli, 2016). Though both sensor's radiometric accuracies are high, the difference still requires careful evaluation to determine whether the differences in reflectance values are relevant and fulfill the purpose of the specific application. Sentinel-3 (launched at February 2016; design life: 7 years) is considered the most improved version of the family of Sentinel satellites. The Sentinel system first launched in 2014 resulted in an exceptional blend of spatial resolution, spectral coverage and temporal revisit time. Sentinel-3 has even greater potential to enhance water quality assessment, eutrophication monitoring and plant / crop health monitoring (Huck, 2016). Newer data from various remote sensors on board of many different platforms and of different types will continue to be leveraged to produce more robust methods utilizing longer time series.

2.6   Summary and Conclusions

This paper provides an overview of RS applications in assessing the impact of extreme hydrologic events in coastal wetlands. Coastal wetlands worldwide have been experiencing significant threats due to extreme hydrologic events. Sea level rise, intensified storms, and changing freshwater input, along with human impacts, directly impact coastal wetlands and limit their ability to provide

valuable ecosystem services. The usefulness of vegetation indices and other methods for identifying the impact on coastal wetlands is the primary focus of the current review paper.

Remote sensors were categorized according to their ground resolutions: Coarse, medium, and high. Hyperspectral images are a unique case and have a range of ground resolutions along with their fine spectral resolution. Also, remote sensors typically used in this application were categorized as active and passive according to their source of electromagnetic radiation. Satellite/aerial photography is also an integral part of sensor systems used to monitor and assess hydrologic impacts and in recent years, aerial photography has been used in conjunction with unmanned aerial systems to assess post storm damage and classify different types of coastal wetlands. Depending on the areal extent and purpose of a particular study, investigators blend a variety of sensor data that adequately captures the spatial, spectral, and time scales relevant to the target wetland and hazard types. Often times, abstracted indices, such as Normalized difference vegetation index, derived from MODIS, LANDSAT and/or AVHRR are frequently used in coastal wetland studies. Hyperspectral data are used mostly in relatively small area studies due their advantage of deep spectral resolution and also their high cost and data magnitude. Active sensors such as synthetic aperture radar consistently outperformed optical sensors in coastal wetland change detection because of its ability to penetrate clouds and canopy. lidar data have also been shown to be very useful for monitoring and exploring ground surface and elevation information such as the height of forests or the water level. Many studies use lidar in combination with other forms of remote sensing data to amplify the classification and quantification effectiveness.

This study documented previous researches on the application of remote sensing with special focus on vegetation indices to identify and assess the impacts of extreme hydrologic events on coastal wetlands. The discussion aimed to identify limitations and advantages of certain vegetation indices and also primary sensor data in an effort to guide future research into this application of remote sensing. This study also discussed potential future research topics for enhancing coastal wetland studies using remote sensing. Thus, this paper provides a reference base for future studies involving long term monitoring of coastal wetlands, especially their response to extreme hydrologic events.

CHAPTER 3: WETLAND DYNAMICS INFERRED FROM SPECTRAL ANALYSES OF HYDRO-METEOROLOGICAL SIGNALS AND LANDSAT DERIVED VEGETATION INDICES

3.1   Introduction

The spatial extent and composition of coastal wetlands (CW) varies in response to hydrologic and meteorological conditions (e.g. precipitation and wind) and extreme events (e.g. droughts and floods). These variations represent a major source of CW alteration on the global, regional, and local scale (Bilskie et al., 2016; La Cecilia et al., 2016; Clinton et al., 2014; Van Hoek et al., 2016; Passeri et al., 2016). Knowledge of CW dynamics across scales is important as these wetlands provide a variety of ecosystem services such as habitat (Sivaperuman & Venkatraman, 2015), protection from storm surges (Barbier, 2013; Wamsley et al., 2010), water quality enhancement by nutrient uptake and filtration, carbon sequestration, and commercial and recreational fishing. CW also provide other important ecosystem services such as erosion control, local water storage improvement (Wong et al., 2017), climate regulation and stabilization, and are a unique aesthetic landscape of cultural, historic and spiritual relevance (Barbier, 2013).

The characterization of both terrestrial wetland (Papa et al., 2006; Tadesse et al., 2014) and CW dynamics can be efficiently approached by using satellite remote sensing data that are available over wide and consistently sampled areas. Satellite remote sensing can be particularly important for monitoring long-term CW changes (Rodgers et al., 2009; Steyer et al., 2013). The Normalized difference vegetation index (NDVI) is a vegetation index that is used to measure vegetation

greenness and can be derived from several remote sensors. This index is sensitive to the green vegetation biomass as affected by the type of wetland and season (Guo et al., 2017). It has been well correlated with wetland greenness, for example, in Apalachicola Bay of Florida (La Cecilia et al., 2016; Tahsin et al., 2016). Landsat NDVI is also regarded as a reliable indicator for wetland pattern change detection (Kayastha et al., 2012). Furthermore, NDVI derived from Landsat has the most comprehensive spatial and temporal coverage along with reasonable resolution when compared to other publicly available satellite imagery. Landsat satellites has been collecting valuable information since 1984 and such a long-term record is unique among satellite remote sensing products.

Previous studies established that vegetation phenology in different parts of the world is a key indicator of climate-biosphere interactions. Timings of phenology is linked to precipitation (Maignan et al., 2008) and temperature (Myneni et al., 1997; Zhou et al., 2001), especially, in the northern high-latitudes. As the global hydro-meteorology changes as part of the climate, vegetation is adapting and simultaneously feeding back to the larger system (Foley et al., 1994; Kirilenko & Sedjo, 2007).

The presence of feedback mechanisms relating Earth's coastal/terrestrial systems and hydro-meteorology, implies the presence of cross-correlation structures (interdependencies) and memory effects. Within this feedback structure, the concept of persistence, explained through the idea of scaling behavior of Fourier transformed hydro-meteorological signals (Feder, 1988; Telesca & Lasaponara, 2006), can be useful to discern the resilience of wetland vegetation. Persistence of a system refers to a phenomena that is controlled by positive feedback mechanisms, which tend to

disrupt the stability properties of the system and make them vulnerable to external forcing (Maktav, 2009; Witt & Malamud, 2013; Zheng et al., 2010). Since resilience of a system is the capability to respond to a disturbance by resisting damage and recovering quickly, ecosystem resilience can be studied by their persistence through time (Switzer et al., 2006). The quantification of memory and persistence in a signal requires long-term data and satellite remote sensing often fills this need. However, not all satellites provide long-term time-series data and there is often missing information within the available time-frame. A methodical and repeatable framework for addressing this issue is therefore required to characterize vegetation dynamics at temporal scales ranging from seasonal to multi-decadal.

In this study, we use the time-series of NDVI and hydro-meteorological data from 1984 to 2015 for Apalachicola Bay, Florida. Spectral analysis of these data allows for the characterization of persistence in the signal. While previous studies focused on vegetation dynamics in terrestrial areas using conventional data and methods, CW dynamics using long-term remote sensing data and robust methodologies for the extraction of complex interaction related information is understudied. This study aims to partially fill that knowledge gap.

We quantified the time-lag between the forcing (hydro-meteorological) and response (NDVI) signals for target coastal areas based on the National Oceanic and Atmospheric Administration (NOAA) Coastal Change Analysis Program (C-CAP) classification system. Most previous models estimated time-lag using linear correlation or cross-correlation between changes in two or more indices over time or used a time-lag defined *a priori*. These techniques could lead to insufficient results due to the large variation in NDVI across both spatial and temporal scales, making previous

assumptions unsuitable to be adopted globally or locally (Clinton et al., 2014). Also, the influence of the varying growth periods of vegetation could affect the results as well. We minimized these limitations first by applying cross-spectral analysis over wetland vegetation and hydro-meteorological signals which allows the determination of the similarities between two signals as a function of frequency with the help of phase shift; and second by re-classifying CW into aggregate classes (freshwater and saltwater types); and third by extracting time-lags directly from cross-spectral components.

The aim of the study was to i) understand and quantify any prevailing variability in persistent behavior among different CW vegetation classes; ii) characterize the spatio-temporal sensitivity of CW with hydro-meteorological signals under various frequency domains; and iii) assess the spatial difference in time-lag between forcing (hydro-meteorological) and response (NDVI) signals.

3.2   Data and Methods

3.2.1   Site description and coastal wetlands classification

The setting for this study was Apalachicola Bay in the Florida Panhandle, with the specific study area indicated by the black boundary in Figure 3.1 a). CW have been classified by C-CAP along the eastern seaboard and Gulf coasts of the United States (Ramsey III et al., 2001). Figure 3.1 b) depicts the type and the locations of CW in the study area. The specific wetland classes investigated were: Palustrine-forested wetland (PFW): 54.1%, Palustrine-emergent wetland (PEW): 7.9%, Palustrine-scrub and emergent- wetlands (PSEW): 11.7%, and Estuarine-emergent wetland (EEW): 6.5%.
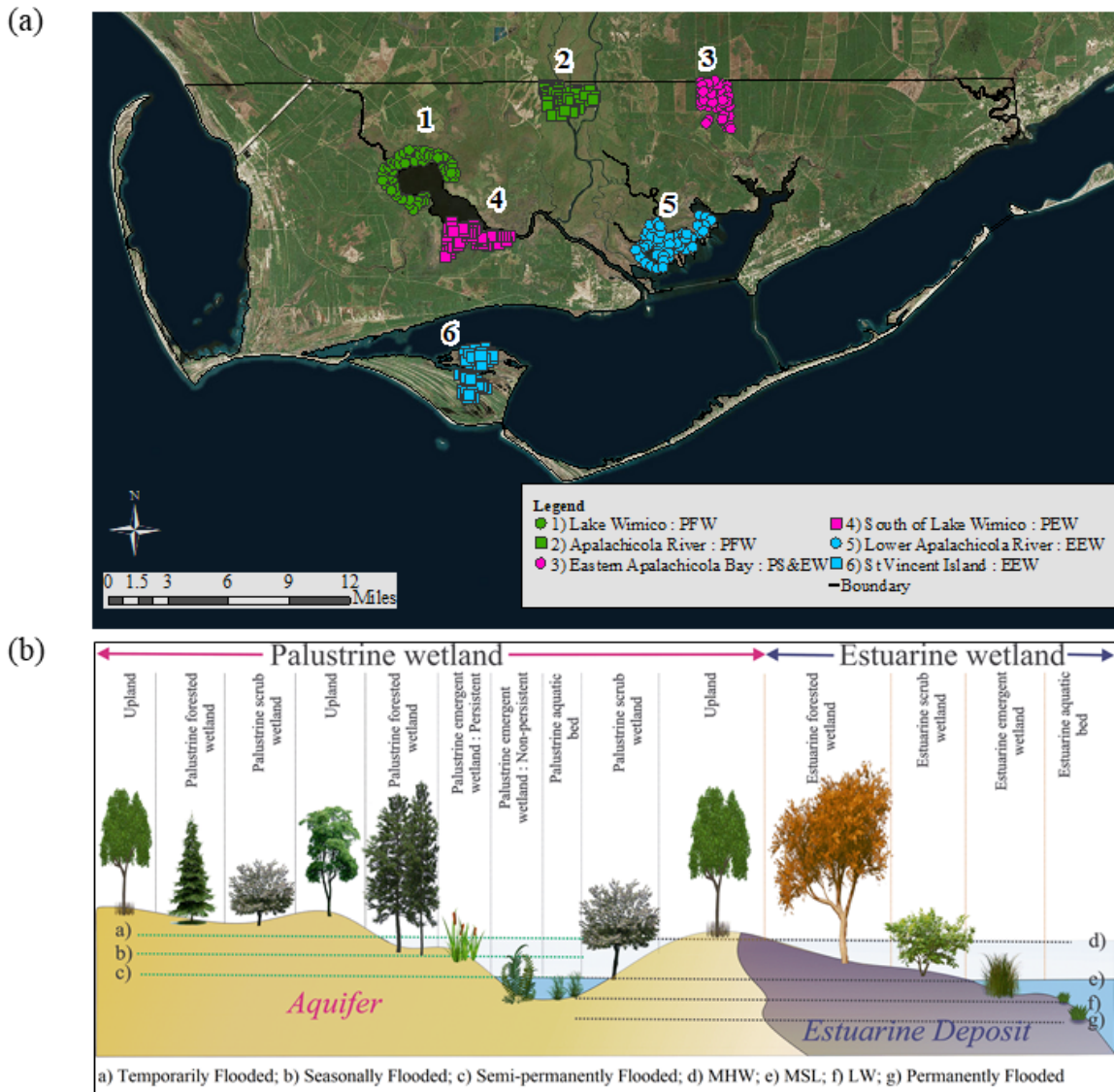
Figure 3.1: a) Different classes of wetlands* at spatially separated locations in the Apalachicola Bay; b) Distinguishing wetland habitats in Palustrine and Estuarine Wetlands: CW ecosystem definitions based on NOAA C-CAP. *Palustrine forested wetland (PFW); Palustrine emergent wetland (PEW); Estuarine emergent wetland (EEW); Palustrine scrub/shrub and Palustrine emergent wetland (PSEW). Mean high water (MHW); Mean sea level (MSL); Low water (LW)

Other wetland classes such as Estuarine forested wetland, Estuarine scrub/shrub wetland are uncommon (<1%) in the study area. 19.56% of the study area was comprised of other land uses than wetlands, including developed area, agricultural use, and bare land.

We selected six locations (see Figure 3.1 a) inside the study area to represent the dominant wetland types. The spatial variability includes PFW at two locations: Lake Wimico and Apalachicola River; EEW at two locations: lower Apalachicola River and St. Vincent Island; PSEW at one location – Eastern Apalachicola; and PEW at one location – South of Lake Wimico.

3.2.2   Forcing and Response Signals

Surface reflectance of Landsat-5 data were acquired between 1984 and 2015 from USGS Earth Resources Observation and Science Center archive to calculate NDVI. After image acquisition, all images were registered and clipped to the spatial extent of the study area. Spatial registration, resampling and projection using WGS1984 UTM Zone 16N was implemented using ArcGIS. NDVI was calculated as the normalized ratio of red (*R*) and near-infrared (*NIR*) reflectance of a sensor system and generally characterizes the greenness of wetland vegetation. It is commonly expressed as equation 3.1.

$$NDVI = \frac{NIR - R}{NIR + R} \qquad\qquad (3.1)$$

For heavily vegetated areas, NIR reflectance is greater than Red reflectance due to the tendency of chlorophyll to absorb red light. In those areas, NDVI values greater than 0 are expected (Tahsin et al., 2016, 2018). The C-CAP wetland classification was superimposed onto the wetland NDVI to label NDVI according to CW classes.

Water level, precipitation, temperature and wind speed data were collected over the same spatial region and time period. Water level data were collected from NOAA / NOS coastal gage station (Station ID: 8728690) located at Apalachicola, FL. Precipitation, temperature and wind speed data were collected from Automated Surface Observing System (ASOS) stations located at the airports in the United States and maintained by IOWA State University, IOWA Environmental Mesonet. The AAF Apalachicola Muni ASOS station, located inside the study area was used for the analysis in the study.

3.2.3   Methodology

3.2.3.1 Power Spectral Density and Scaling Behavior in the Frequency Domain

Power spectral density (PSD) is a measure of the frequency response to the variation in a signal. In general, PSD analysis provides a standard method to identify correlation features in time-series fluctuations and describes how the energy in a signal is distributed across various frequencies (Singh et al., 2010). The PSD $S(\omega)$ of a discrete signal $F(x)$ can be computed as the average of the Fourier transform magnitude squared, over a large time interval and expressed as equation 3.2.

$$S(\omega) = \left| \frac{1}{2\pi} \sum_{-\infty}^{\infty} F(x)e^{-i\omega t} \right|^2 \quad = \quad \frac{\hat{F}(\omega)\hat{F}^*(\omega)}{2\pi} \tag{3.2}$$

where $\hat{F}(\omega)$ is the discrete Fourier transform of $F(x)$, $\hat{F}^*(\omega)$ is its complex conjugate and ω is the wavenumber (Singh et al., 2012; Stoica & Randolph, 1997).

We analyzed the scaling behavior of the PSD which was determined to be a power-law dependence of the spectrum on the frequency ω in the following equation 3.3.

$$S(\omega) \sim \frac{1}{\omega^\beta} \tag{3.3}$$

Here β is the power-law exponent of the PSD. A robust estimation of the scaling exponent β can be achieved by computing the slope of the linear regression fitted to the estimated PSD plotted on log–log scales (Pilgram & Kaplan, 1998). The strength of these scaling exponents provides useful information about the inherent memory of the system (Miramontes & Rohani, 2002; Witt & Malamud, 2013). Witt & Malamud, (2013) found PSD analysis to be a more accurate method to quantify persistence of a self-affine time-series than other empirical methods such as Hurst rescaled range (R/S) analysis, detrended fluctuation analysis, and semi-variogram analysis. The basic feature of a self-affine time-series is that the PSD of the time-series has a power-law dependence on frequency and as a result they exhibit long-range persistent behavior (Malamud & Turcotte, 1999; Mandelbrot & Ness, 1968). In other words, a time-series is self-affine if it exhibits statistical self-similarity i.e. invariance under suitable scaling of time or have the same statistical properties (Mandelbrot, 1984) when the two axes are scaled differently. A steeper PSD indicates a higher persistence (or low vulnerability) which characterizes stability or instability in the concerned ecosystem. In more general cases of long-range persistence, β ~ 0 implies that the temporal fluctuations are purely random and are characterized by the uncorrelated sample – typically white noise processes; $0 < \beta \leq 1$ is known as a pink or flicker noise (Bak et al., 1987; Mandelbrot & Ness, 1968). Pink noise is a statistically reliable departure from white noise in the direction of persistence (Holden, 2005). $\beta = 2$ is known as brown noise (or Brownian motion), however its increments are uncorrelated and result in white noise with $\beta = 0$. Both pink and brown noise correspond to persistent behavior and indicate the presence of a positive feedback mechanism.

3.2.3.2 Cross-spectrum and Time-Lag Analysis Between Signals in the Frequency Domain

Cross-spectrum analysis relates the variance of two signals. The cross power spectral density (CPSD) is computed using a real valued PSD estimate of time-series $z_i(t)$ defined as $\hat{F}_{z_i}(\omega)$ and the complex conjugate of the PSD estimate of time-series $z_j(t)$ defined as $\hat{F}_{z_j}^*(\omega)$ in the frequency domain (ω), and is given by equation 3.4.

$$\hat{F}_{z_i z_j}(\omega) = \hat{F}_{z_i}(\omega)\ \hat{F}_{z_j}^*(\omega) \tag{3.4}$$

The real component of the CPSD is defined as the co-spectrum, C_o, whereas the imaginary component is defined as the quadrature spectrum, Q. Equation 3.4 can thus be re-written as equation 3.5.

$$\hat{F}_{z_i z_j}(\omega) = C_o(\omega) + Q(\omega) \tag{3.5}$$

The phase spectrum estimate $\phi_{z_i z_j}(\omega)$ is bounded between $-\pi$ and π and is the phase difference at each frequency between z_i and z_j. It can be calculated from the real and imaginary components of the CPSD in equation 3.6.

$$\phi_{z_i z_j}(\omega) = \tan^{-1}\left[\frac{Q(\omega)}{C_o(\omega)}\right]. \tag{3.6}$$

Finally, the time-lag $\phi_{z_i z_j}(t)$ can be obtained from the phase spectrum as equation 3.7.

$$\phi_{z_i z_j}(t) = \frac{\phi_{z_i z_j}(\omega)}{(2 \times \pi \times \omega)} \tag{3.7}$$

where $\phi_{z_i z_j}(\omega)$ is the phase in radians and ω is the radian frequency (Van Hoek et al., 2016).

3.3 Results and Discussion

The NDVI time-series for the six selected locations from 1984 to 2015 (sampled monthly) are shown in Figure 3.2 a. The three black-dashed boxes in the time-series highlight the dynamic behavior of the NDVI ranging from approximately 0.1 to 0.9 and are shown in greater detail in Figure 3.2 b (1985 to 1987), Figure 3.2 c (1995 to 1996), and Figure 3.2 e (2004 to 2006), which were marked by several extreme events including various minor and major hurricanes, droughts, and floods (Hurricane Research Division, 2012). The black solid box highlights less dynamic NDVI ranging from approximately 0.4 to 0.9 (Figure 3.2 d; 2001 to 2002), where there were no reported extreme natural or anthropogenic events. However, NDVI for PFW still had a distinct peak and drop during this but varied little for EEW, PEW and PSEW. Therefore, these time-series hinted at the disparate response among PFW, PSEW, PEW and EEW.
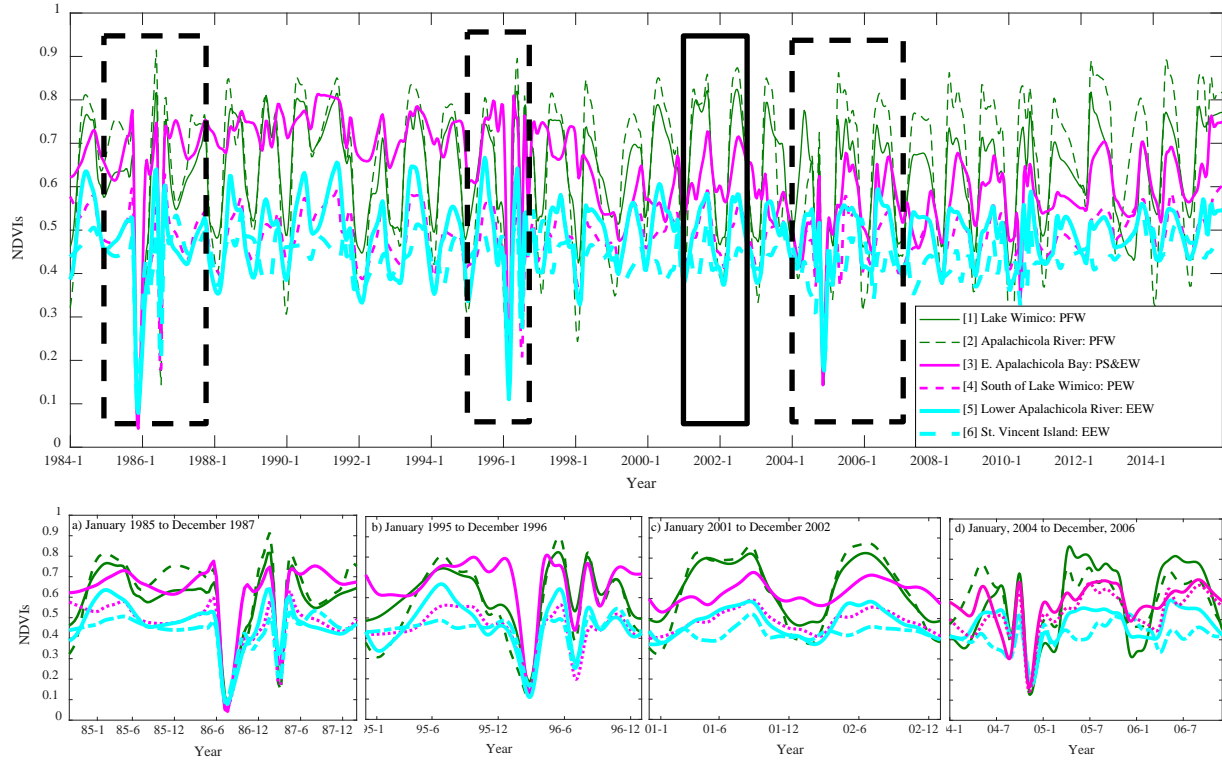
Figure 3.2: Time-series of NDVIs at spatially separated six locations in Apalachicola Bay from 1984 to 2015. [1] through [6] in the legend indicate the locations of wetlands (see Figure 3.1 **a)**

To further investigate the disparate behavior among different wetland types, we identified peak greenness and explored periodic trends using PSD analysis. Figure 3.3 shows the averaged PSD of NDVIs at six locations in Apalachicola Bay (see Figure 3.1 a for location). Visual observation suggests that the PSDs, which were plotted in log-log scale, were not flat (slope $\beta \neq 0$) for the analyzed frequency scale. This indicated that the wetland dynamics were not characterized by purely random and uncorrelated temporal fluctuations but instead contained correlated time-structure and memory phenomena.
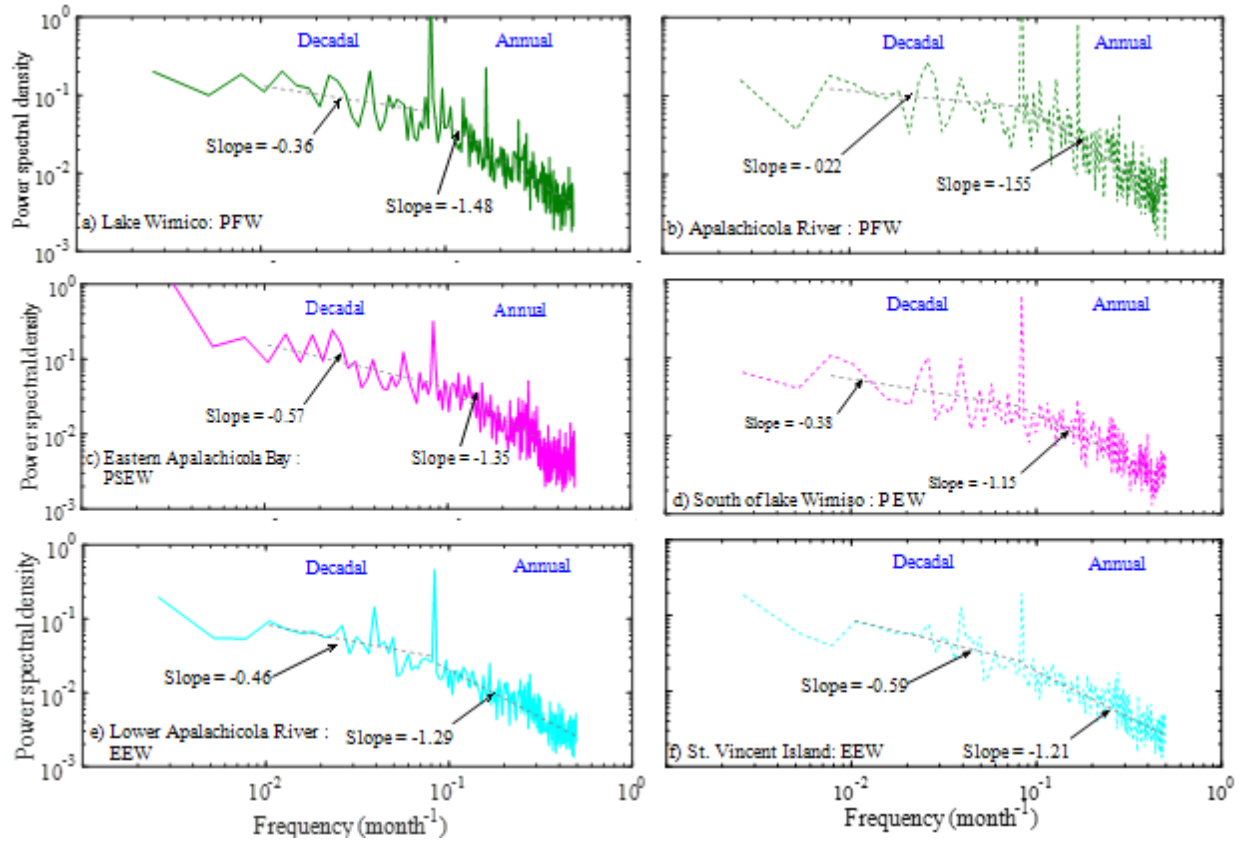
Figure 3.3: PSD of NDVI at spatially separated wetland locations around Apalachicola Bay. For all locations, the PSDs were computed as an average of PSDs from 60 data points (pixels); the locations are shown in Figure 3.1 **a.**

Figure 3.3 (a) and Figure 3.3 (b) show two different modality behaviors with distinct annual (frequency peaks at $f = 0.085$ (month^{-1})) and semi-annual peaks (frequency peaks at $f = 0.1693$ (month^{-1})). Modality indicates the periodicity of the vegetation. Generally, multi-modality occurs in places with double cropping, or with vegetation that is highly responsive to bi-modal temperature and/or precipitation regime, or with diverse land-cover types (Yang et al., 2001). In our case, there were two peaks of greenness for PFW occurring at different times. This was mainly due to the heterogeneity of the PFW, which consists mostly of woody vegetation both in tidal or non-tidal wetlands. Characteristic species are Tupelo (*Nyssa*), Cottonwoods (*Populus deltoids*) and Bald Cypress (*Taodium distichum*) (Conner & Buford, 1998). For PFW, the main greenness peak

66

was associated with the spring season, whereas the second peak was likely due to the larger availability of fresh water during the main precipitation season in the months of October and November. This finding is consistent with previous studies (Lizárraga-Celaya et al., 2010; Telesca & Lasaponara, 2006; Vivoni et al., 2008).

However, for the other four sites (PSEW, PEW and EEW), shown in Figure 3.3 (c), (d), (e) and (f) there was a unimodal NDVI seasonal cycle. This peak ($f = 0.085$ (month^{-1})) indicated a strong annual component of the NDVI fluctuations. An early peak supporting initial springtime plant emergence was observed for PSEW, PEW and EEW in Apalachicola Bay, followed by 3-4 months of gradual plant growth until the summertime rain provided adequate moisture for the rapidly established NDVI peak. This type of unimodal greenness is also found at south-west American regions, for example Utah/Colorado sites and Audubon showed a unimodal NDVI cycle, where springtime snowmelt and an initial precipitation peak support springtime plant emergence, then the plants keep growing gradually for the next 3-4 months and NDVI peaks in summertime (Notaro et al., 2010).

The results also indicated two scaling regimes in the PSDs of the wetlands associated with annual and decadal scales. In the annual frequency domain, the slopes were steeper for the PFW wetlands PSD compared to the slope for PSEW, PEW and EEW wetlands. The finding was similar to previous findings where scrub wetlands (here PSEW) were found to be less persistent (Dinerstein et al., 2019), and emergent wetlands (here PEW and EEW) were found to be more salt tolerant (Adam, 1990). Coastal forests (here PFW) were also found to be more persistent in a previous study in southern Italy (Telesca & Lasaponara, 2006). In this study, the persistence reversal was

observed at the decadal frequency where the NDVI values for the PSEW, PEW and EEW were more persistent than PFW. Figure 3.2 (d) graphically explains the dynamic nature of PFW annually where NDVI dropped sharply (from 0.9 to 0.4) while the NDVI for the other wetland categories fluctuated within a much narrower range (from 0.6 to 0.4). At the decadal scale, PSEW, PEW and EEW had larger persistence in NDVI values compared to PFWs which indicates a more unstable character with respect to external perturbations. Hurricanes, storm surges or other hydrologic events impact the coastal areas over a relatively sudden and short time span and since PSEW, PEW and EEW are generally located closer to the coast than PFW, they were impacted first and more severely.
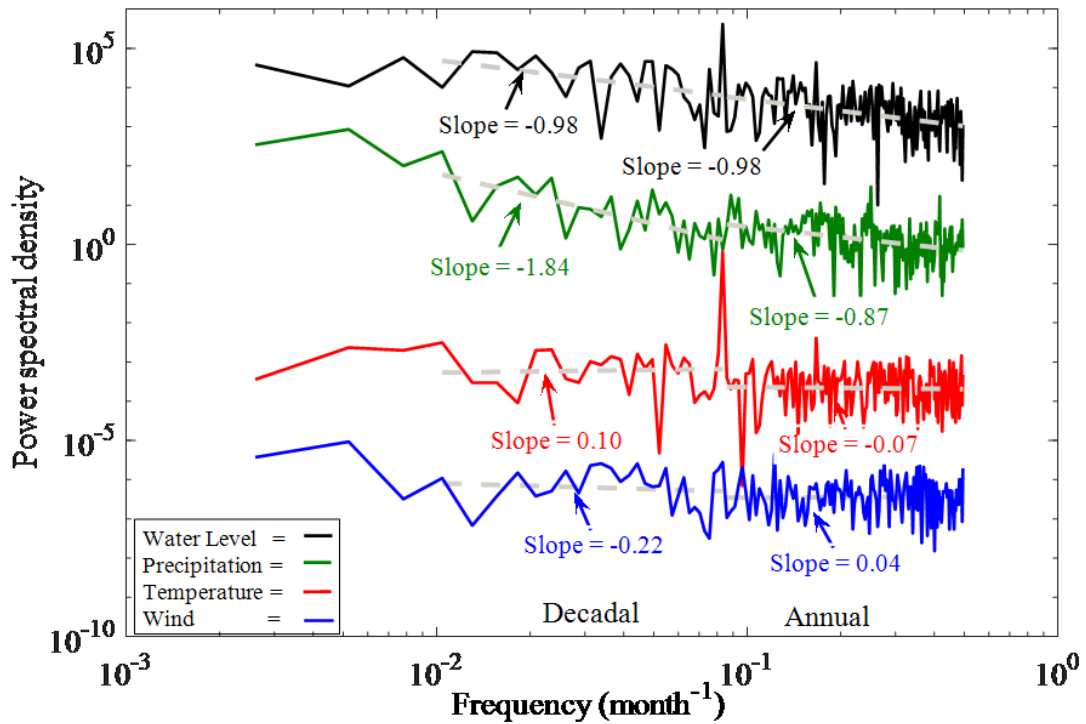
Figure 3.4: Power Spectral Density (PSD) of Water level, Precipitation, Temperature, and Wind. The dashed linear lines represent the slopes of the annual and decadal frequency regimes

Figure 3.4 shows the PSDs of the four hydro-meteorological signals: water level, precipitation, temperature and wind in Apalachicola Bay, which we refer to as forcing mechanisms. For visual comparison, we vertically shifted the PSDs on the log-log plot. Figure 3.4 clearly shows a distinct annual peak for water level and temperature similar to what was observed for the NDVI for the different wetland types (Figure 3.3). The major peak suggests an interdependence between the vegetation dynamics of all wetland types and the annual water level and temperature fluctuation. Figure 3.4 also exhibits steeper spectral slope for water level and precipitation, which indicates that the temporal fluctuations of water level and precipitation were persistent and related by memory. On the other hand, the PSD for temperature and wind were flat suggesting uncorrelated behavior of fluctuations across spatial and temporal scales.

69
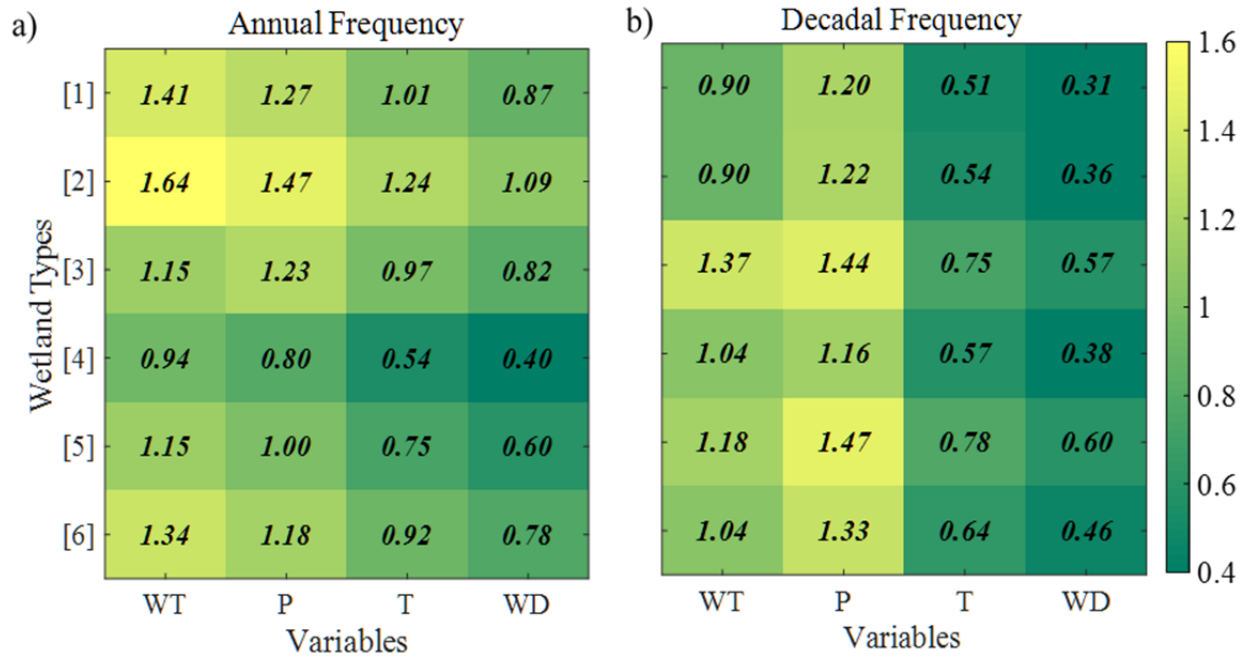
Figure 3.5: Heat-map of cross-spectral (CPSD) slope between NDVI and four hydro-meteorological signals - Water level (WT), Precipitation (P), Temperature (T), and Wind (WD); Color bar shows the magnitude of the CPSD slope. [1], [2], [3], [4], [5] and [6] show the locations of the different wetlands type (see Figure 4.3 a)

Figure 3.5 shows a heat-map of cross-spectral slope obtained from the CPSD analysis between each of the CW NDVI signals and hydro-meteorological signals at the annual Figure 3.5 (a) and decadal Figure 3.5 (b) scales. The slope of the CPSD serves as a measure of the influence of hydro-meteorological signal onto wetland types. The warmer colors indicate a steeper slope, which is suggestive of a more persistent and thus less resilient (Gunderson, 2002; Holling, 1973) relation, between the forcing and response signal. Figure 3.5 shows the largest CPSD slopes for water level and precipitation for all wetland types in both annual and decadal scales indicating that wetlands responded more to the changes in water level and precipitation across all scales compared to wind and temperature. Figure 3.5 also depicts a reverse scenario for the wetland types in two different frequency domains. While annually PFWs responded promptly to the change in hydro-

70

meteorological forcing; PFW responded less on a decadal scale with hydro-meteorological mechanisms. In summary, inland wetlands exhibited more vulnerability at the annual scale while in the decadal scale they were less vulnerable. The PFW, PSEW, PEW and EEW persistence character with respect to hydro-meteorological signals provides valuable information that can be used in supporting local environmental protection agencies.

Components of CPSD analysis, i.e. percentage of amplitude with the major peak, phase lag and corresponding time-lag are shown in Table 3.1. Major peaks in amplitude spectra were identified by using a threshold quantified using smoothed z-score algorithm (Lo et al., 2018; Moore et al., 2018; Perkins & Heber, 2018). The algorithm is based on the principle of dispersion and is robust as it builds a separate moving mean and deviation so that the signals themselves do not pollute the threshold (Lo et al., 2018). Peak or high amplitude indicates a strong correlation between response and forcing signal at that frequency. While there are clear major peaks for temperature and water level, there were none for precipitation and wind did not have major peaks. Precipitation had a minor peak for PEW at location 4 and wind had two minor peaks for PFW at locations 1 and 2 and one minor peak for PEW at location 4 (see Figure 3.1 (a) for locations).

Table 3.1: Summary of cross-spectral (CPSD) analysis between NDVI and different hydro-meteorological signals. Amplitude % was computed as the ratio of amplitude at the peak to the sum of amplitudes at all frequencies. Phase-lag, and time-lag were computed using equations 3.6 and equation 3.7 respectively. Major peak was computed using the smoothed z-score algorithm. In the last column, the square brackets [] represent frequencies corresponding to the % of amplitude

Cross power spectral density (CPSD) Variables	(Major peak) % of Amplitude at annual frequency	Phase-lag (degree)	Time-Lag (months)	(Minor peak) % of Amplitude at other frequencies
Wet 1 vs. temperature	31.6	81.9	2.7	1.0 [Every 1.2 years]
Wet 2 vs. temperature	39.5	62.3	2.1	0.7 [Every 8 years]
Wet 3 vs. temperature	22.0	24.5	0.8	No minor peak
Wet 4 vs. temperature	32.6	32.0	1.1	0.5 [Every 8 years]
Wet 5 vs. temperature	37.4	56.2	1.9	No minor peak
Wet 6 vs. temperature	16.7	50.8	1.7	1.0 [Every 6 years]
Wet 1 vs. water level	11.2	66.0	2.2	2.3 [Every 5 years]
Wet 2 vs. water level	19.1	46.6	1.6	2.3 [Every 8 years]
Wet 3 vs. water level	16.1	39.7	1.3	2.1 [Every 1.6 years]
Wet 4 vs. water level	15.7	26.3	0.9	1.6 [Every 5 years]
Wet 5 vs. water level	17.5	46.6	1.6	No minor peak
Wet 6 vs. water level	14.1	41.8	1.4	1.4 [Every 2 years]
Wet 1 vs. wind	No major peak	N/A	N/A	4.1 [Annual]

Cross power spectral density (CPSD) Variables	(Major peak) % of Amplitude at annual frequency	Phase-lag (degree)	Time-Lag (months)	(Minor peak) % of Amplitude at other frequencies
Wet 2 vs. wind	No major peak	N/A	N/A	7.6 [Annual]
Wet 3 vs. wind	No major peak	N/A	N/A	No minor peak
Wet 4 vs. wind	No major peak	N/A	N/A	5.2 [Annual]
Wet 5 vs. wind	No major peak	N/A	N/A	No minor peak
Wet 6 vs. wind	No major peak	N/A	N/A	No minor peak
Wet 1 vs. precipitation	No major peak	N/A	N/A	2.0 [Every 3 years]
Wet 2 vs. precipitation	No major peak	N/A	N/A	5.1 & 2.4 [Every 8 & 4 years]
Wet 3 vs. precipitation	No major peak	N/A	N/A	3.4 [Every 6 years]
Wet 4 vs. precipitation	No major peak	N/A	N/A	No minor peak
Wet 5 vs. precipitation	No major peak	N/A	N/A	2.13 [Every 8 years]
Wet 6 vs. precipitation	No major peak	N/A	N/A	6.13 [Every 6 years]

The major peak indicated that annually both periodic components of NDVI time-series and temperature time-series are correlated. The phase lag between the annual components of CW NDVIs and temperature ranged from approximately 24 degrees to 81 degrees i.e. 0.8 month to 2.7 months. Our results suggest that the CW NDVI responded with a longer delay of maximum 2.7 months with temperature whereas, it responded with a shorter delay of maximum 2.2 months with water level. The time-lag was obtained using equation 3.7 from the mean phase spectrum over

frequencies within a range of +/-1 month. There was no major peak in the amplitude spectra at any frequency between CW NDVI and precipitation or CW NDVI and wind. Since low amplitude (minor peak) indicate weaker correlations between response and forcing signal, the phase spectrum and consequently time-lag are not significant (i.e. unreliable) for that frequency (see Table 3.1). This analysis can help in understanding key factors such as moderate temperature and water level benefits in CW growth.

3.4   Summary and Conclusions

This study aimed to understand the dynamic nature of various types of coastal wetlands by analyzing the interaction between the hydro-meteorological mechanisms (i.e., water level, precipitation, temperature, wind) that force these dynamics and the corresponding response in the CW NDVI signal. The study also sought to understand the temporal lag between the response and forcing signals. The data used were Landsat derived NDVI, airport and tide station hydro-meteorological data, and an established wetland classification system. A series of empirical methods were implemented to analyze the time-series under different situations.

Based on spectral analysis, on an annual-scale, PFW (inland locations) were found to be more vulnerable to external forcing compared to PSEW, PEW and EEW (coastal locations). However, at the decadal-scale, inland locations were more resilient (i.e. less vulnerable) than coastal locations. The wetland dynamics were mostly driven by water level and precipitation. NDVI exhibited annual periodicity which appeared to be regulated primarily by temperature and water level. Cross-spectral analysis found a time-lag of 0.8 months to 2.7 months between temperature and NDVI and 0.9 months to 2.2 months between water level and NDVI. The characterization of

the persistent behavior across a range of spatial and temporal scales and subsequent understanding that coastal wetland dynamics are mostly driven by water level and precipitation indicated that the severity of droughts, floods, and storm surges will be a driving factor in the future sustainability of coastal wetland ecosystems. For long term projections of coastal wetland dynamics, we recommend that extreme hydrologic events (floods and hurricanes) be incorporated into the model at approximately decadal intervals and that wetland responses to temperature and storm surge events be lagged in time by the values indicated above.

CHAPTER 4: NDVI RECONSTRUCTION FOR IMPROVED COASTAL WETLAND MONITORING USING TRI-SENSOR DATA FUSION: OBSERVATIONS FROM LANDSAT-8, SENTINEL-2A AND ASTER

4.1   Introduction

Availability of free satellite imagery significantly advances simulated constellations of medium resolution sensor data for monitoring earth's coastal and terrestrial systems (Dassenakis et al., 2011; Wulder et al., 2015). Coastal wetlands (CW) have been recognized for their ability to protect shorelines, improve water quality, recharge aquifers, provide nurseries for fisheries, and offer a setting for recreational activities (Ozesmi et al., 2002). Unfortunately, CW are deteriorating due to climate change, human activity and accelerating rates of sea level rise (E. Barbier, 2013; Ozesmi et al., 2002). Due to the protective and non-protective ecosystem services they provide, it is important to conserve these valuable resources.

Satellite remote sensing has many advantages for inventorying and monitoring CW. However, even with high resolution, a single sensor can have limitations in terms of spatial coverage in a selected scene or in a series of scenes that hinders continuous long-term CW monitoring. Therefore, multi-sensor fusion plays an important role in accumulating complementary data from multiple sensors. This is especially useful for CW areas where a single day of full coverage is difficult for a single sensor due to frequent thick clouds (Gordon & Wang, 1994). In this regard, a

potential problem lies in the synergistic use of multiple satellite systems. Fusion of satellite data from multiple sources involves an inherent disruption of harmonizing information due to differences in spatial resolution, spectral ranges, and spectral properties such as band number, position, and width (Ranchin & Wald, 1996). Therefore, finding satellite sensors of similar spatial and spectral properties, especially for CW dynamics analysis, is vital for the coherent fusion of multi-sensor satellite data.

Among the publicly available sensors, Landsat has the longest data record starting from 1984 and has been used extensively for local and global monitoring. Landsat-8 (L8) is the latest generation in the Landsat Data Continuity mission which was launched in 2013. L8 is equipped with Operational Land Imager (OLI) and Thermal Infrared Sensor (TIRS) and both are currently in operation with an orbital revisit time of 16 days (Wulder et al., 2015). The historical record of Landsat imagery is hindered by the cloud and shadow obscurity that affects all similar optical satellite sensors. The temporally sparse time-series of L8 requires complementary data to make the longest satellite time-series more suitable for CW monitoring in applications such as long-term salt marsh change and mapping (Campbell, 2018; SUN, 2015), forest degradation (Ranchin & Wald, 1996), rapid phenology changes (SUN, 2015), and CW degradation (Mo et al., 2017; Tahsin et al., 2016).

Normalized Difference Vegetation Index (NDVI) conveys valuable information relating to CW dynamics (Civco et al., 2006; Tahsin et al., 2016). NDVI is a vegetation index derived from optical remote sensors that characterizes the reflective and absorptive characteristics of vegetation in the red and near infrared (NIR) bands of the electromagnetic spectrum. A chronological analysis of

NDVI with reasonable spatial resolution can indicate changes in CW including coastal marsh vegetation (SUN, 2015). Current optical sensors have sufficient spatial and temporal resolution for NDVI production, but unfortunately image pixels may be obscured by clouds thereby masking critical areas of change. These obscured pixels are one of the principal barriers to effective satellite image interpretation from optical sensors. However, the required high or medium spatial resolution is provided only by panchromatic and multispectral scanners in the reflective spectral range e.g., SPOT, Landsat, Advanced Spaceborne Thermal Emission and Reflection Radiometer (ASTER), Sentinel and SAR sensors. Many of these are commercial and not publicly available to use except at significant cost. Hyperspectral sensors on satellites such as MERIS/ENVISAT-1 could provide additional useful information about biochemical composition of vegetation and waters, mineralogical composition of soils and rocks, surface temperature, water content in vegetation and soil, etc. However, their relatively coarse resolution is not suitable for a local ecosystem change identification and the narrow swath width results in low availability of data for coastal areas, both of which prevent their efficient and widespread utilization for many coastal applications.

Previous researchers have reported many successful applications of sensor fusion among Landsat, MODIS, and Sentinel (Kulawardhana et al., 2007; Roy et al., 2008; Walker et al., 2012). Also, different satellite sensors: Landsat, AVHRR, ASTER, Sentinel, and MODIS have been exploited for the NDVI mapping at local or global scale over the past decades (Cihlar, 1996; Xu & Zhang, 2011; W. Zhu et al., 2012). In spite of the availability of NDVI data from multiple sources, an inherent inconsistency hinders the synergistic use of multi-source NDVI. Many previous researchers have also presented comprehensive literature reviews focused on consistency issues among the inter sensor NDVI data, particularly in the spectral aspect (Fan & Liu, 2018). Since

NDVI is computed using reflectance values in the visible and NIR bands, the issues affecting spectral band data impacts the NDVI calculation. Basically, satellite observations are post-processed to rectify various spatial (Goodin & Henebry, 2002), temporal (Fensholt et al., 2010), radiometric (Roderick et al., 1996), and spectral factors (Galvão et al., 1999). Differences in spatial resolution can add bias to fused NDVI data since it is scale dependent (Jiang et al., 2006).To reduce overall uncertainty, multiple NDVI intercalibration studies agree that the subject and reference sensor data need to be spatially co-registered and resampled (Fan & Liu, 2018). Thus, all sensor data can be compared pixel-to-pixel. After that any physical quantities can be computed via accurate sensor calibration. In the cases of spectral and spatial similarity, multi-sensor data can be used interchangeably (Li et al., 2013; Wulder et al., 2015). In other cases, the results obtained from multi-sensor data are first compared and then used in combination (Wu & Liu, 2014). However, some research gaps remain.

Previous research compared Sentinel-2A (S2A) MSI and L8 OLI data, but did not take into account the misregistration between the sensors (Flood, 2017). While some previous research focused on terrestrial area (desert) only (Li et al., 2017) and used simulated reflectance data (Gorroño et al., 2017), some of their models did not consider large amounts of data from the spatio-temporal domain (Li et al., 2017; Mandanici & Bitelli, 2016). For example, some models were based on fusion of multi-sensor data for pre-selected dates only leaving the model inapplicable to other seasons (Hazaymeh & Hassan, 2015). Other research did not consider more than two satellite systems of similar spectral and spatial features (Walker et al., 2012).

A research gap is clearly present in multiple sensor fusion models that can be applied to any season or any area. Therefore, we propose a tri-sensor fusion (TSF) model that integrates compatible sensors and addresses the sensor inequality issues by utilizing the coincident imagery from a selected four-year time-series. The technique uses both S2A MSI and ASTER synergistically with L8 OLI. The free access to L8, S2A and ASTER, the similar wavelength for bands relevant to NDVI, and similar geographic coordinate systems (Zhu et al., 2015) provide a viable opportunity to combine these three satellite systems for more continuous monitoring of CW areas. ASTER has been used in conjunction with Landsat 5 (L5) to compare two vegetation indices generated by these two sensors. Both NDVI and soil-adjusted vegetation index (SAVI) showed lower spectral vegetation index measurements for ASTER compared to L5 ETM+ for the same target, but still showed a strong positive linear relationship (Xu & Zhang, 2011). Several simulation studies have also shown the potential of combining S2A and L8 [29] as well as L8 and ASTER (Xu & Zhang, 2011). In total, the aforementioned research provides justification for the synergistic use of L8, ASTER and S2A in this study.

Various approaches have been developed for image fusion, such as the intensity-hue-saturation (Tu et al., 2001), principal component analysis (Shettigara, 1992), wavelet decomposition (Nünez et al., 1999), high-pass filter (HPF) (Chavez & Sides, 2002), sparse representation (Wei et al., 2015) and area-to-point regression kriging (ATPRK) methods (Q. Wang et al., 2015). There are several reviews of the available image fusion approaches (Pohl & Van Genderen, 1998; J. Zhang, 2010). Recently, machine learning techniques such as deep learning (Liu et al., 2018) and random forest (RF) (Seo et al., 2018; Tahsin et al., 2017) have gained popularity in image fusion. Motivated by the advantages and encouraging performance in a previous data enhancement technique (Tahsin

et al., 2017), an RF algorithm is proposed here for multi-sensor data adjustment before the fusion of L8, S2A and ASTER data. Our approach in the multi-sensor data environment is to first designate the most ubiquitous sensor with the longest data record as the baseline. In this study, L8 will serve as the baseline. The second component of our approach is to investigate peer sensors for similar spectral features to develop candidates for fusion. Third, the hierarchical fusion workflow is established to produce enhanced cloud-free NDVI that mimics the L8 product.

There are two potential sub-approaches for the fusion task. The first option was to upscale the 20 m S2A Level-1C data and the 15 m ASTER Level-1B data to match the 30 m spatial resolution of L8 Level-1B. S2A Level-1C top-of-atmosphere (TOA) reflectance data is geometrically and radiometrically rectified with orthorectification to generate accurate geolocated products. ASTER Level-1B data contains calibrated at-sensor radiance, which is geometrically corrected and geolocated. The process for upscaling is straightforward but effectively wastes the valuable 20 m information obtained by S2A and 15 m information obtained by ASTER. Since our objective is to enrich the existing L8 with available complementary data, we retained all spatial and spectral characteristics of L8 and modified the other two satellites accordingly. The fusion of L8 with S2A and ASTER data can increase the spatial coverage of data available for continuous monitoring. This is especially beneficial in CW areas where cloud and water vapor masks a high percentage of the data (Martinuzzi et al., 2007). The second option was to compute NDVI from each sensor first before the co-registration and scaling. This approach is called 'index then blend (IB)' (Goyal & Guruprasad, 2018; Jarihani et al., 2014). The IB approach has been found to be computationally more accurate because it mitigates error propagation compared to the alternative (Jarihani et al., 2014).

This paper presents a virtual constellation of NDVI data from three satellite sensors that have similar spectral features: L8, S2A and ASTER. The combined imagery enables NDVI observations of CW at moderate (30 m) spatial resolution similar to L8 with more available spatio-temporal coverage. The novelty in current study lies in the capability of the proposed model to utilize the four years of NDVI imagery altogether to predict NDVI for any selected date irrespective of the season, thus making the TSF model robust and adaptive to seasonal and inter-annual changes. The TSF model will serve as a unique tool for coastal managers to monitor CW changes. The development and testing of the TSF technique are as follows: We discuss the methodology in Section 2, application of proposed method in Section 3, and results in Section 4. After that, a discussion on the proposed TSF model, its application, and limitations are presented in Section 5. Conclusions and recommendations for future work are provided in Section 6.

4.2   Methodology

The TSF methodology is divided into three major components: data collection and pre-processing; model development; and model validation. The components are illustrated in Figure 4.1 a (data collection and pre-processing) and Figure 4.1 b (model development and validation) and discussed in the following sections.
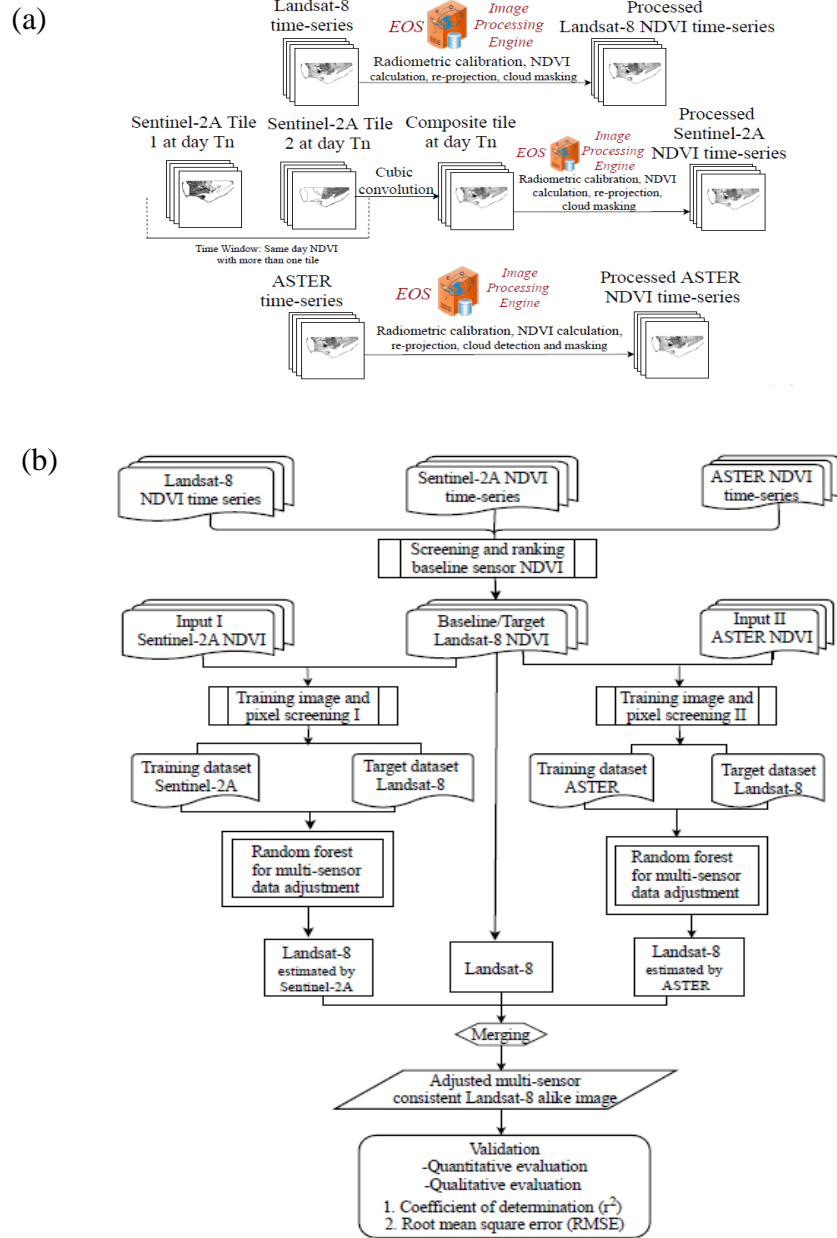
Figure 4.1: Sketch map of TSF flowchart: a) Image pre-processing for Landsat-8, Sentinel-2A and ASTER including compositing Sentinel-2A time-series into a new composite of gap filled (caused by image path overlapping) Sentinel-2A time-series at a pixel-based scale; b) Schematic flowchart of the Tri-sensor fusion (TSF) scheme.

4.2.1   <u>Sensor data collection and pre-processing</u>

L8, S2A and ASTER data from the years 2015 through 2018 were collected for the current study. These years represent the time period (ongoing) where data are available for all three sensors.

Landsat-8 (L8) data were collected from the Earth Observing System (EOS) website (Lenhardt, 2015), for the years 2015 through 2018. L8 was initially known as the Landsat Data Continuity Mission which was launched on February 11, 2013. Similar to the previous generations of Landsat, L8 has a 16-day repeat cycle. L8 satellite carries the Operational Land Imager (OLI) sensor that contains nine spectral bands, including a panchromatic (PAN) band. The visible, near infrared (VNIR) and shortwave infrared (SWIR) bands are 30 m in spatial resolution, while the PAN band is 15 m in spatial resolution. The L8 swath width is 185 km. We downloaded L8 images covering the Paths 19-20, Row 39. While Path 20, Row-39 covers 100% of our study area, Path 19, Row-39 covers almost 50% of the eastern side of the study area. The reason for keeping two different combinations of Paths and Rows, is to accumulate more dates in the temporal domain for training the RF model. A sharp edge is observed in the L8 image for the dates where only one pass (Path 19, Row-39) which covers half of the study area is performed (See Figure 4.2 a).

We pre-processed the L8 data for years 2015 through 2018 using the analytics tool in the EOS cloud-based platform (Lenhardt, 2015). This service removes the need for the user to download and store the data prior to pre-processing locally, making this part of the workflow much more convenient. The L8 data were subjected to the EOS imagery pre-processing pipeline which includes radiometric calibration of digital numbers into at-sensor radiance, raster filters to remove noise, reprojection to a common projection system (UTM zone 16N, WGS 1984), cloud detection

84

and masking. We specified for NDVI computation and further analysis. NDVI was computed using EOS based on band 4 (Red) and band 5 (NIR) reflectances and the resulting NDVI image was produced in geotiff format (Lenhardt, 2015). EOS employs the canonical NDVI formula (Levy, 2000), expressed mathematically as:

$$\text{NDVI} = \frac{(NIR - RED)}{(NIR + RED)} \tag{4.1}$$

Sentinel-2A (S2A) data were also collected from EOS (Lenhardt, 2015). S2A was launched as part of the European Commission's Copernicus program on June 23, 2015. S2A has 13 spectral channels including three VNIR bands with 10 m resolution, two NIR bands with 10 and 20 m resolution. S2A has the widest swath width of the three sensors in TSF at 290 km. Similar to L8, S2A data were collected and pre-processed using EOS for the years 2015 through 2018. Band 8A (NIR) and band 4 (Red) reflectance values were used for S2A NDVI calculation. All available S2A images from tiles T16RFT, T16RGU, T16RGT, T16RFU, and T16RGT were used to produce NDVI images. These 5 tiles combined to cover the full study area, but not all tiles had images captured on all desired dates. Similar to L8, a sharp edge was observed in the S2A image for those dates where less than five of the mentioned tiles are available. Also, S2A data tiles contain some overlap for images acquired on the same date. Image reprojection and cubic convolution resampling technique was done with ArcGIS to estimate the resampled pixel value in the overlapped portion of the S2A input image (Park & Schowengerdt, 1983) (See Figure 4.2 b).
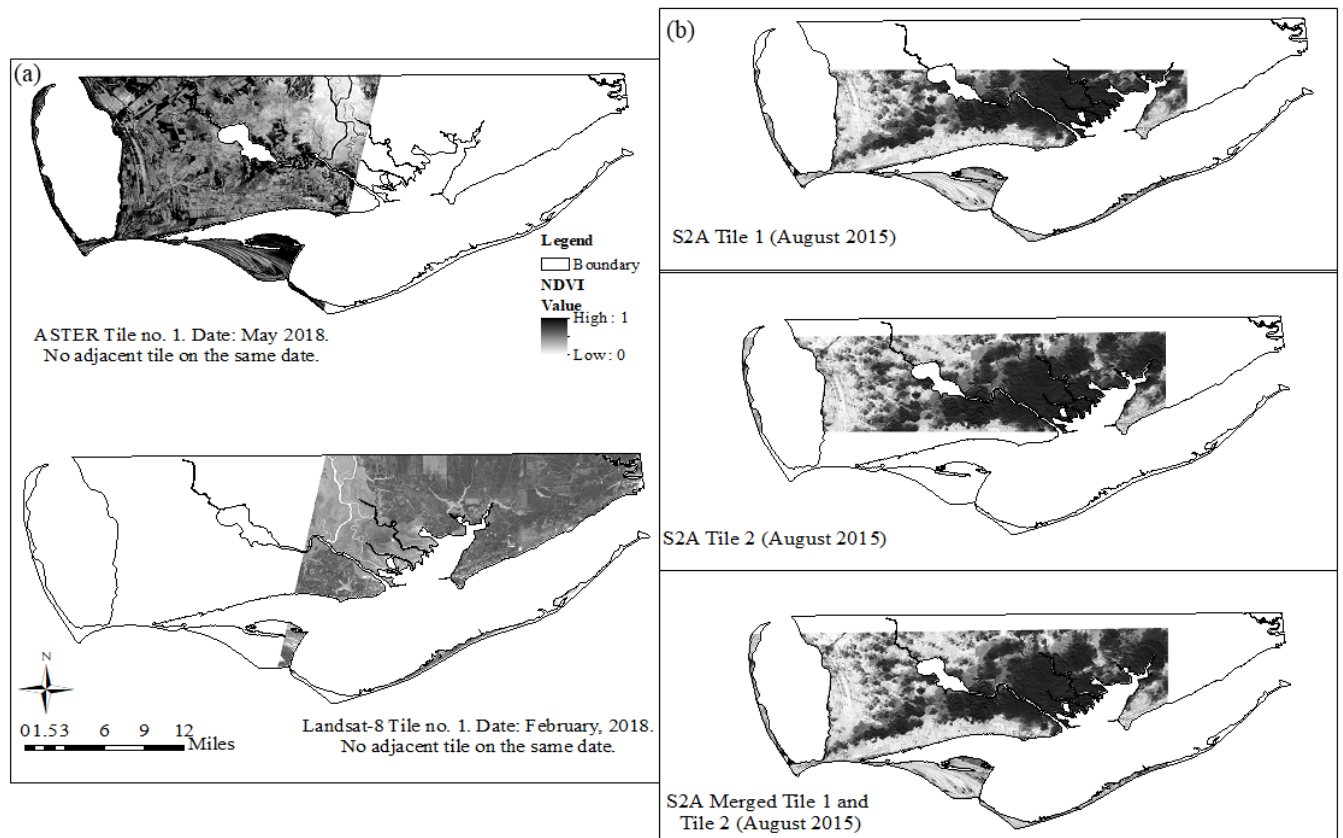
Figure 4.2: a) ASTER tile from May 2018 and Landsat-8 tile from February 2018, no adjacent tiles present on the same date for either sensor;

b) Sentinel-2A tiles merged for August 2015, two overlapping tiles present on the same date.

ASTER data were acquired through the USGS Earth Explorer website from LP-DAAC site (The NASA Land Processes Distributed Active Archive Center (LP DAAC), n.d.). ASTER is a joint operation between National Aeronautics and Space Administration (NASA) and Japan's Ministry of Economy, Trade and Industry (METI). ASTER global observation data has been publicly available since the year 2000. ASTER spectral capabilities include three VNIR bands at 15 m resolution, six SWIR bands at 30 m resolution, five thermal infrared (TIR) bands at 90 m resolution and a NIR band at 15 m resolution. It has the narrowest swath width of the three TSF sensors at

86

60 km. We downloaded all available local granules of ASTER covering the entire spatial extent of the study area. Similar to L8 and S2A, the dates where one or more granules are missing result in a sharp edge in the image. Collecting granules in the same date prevents from overlapping image scenes (See figure 2a). The ASTER data was pre-processed using USGS LP-DAAC Science Processor for Missions (S4PM) (Lynnes, 2007) processing system that also stores ASTER Level 1, 2, and 3 products. The ASTER Level-1B data was used for NDVI computation. The ASTER Level-1B data are available in the Hierarchical Data Format (HDF) and the bands required to compute NDVI are band 3N (Red) and band 8 (NIR). The R (Krehbiel, 2017) package provided by USGS LP-DAAC (The NASA Land Processes Distributed Active Archive Center (LP DAAC), n.d.) was used to convert the HDF data from ASTER Level-1B (which is in UTM) and outputs it as a multi-band geotiff file. NDVI was computed from the pre-processed image using the bands referenced above and equation 4.1.

The collective spatial and spectral similarities of L8, S2A and ASTER enable their synergistic use to map NDVI as a virtual constellation. Since NDVI is calculated using only red and NIR bands, no other bands from the respective satellite sensors were used in the current paper. The spectral characteristics of the L8, S2A and ASTER standard products are listed in Table 4.1.

87

Table 4.1: Parameters of Selected Bands (for NDVI Computation) from Landsat8 (L8), Sentinel-2A (S2A) and the Advanced Spaceborne Thermal Emission and Reflection Radiometer (ASTER).

Satellite/Sensors	Subsystem	Band Number	Spectral Range (µm)	Signal to Noise Ratio (SNR)	Spatial Resolution (m)	Swath Width (km)
Landsat-8 OLI	NIR	Band 5	0.85-0.87	204	30	185
	Red	Band 4	0.63-0.68	227		
Sentinel-2A MSI	NIR	Band 8A	0.86–0.88	72	20	290
	Red	Band 4	0.65–0.68	142	10	
ASTER	NIR	Band 3N	0.78-0.86	202	15	60
	Red	Band 2	0.63-0.69	306		

4.2.2   Tri-Sensor fusion method development

Tri-Sensor Fusion (TSF) model is a remote sensing modeling system that synthesizes three satellite sensors into a virtual constellation. It was built using Matlab and ArcGIS for image processing and Python for TSF operation. The method was developed under two primary assumptions. First, NDVI is a proxy for CW vegetation vigor (Tahsin et al., 2017), therefore a monthly NDVI time series will follow a relatively predictable annual pattern of growth and decline except when influenced by major external forces such as sea level rise (long-term) or hurricane storm surge (short term). Second, inequality of NDVI between different sensors is systematic (Fan & Liu, 2018) or random (Aghakouchak et al., 2012) and the complex relationship can be modeled using long-term historical data (Nay et al., 2018) for all three sensors.

The first objective of TSF is to unify the NDVI scales across the three sensors prior to fusion. Common observations from the three sensors during the coincident time-period provides an opportunity for synergistic inter-sensor comparison. Relationships need to be analyzed pixel by pixel between two sensors at a time. The reason for developing the relationships between two sensors at a time is that each pair of sensors has unique inconsistencies from systematic and random components (Aghakouchak et al., 2012) where the systematic inconsistency comes from different climate conditions or geographical locations of the satellites (Y. Tian et al., 2009) and the random inconsistency comes from multiple sources such as difference in overpass timing, sun angle, sensor mechanism and other sensor specific features. The amount of inconsistency varies between each sensor combination. Traditional linear regression would be the simplest method to establish NDVI relationships between sensors. However, linear regression has previously been shown to be ineffective in capturing complex and non-linear relationships in remote sensing imagery. Therefore, TSF implements a random forest (RF) model similar to Tahsin et al. 2017 (Tahsin et al., 2017). By using four years of monthly imagery data with sufficient temporal overlapping among the sensors, a RF model was developed to predict missing NDVI for L8 pixels obscured by clouds and shadows.

4.2.2.1 Random Forest Model

To establish quantitative relationships between the baseline L8 sensor, and peer sensors S2A and ASTER, we constructed a RF model as a multivariate non-parametric regression method (Breiman, 2001; Rodriguez-Galiano et al., 2015), with peer sensor NDVI values, unique geographic location

(northing (m) and easting (m)) and month of the year from each NDVI time series as predictor variables.

The RF algorithm builds many regression trees (i.e. a forest) based on random subsamples of the training data set. This known as bootstrap aggregation, commonly referred to as bagging, where a random subset is selected with replacement to train the individual trees with the results of the ensemble aggregated by averaging (for regression) or voting (for classification) (Breiman, 2001; Palmer et al., 2007). At each node in the tree, a subset of predictor variables is selected at random and the optimal binary split is computed using the training data subsample and a metric known as "purity." During this procedure, the decision tree progresses through all candidate splits to determine the optimal split that maximizes the purity of the resulting branch. Residual sum of squares (RSS), shown in equation 4.2 is used as the splitting criteria for regression trees.

$$RSS = \sum left \ (y_i - y_L)^2 + \sum right \ (y_i - y_R)^2 \tag{4.2}$$

where, $\sum left \ (y_i - y_L)^2$ and $\sum right \ (y_i - y_R)^2$ refer to the left and right nodes, determined by the binary split.

The RF algorithm is superior in a sense that while classic regression trees are typically "pruned" thus reducing the number of child nodes, according to a specific condition, decision trees in RF grows to maximum purity, constrained by a maximum depth parameter. Each tree sees only part of the training data sets and thus captures only part of the information contained in the entire training data set. The details of RF can be found in (Breiman, 2001). RF is appealing in this application because it inherits some special characteristics such as built-in feature selection capabilities, a means for evaluating the influence of each feature on the algorithm, and relatively

high levels of accuracy in predictions (Palmer et al., 2007). The vital feature of RF is that, using a bootstrap sample of the data, it trains each tree individually. This randomness makes the model more robust than a single decision tree and prevents overfitting the training data. The ensemble of decision trees aggregates predictions of continuous variables by averaging the predictions from all trees (Breiman, 2001). Furthermore, the RF algorithm provides an extra level of randomness and computational efficiency to the bagging process. While nodes of standard decision trees are split by making use of the best possible split from the full list of predictor variables, RF uses a randomly selected subset of these variables; this considerably speeds up the tree growing process. However, in RF every node utilizes the best possible split from the randomly selected subset of predictors at the node. The best splitter might either be just a fairly good splitter, may not be of any help at all or the best overall. In case the splitter is not very helpful, the outcome from the split is two nodes that are basically the same. We suggest that readers look at the figures of (Tahsin et al., 2017) to see an illustration of an ensemble containing three tree and also a detail of one tree from the ensemble.

4.2.3   TSF model validation

The validation starts with comparing the prediction accuracy of the proposed TSF model using RF against a linear regression model. The purpose of this comparison is to demonstrate the superiority of the RF model and justify the added complexity over a simple linear regression model. For quantitative validation of the model, synthetic clouds were developed over areas in an image that have viable NDVI values. This provides labeled data for validation purposes. The images selected for the synthetic cloud validation were purposely excluded from the training and testing data but

were still located in the study area. The statistical measurement used for validation was Root Mean Square Error (RMSE) and Coefficient of Determination (R^2).

Root-Mean-Square Error (RMSE) is defined as:

$$RMSE = \sqrt{\frac{1}{n}\sum_{i=1}^{n}[\hat{T}_i - T_i]^2} \qquad (4.3)$$

Where $\hat{T}_i \ and \ T_i$ represents the observed NDVI and estimated NDVI for pixel i, respectively, and n is the number of pixels in the test set (Jagalingam & Hegde, 2015).

Coefficient of Determination (R^2) is an overall measure of performance when comparing estimated values to observed values. It is defined as:

$$R^2 = \frac{Cov\ (\hat{T}_i,T_i)}{S_{\hat{T}_i},S_{T_i}} \qquad (4.4)$$

Where $Cov\ (\hat{T}_i, T_i)$ is the covariance between $\hat{T}_i$ (Observed NDVI for pixel i) and T_i (estimated NDVI for pixel i); $S_{\hat{T}_i} and\ S_{T_i}$ indicate the standard deviations of $\hat{T}_i \ and \ T_i$ respectively. R^2 measures the linear association between prediction and observation. However, it only provides usable information when data are normally distributed and is sensitive to large values and outliers.

4.3 Application and Testing of TSF in Apalachicola Bay

We conducted our study at Apalachicola Bay, located on the Gulf of Mexico coast in the Florida panhandle (see Figure 4.3). The study area occupies a section of complete L8 scene, Path 19/Row 39, containing a total area of 1053.24 km^2. The study site in Apalachicola Bay is home to rich variety of CW vegetation. CW along the eastern seaboard and Gulf coasts of the United States

have been classified by the National Oceanographic and Atmospheric Administration (NOAA) Coastal Change Analysis Program (C-CAP) (NOAA, 2017; Tahsin et al., 2016). The relevant wetland land cover types in the study area are: palustrine forested wetland (PFW): 54.1%, palustrine emergent wetland (PEW): 7.86%, palustrine scrub and emergent wetlands (PSEW): 11.66%, and estuarine emergent wetland (EEW): 6.48%. Other wetland classes such as estuarine forested wetland, estuarine scrub/shrub wetland are negligible (<1%) in the study area. 19.56% of the study area was comprised of other land uses in addition to wetlands including developed area, agricultural use, and bare land. Apalachicola Bay was chosen as the study area because of its location in a coastal area where clouds are frequently present throughout the year.

Figure 4.3: Study Area Shown in Red Polygon in the Upper Panel and Black Polygon in the Lower Panel.

4.3.1 Selecting the baseline sensor

A baseline sensor is required before image fusion. The baseline sensor is the target sensor while the peer sensors provide complementary observations to the target sensor in an effort to estimated missing data. In the current paper, NDVI derived from three satellite systems (L8, S2A and ASTER) were selected for data fusion. Three primary factors were considered when selecting the baseline sensor: Longest availabile historical data record; maximum overlapping with peer sensors; and minimum percentage of monthly cloud obscured data.

Average monthly cloud cover percentage (i.e., CC) was calculated as the number of cloud obscured pixels by total pixels in the study area in each image. The formula can be written as:

$$Cloud\ Cover\ Percentage\ (CC) = 100 \times \frac{Pixel_{cloud}}{Pixel_{total}} \tag{4.5}$$

Here, $Pixel_{cloud}$ is the number of pixels obscured by clouds; $Pixel_{total}$ is the total number of pixels in the scene.
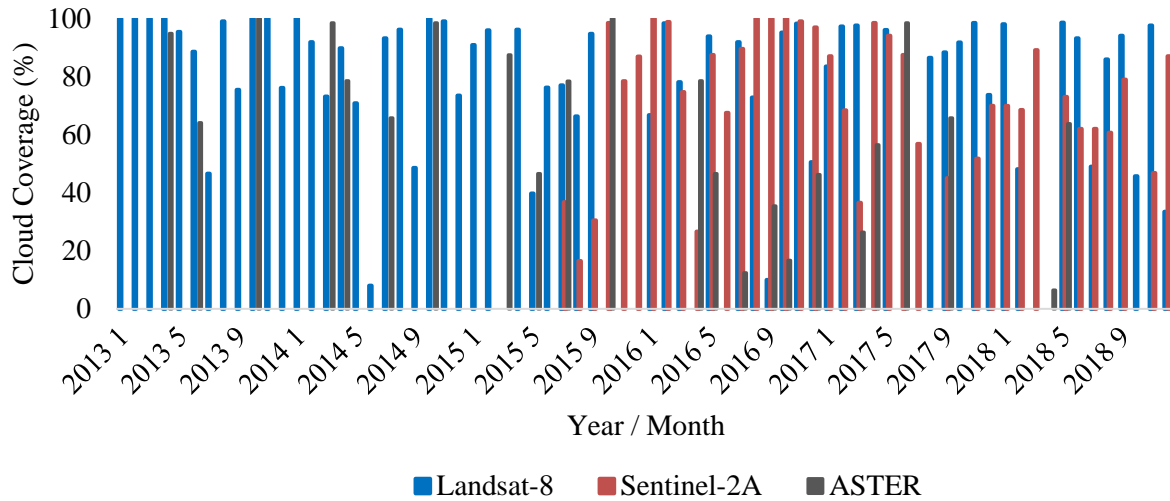
Figure 4.4: Monthly Percentage of Cloud Free Data for L8, S2A and ASTER.

Figure 4.4 shows the timeline of the three sensors with their respective cloud coverage percentages. Landsat (including generations previous to L8) has the longest data record starting from August 1972. ASTER has the next longest record starting from July 2000 and S2A has the shortest records starting from July 2015. Figure 4.4 shows that all three satellites are in operation with their coincident time period beginning in 2015. In the current study we limit the temporal domain from 2015 to 2018 when all three sensors were operational. The greatest benefits among these three sensors are spectral and spatial similarity which reduce the pre-processing and aids in retaining sensor information intact in the peer sensors. Regarding the last criterion for selection of the baseline sensor, L8 has highest percentage (79.72%) of cloud free data while S2A and ASTER have 71.33% and 52.27%, respectively, over the coincident time period from July 2015 to 2018. Therefore, L8 was selected as the baseline sensor over ASTER or S2A. By selecting L8 as the baseline sensor, observations from the peer sensors will be projected onto L8 when necessary. In

other words, the output of TSF will be a repaired L8 image where missing values due to clouds are estimated using S2A and/or ASTER.

4.3.2   Input Preparation

4.3.2.1 Target Variable: L8 NDVI

L8 NDVI imagery is the target for the TSF model. Images in the L8 time-series were clipped to study area boundary using ArcGIS. In performing the TSF, data availability was considered at the pixel level. The L8 cloud mask (Foga et al., 2017), distributed with each image, was used to identify cloudy pixels and calculate cloud cover percentage. An additional filter for negative NDVI values was implemented since NDVI values approaching -1 correspond to open water (Weier & Herring, 2000). Figure 4.5 shows a heat map of usable data in the study area over the selected temporal domain. L8 NDVI imagery is released as a 16-day composite, therefore two images per month are often available. Considering that the month is a predictor variable in the feature vector, when two images were available for a given month the one with less cloud coverage was selected.

90.85	66.78	83.47	98.03
95.93	98.39	97.27	48.09
0.00	78.10	97.62	98.49
96.19	96.41	66.45	0.00
39.73	93.91	96.04	98.63
76.21	75.18	67.64	93.25
77.05	91.87	92.77	49.03
66.35	72.82	36.45	85.99
94.72	9.98	88.38	94.09
0.00	95.19	91.79	45.75
0.00	98.23	98.54	97.65
0.00	50.56	73.67	33.50

Figure 4.5: Percentage of Data Availability in Landsat-8 (L8).

4.3.2.2 Predictor Variables: S2A and ASTER NDVI, Location and Month

S2A and ASTER NDVI values, location (encoded as the northing and easting coordinates of the pixels in meters referenced to UTM Zone 16N, WGS84), and the image acquisition month (encoded as an integer from 1 to 12) were the predictor variables for TSF model. Including location in the feature vector guides the model to estimate a value close to that of the neighboring pixels as well as a plausible value for that pixel in historical and phenological terms.

The pre-processed S2A and ASTER data were clipped to study area and resampled to 30 m using ArcGIS to ensure that each 30 m pixel location was consistent throughout the time series. The SEN2COR cloud mask (Mueller-Wilm et al., 2016) is used for S2A cloud identification. The negative NDVI filter was also used for S2A to mask out pixels corresponding to open water.

In the TSF model organization, S2A data is selected as secondary. The reason for prioritizing S2A with L8 was because S2A has been previously shown to provide adequate continuity for current LANDSAT missions (Topaloğlu et al., 2016). The L8-S2A fused imagery is then ready for tertiary fusion with ASTER if necessary. The TSF model is robust in the sense that in cases of scene unavailability or obscurity for any of these three sensors, the others can be fused into a viable NDVI image In cases where only one sensor is available in addition to L8 (target variable), then the sensor adjustment takes place and the peer sensor (S2A or ASTER) is converted to L8 compatible NDVI values while L8 values remained unchanged. On the other hand, if the baseline target variable L8 is not available, then S2A can be fused with ASTER where both S2A and ASTER transforms to L8 compatible values based on the training data memory. In the event that the only available imagery is a cloudy image from one sensor, then a technique such as Optical Cloud Pixel Recovery (OCPR) can be used to repair the image (Tahsin et al., 2017).

4.3.3   Selection of input for training

It is important to select reliable inputs for the training of any machine learning model, including TSF. The final performance of the final estimator is highly dependent on the quantity and quality of the training data. For TSF, NDVI from L8 are the target data or labels and NDVI from S2A, NDVI from ASTER, northing, easting, and calendar month, easting and northing are predictor data or features. All predictor variables except calendar month are gridded raster products and are therefore spatially variable. Examples of input data records used to train the TSF model are shown in Table 4.2 and Table 4.3.

Table 4.2: Sample Input Data for Training TSF Model - Phase 1.

L8 NDVI Data	Month	Northing (m)	Easting (m)	S2A NDVI Data
0.56	12	701392	3296625	0.69
0.59	12	701422	3296625	0.67
0.62	8	701452	3296625	0.66
0.61	8	701482	3296625	0.68
0.59	8	701512	3296625	0.68
0.53	6	701542	3296625	0.67
0.49	5	701572	3296625	0.64
0.49	4	701602	3296625	0.69
0.49	4	701632	3296625	0.66
0.56	5	701662	3296625	0.66

Table 4.3: Sample Input Data for Training TSF Model – Phase 2.

L8 NDVI Data	Month	Northing (m)	Easting (m)	ASTER NDVI Data
0.59	5	701692	3296625	0.34
0.62	5	701722	3296625	0.26
0.48	7	701752	3296625	0.00
0.55	7	701782	3296625	0.36
0.66	7	701812	3296625	0.38
0.66	8	701842	3296625	0.38
0.62	6	701872	3296625	0.35
0.55	6	701902	3296625	0.36
0.59	6	701932	3296625	0.37
0.58	6	701962	3296625	0.37

4.3.4   Building the prediction model

The random forest algorithm used in the TSF model to project L8 data was implemented in Python using the scikit-learn (sklearn) (Pedregosa & Varoquaux, 2011) module . The GDAL

(GDAL/OGR contributors, 2012) module was used to extract the spatial information associated with the target and predictor variables from geo-referenced images. 70% of the data corpus was randomly selected in both models, without replacement, as the training data with the remaining 30% held out for testing. For the maximum purity of the RF model, the records containing missing predictors (labeled as "zero") were removed. Overall, the construction of the data corpus from the associated imagery took approximately 15+ min on average for each date (approximately 1053.24 km^2) on a non-specialized laptop computer.

4.3.5   Validation and performance metrics

For quantitative validation of the model, hypothetical clouds were created where the underlying image has viable NDVI values in L8. First, a performance matrix was developed for the hypothetical cloud pixels using RF-based TSF model and LR-based TSF model. Data from each season i.e. every 3rd month of year were taken for validation to check for reconstruction bias by season/month. This provides labeled data for validation purposes. The images selected for the hypothetical cloud validation were deliberately excluded from the training and testing data but were still located in the study area.

The TSF model also underwent an additional two-fold validation: 1) by month and 2) by percentage of spatial coverage in a specific image to deepen our understanding about the robustness of the model in terms of seasonality effect, to check for issues related to Simpson's paradox (Tahsin et al., 2017) or any sensitivity to the percentage of image obscured spatial coverage. Hypothetical clouds were created purposefully by extracting percentages of data

systematically from the area to see any potential impact by percentage of spatial coverage in data reconstruction.

4.4 Results

4.4.1 Sensor inequality adjustment

To observe the results of the sensor inequality adjustment, we produced one-to-one scatterplots of observed L8 versus observed S2A and observed ASTER individually, along with their counterpart plots of observed L8 versus adjusted S2A and adjusted ASTER (Figure 4.6). The images used to generate Figure 4.6 was acquired in May 2018. Figure 4.6 (a) and Figure 4.6 (c) clearly show the scale inconsistencies between L8 and observed S2A and between L8 and observed ASTER, respectively. Figure 4.6 (a) shows a positive yet significantly scattered relationship between observed L8 and observed S2A NDVI, while Figure 4.6 (b) shows a much less scattered and positive relationship between observed L8 and adjusted S2A NDVI. Similarly, Figure 4.6 (c) shows a positive and highly scattered relationship between observed L8 and observed ASTER NDVI, while Figure 4.6 (d) shows a much less scattered and positive relationship between observed L8 and observed ASTER NDVI. These visual observations are confirmed by the improved R^2 values between the observed and adjusted S2A and ASTER NDVI plots.
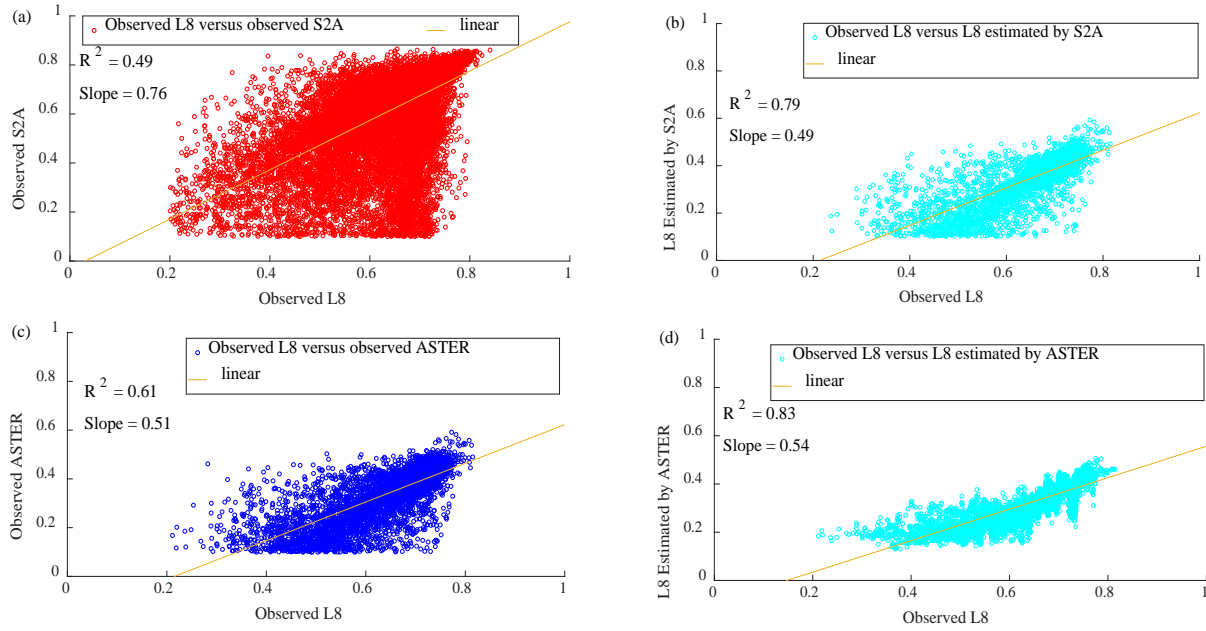
Figure 4.6: Comparison of observed NDVI differences between sensors and subsequent adjustments for selected pixels in May 2018: (a) Observed L8 versus observed S2A; (b) Observed L8 versus L8 estimated by S2A; (c) Observed L8 versus observed ASTER; (d) Observed L8 versus L8 estimated by ASTER.

4.4.2   Data fusion and reconstruction

After TSF, the spatial coverage of L8 NDVI over the study area showed improvement. In February 2018 (Figure 4.7 a), L8 had visible coverage of only 48.08% of the study area. The coverage percentages improved to 100% after fusion with S2A. ASTER did not contribute to this fusion due to complete cloud coverage in its February 2018 image. In September 2016, both S2A and ASTER contributed to the increased spatial coverage of fused L8 NDVI. Before TSF, L8 had a visible coverage of only 9.89%. The visible coverage percentage improved to 33.75% after fusion with S2A and then to 70.86% after fusion with ASTER. The sharp image boundaries in Figure 4.7 represent the absence of an adjacent scene for that sensor in that month or possibly cloud cover although it is unlikely for clouds to form such a regular pattern.
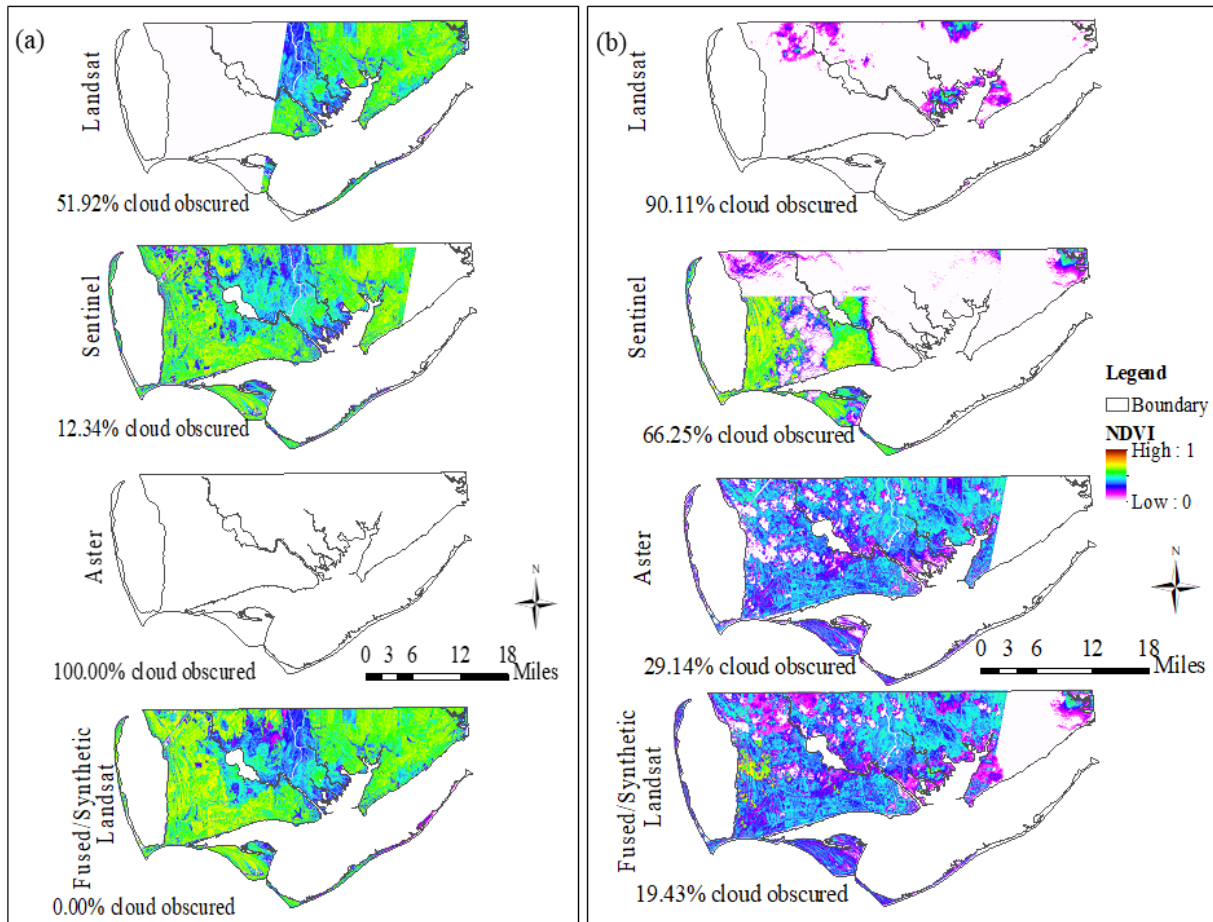
Figure 4.7: TSF performance in (a) February 2018; (b) September 2016.

4.4.3   Analysis of TSF model performance

A large portion of relevant NDVI data is often missing (i.e. see Figure 4.4) from L8 due to heavy

cloud cover in coastal areas. Therefore, to aid in the broader application of long-term continuous

monitoring of CW vegetation dynamics, TSF should be applied improve spatial NDVI coverage.

The RF based TSF model (TSF-RF) was compared with a LR based TSF model (TSF-LR) to

demonstrate the insufficiency of LR and justify the use of RF. Figure 8 shows the fused L8 NDVI

versus observed L8 NDVI for the pixels in testing dataset. Figure 4.8 (a) shows the predictions of

TSF-RF while Figure 4.8 (b) shows TSF-LR. The testing data consists of 30% of the entire data

set, randomly sampled, without replacement (n = 830772). Visually, the plots show that TSF-RF

has a more consistent linear trend across the plotted seasons and a tighter agreement than LR. TSF-

RF has an R^2 value of 0.88 and a clearly positive linear trend while the TSF-LR has a significantly

weaker R^2 value (0.26) and is more scattered around its linear trend, with some visible disjoints

between seasons. Overall, TSF-RF has a RMSE of 0.0020 while TSF-LR has a RMSE of 0.1207.

R^2 and RMSE also suggest that TSF-RF was able to synthesize the missing pixels quite closely in

terms of the absolute magnitude of NDVI. The data shown in Figure 4.8 are also color coded by

month to represent seasonal variations and to investigate the possibility of the model performing

well as a whole while performing poorly in each individual month (Simpson's Paradox). Though

the test data was randomly sampled from the entire data consisting of twelve months, in figure 8

only four months (March, June, September, and December) have been plotted to avoid chaos of

different categories. At the same time represents the seasonal varieties in each quarter of a year.

The colors are well distributed throughout the scatter plot indicating that the model is performing

equally well in all months in addition to the data aggregated over the entire time span.
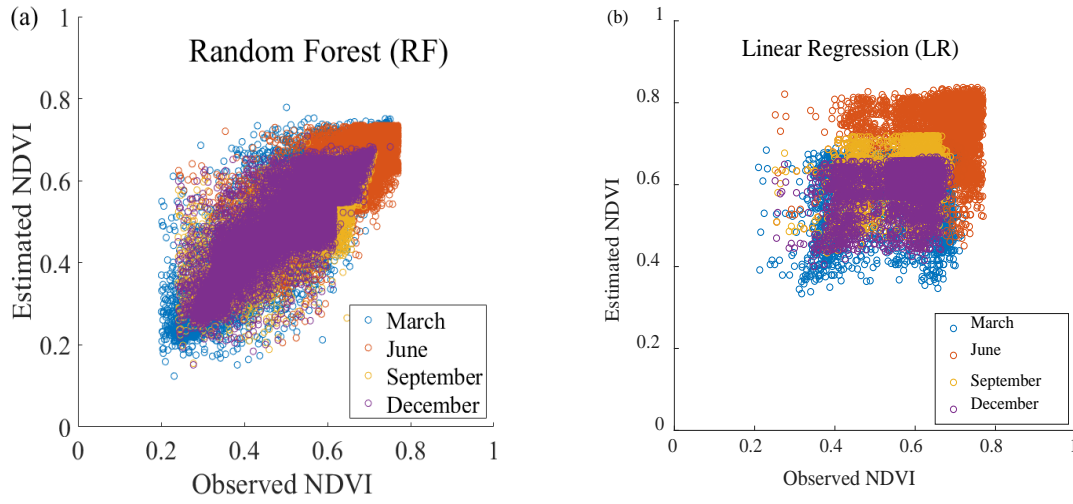
Figure 4.8: Scatter Plots of The Observed and Reconstructed NDVI From the Testing Dataset Using (Left) TSF and (Right) Linear Regression.

4.4.4   Sensitivity of TSF performance to initial L8 cloud cover

TSF was trained and tested using a data corpus where each record corresponds to a labeled (NDVI) pixel with the predictor features explained above. The source images were compiled from the from the imagery associated with L8, S2A, and ASTER from 2015 to 2018. Since each pixel is used as a training record, rather than a vector representing the entire image (i.e. common practice in deep convolutional neural networks), TSF is robust against overfitting to any particular prediction feature, including month. However, in order to determine the effective limit on initial cloud cover in the target L8 image that can be reconstructed using TSF, we tested the methods sensitivity to percent cloud cover by artificially obscuring increasing percentages of pixels from the target L8 image and executing TSF. Table 4.4 shows the performance of TSF obtained under different percentages of cloud covered scenario for a selected image. January 2016 was selected as the test image because it had 0% observed cloud coverage and was therefore a good candidate for validation using hypothetical clouds.

Table 4.4: Sensitivity of TSF performance to percent cloud cover of base L8 image, January 2016

Percentage of cloud cover	Tri-sensor fusion		
	R-Square	RMSE	P-Value
10%	0.8129	0.009648	<0.05
20%	0.8146	0.009669	<0.05
30%	0.8127	0.00949	<0.05
40%	0.8356	0.009557	<0.05
50%	0.8246	0.009474	<0.05
60%	0.8179	0.009457	<0.05
70%	0.8113	0.009548	<0.05
80%	0.8403	0.009457	<0.05
90%	0.8155	0.009546	<0.05
100%	0.8193	0.009581	<0.05

The performance of TSF in reconstructing NDVI data in an L8 image was not sensitive to the initial cloud cover of the base L8 image. Thus, the results showed that TSF produces reasonably accurate reconstructions of cloud-obscured L8 NDVI pixels based on the spatio-temporal attributes of peer and target sensors regardless of season or severity of cloud coverage in the target L8 image.

4.5 Discussion

Sensor fusion can open opportunities for capturing dynamics in CW vegetation by creating spatially and temporally seamless long-term observations. The major hindrance to multi-sensor fusion is inconsistency between coincident images from each sensor and it is important to consider sensors that are compatible in terms of spectral and spatial characteristics. L8 and S2A have the potential for synergistic use that can capture the dynamics of inland waters and nearshore coastal areas at rates that have never been possible before. L8 and S2A data represent the most widely accessible moderate resolution multispectral satellite measurements. ASTER is another medium

resolution sensor that has similar spatial and spectral characteristics as L8 and was successfully used in past synergistically with previous generations of Landsat (Mezned et al., 2007). While multi-sensor NDVI data provide different views of earth surface, it is important to calibrate the sensor differences. Otherwise, the uncorrected NDVI variances will introduce spurious noise into the fusion results (Fan & Liu, 2018).

TSF explicitly addresses this issue by adjusting each complementary sensor separately and fusing them hierarchically (S2A followed by ASTER). The current study provides a quantitative assessment of how TSF can progress the science of developing accurate, seamless NDVI. TSF was developed to synthesize data from three compatible satellite sensors using RF to address the issue of obscured NDVI coverage from a single optical sensor. It takes advantage of the inherent capabilities and efficiencies of RF to characterize the relationship between a labeled outcome (NDVI) and the features that predict it. Inclusion of location (encoded as the northing and easting coordinates of the pixels) into the feature vector encourages the model to predict a value close to that of the neighboring pixels as well as a plausible value for that pixel based on its history. Also, the inclusion of month only (encoded as an integer from 1 to 12) instead of both month and year enhances the model's robustness to seasonality without overfitting to annual scale non-stationarity. Another reason for the selection of RF as the base model for TSF is its ability to estimate prediction error and feature importance simultaneously with model training and testing. This information can effectively guide researchers toward feature inclusion or exclusion as well as tuning the hyperparameters of the RF model (number of features to split on and maximum depth). Table 4.5 shows the feature importance from each RF used in TSF for this study.

Table 4.5: Feature importance for the trained random forest.

ASTER to L8 NDVI		S2A NDVI to L8	
Features	**Importance**	**Features**	**Importance**
ASTER NDVI	0.586	S2A NDVI	0.479
Northing (m)	0.222	Northing (m)	0.275
Easting (m)	0.185	Easting (m)	0.227
Month	0.014	Month	0.024

As shown in Table 4.5, the complementary sensor NDVI is the most important feature followed by position (Northing, Easting). The month contributes much less to the capture of the remaining variability, accounting for only 1% to 2% of the feature importance in the ASTER and S2A models, respectively. It is likely that the month adds a final layer of spatio-historical memory to the overall prediction, but perhaps it is replicating information already known to the model as a result of the complementary sensor NDVI. This is a necessary topic for future work in enhancing TSF.

The results also showed that using multiple linear regression was insufficient to predict L8 NDVI for either complementary sensor. In terms of model training time, LR is significantly faster than RF. However, RF shows much better prediction accuracy than LR in this real-world application and its complexity is justified. It is not known however, whether or not RF is the best machine learning model for this task. Based on the literature, it is certainly a justifiable choice but perhaps as more data are collected, an alternative model such as convolutional neural networks may be a better choice. This is also a promising avenue for future work.

Lastly, the results presented herein certainly show that while TSF improves spatial coverage of obscured L8 NDVI imagery, there are still cases where it cannot reconstruct the image due to lack

of complementary sensor data from S2A or ASTER over all or parts of the target area. In these cases, a model such as OCPR that relies on deeper environmental data and no other sensors can be used. Regardless, TSF model is positive step towards producing spatially and temporally seamless NDVI for long-term CW studies. One crucial application where TSF could be of use is the projection of CW coverage, zonation, and above ground biomass density under sea level rise scenarios (Alizad et al., 2016; Morris et al., 2002; Swanson et al., 2014). A critical component of these studies is the ability to capture the present and past states of CW for validation purposes. These present and past states serve as the basis for future projections and these types of models are highly sensitive to these intial conditions. TSF can be used to establish these initial states by capturing the spatial variability of CW vegetation health over time. It can also be used to validate a CW vegetation model's projection as data are collected in the future.

4.6   Conclusions

This study developed a technique for synergistic use of three optical satellite sensors to increase spatio-temporal coverage of CW NDVI imagery with cloud contaminated pixels. Using a virtual constellation of L8, S2A, and ASTER, enhanced NDVI imagery was produced covering improved spatial coverage. The enhanced NDVI imagery mimics the spatial and spectral properties of L8 product. The salient benefit of using compatible sensor data is the retention of spatial patterns in the newly reconstructed NDVI imagery which is important for change detection in coastal wetland modeling. Using complementary sensor S2A and ASTER NDVI along with prediction features known to influence coastal vegetation growth and vigor (spatial location encoded as northing and easting and month encoded as integer values from 1 to 12), TSF was shown to be capable of reconstructing obscured L8 NDVI imagery with visually plausible and quantitatively accurate

results, even under severe cloud cover. Complementary sensor NDVI and spatial location were the most important features in the model. On the test data set, TSF predicted NDVI values with an RMSE of 0.0020 (NDVI values range from 0 to 1). Also, the R^2 for the observed versus reconstructed NDVI values was 0.8786 (~1.0) indicating good agreement with the observed data.

Random forest was chosen as the base model for TSF because it demonstrated fast and accurate learning capability when characterizing complex time-space-spectrum relationships in real world studies. The proposed random forest based TSF method can recover missing information with high efficacy. We therefore we predict that it can eventually be scaled for operational use as all the included sensors develop to maturity, and others are brought online.

It should be noted that the TSF method was limited by the availability of the historical time series to characterize the complex time–spatial–spectral relationships between the L8 and peer sensor data over the multiple parameters in a specific region. Also, the peer sensor data are currently not available over the same time period as the baseline L8 NDVI. As with any machine learning model, including TSF, its performance is heavily dependent on its training data. Improvements can be achieved by further optimizing the training algorithms and architectures of the random forest with the new ideas for treating missing values in the predictor variable data sets. Focusing on screening and selecting suitable peer sensors as inputs for the TSF models is critical to the prediction accuracy. Also, the authors strongly recommend that the outer boundary of area selected for training lie well outside the area of interest to avoid edge or boundary effects, considering the importance of spatial location on the reconstructed values. Despite these limitations, the idea of spatial information recovery via machine learning provides a promising and efficient approach to

mitigate and eliminate cloud contamination with enough accuracy to facilitate long-term remote

sensing based coastal wetland studies.

CHAPTER 5: CONCLUSION

5.1   Conclusion

A 15-year long time series NDVI was analyzed to evaluate the impact of hydrologic event on CWs stresses. Such analysis with long-term data is much more credible compared to single event based before-after analyses that bring potential doubt about non-uniformity for all similar events. NDVI is a widely used index to measure density of live green vegetation at global and regional scale. In general, the impact of extreme hydrological events (EHEs) such as hurricane and droughts on CWs can range from massive to very small. The recovery time for vegetation after impact from these EHEs can be highly variable depending on the hazard type and intensity. We investigated the impact of hurricane and drought on both freshwater and saltwater wetlands from year 2000 to 2015 in Apalachicola Bay. Our results indicated that saltwater wetlands are more resilient than freshwater wetlands and suggested that in response to hurricanes, the coastal wetlands took almost a year to recover, while recovery following a drought period was observed after only a month (Tahsin et al., 2016).

The 15-year long NDVI time-series was extended to a 30-year NDVI time-series to evaluate the impact of hydro-meteorological signals on CWs responses. NDVI response was compared against forcing hydro-meteorological variables. The database ranged from the year 1984 to 2015 and included hydro-meteorological data in the same temporal domain for Apalachicola Bay, Florida. Spectral analysis of these data allows for the characterization of persistence properties in the signal. Spectral analysis exhibited a difference in persistency against EHEs between inland and coastal locations of CWs at annual-scale and decadal scale. At annual scale inland CWs (PFW) were more

vulnerable to external forcing than coastal CWs (PSEW, PEW and EEW). However, at the decadal-scale, inland locations were less vulnerable than coastal locations. Cross-spectral analysis found a time-lag of 0.8 months to 2.7 months between NDVI response towards temperature fluctuation and a time-lag of 0.9 months to 2.2 months between NDVI response towards water level fluctuation. The understanding that coastal wetland dynamics are mostly driven by water level and precipitation provided ample indication that the severity of droughts, floods, and storm surges will be a driving factor in the future sustainability of CWs.

The analysis was based on optical sensor derived data. Therefore, the NDVI time-series was temporarily sparse with a lot of missing months in those years. Though empirical S-G filter was used to fill the gap NDVI in the months of missing data, it considered only temporal observations to predict the missing values within a selected window. It is to be noted that we used the filter to predict mean NDVI instead of pixel-by-pixel NDVI. We utilized the processed long time-series (30-years) and multi-variable data. The large dataset was used in machine learning techniques to reconstruct missing data which is a less investigated method. Against this backdrop, this research proposed a novel methodology and applied it firstly to fuse data from multiple sensors and secondly by applying a data enhancement technique to recover the information contaminated by cloud cover.

The last part of this study innovated a novel tri-sensor fusion (TSF) method, that synergistically use three satellite sensors to increase spatial coverage of CWs NDVI data obscured by cloud, using optical remote sensing imagery. The main idea was to fuse sensors of similar spatial and spectral features to use data after adjustment. Peer sensor NDVI data, spatial location (northing and

easting), and month were kept as predictor variables. TSF was shown to be capable of gaining spatial coverage with visually plausible and quantitatively accurate results. As the performance of any machine learning model is heavily dependent on its training data, more training data helps model training and performances. Due to common points in a specific day among three sensors were low in number, we used all NDVI data and corresponding peer sensors data to form the model. TSF improved the spatial coverage in NDVI, yet some days still had missing portion. Therefore, another data reconstruction model was required.

To recover data in the absence of any other available satellite sensor, the study proposed and applied a data reconstruction method for missing pixel recovery using supplementary data for NDVI. A novel and unique Optical Cloud Pixel Recovery (OCPR) method was proposed and applied in Apalachicola Bay. Multi parameter 30-year time series data were used to reconstruct missing data in NDVI reflectance in Landsat data based on the well-known machine learning approach of random forest (RF). OCPR method enabled to devise the cloud repair in a step by step strategy towards final estimation. Temperature, precipitation, water level, month, spatial locations were selected as predictor variable to define the NDVI. While TSF increased spatial coverage with a visually and quantitatively plausible results, OCPR filled the remaining gap with reasonable accuracy.

5.2 Future Research Scope

Future research opportunities in coastal wetland ecosystem (CWE) will involve both maximum utilization of existing satellite remote sensors as well as incorporation of extreme events in existing climate models. The characterization of the persistent behavior across a range of spatial and

114

temporal scales and subsequent understanding that coastal wetland dynamics are mostly driven by water level and precipitation indicated that the severity of droughts, floods, and storm surges will be a driving factor in the future sustainability of coastal wetland ecosystems. It is very important therefore to incorporate extreme events in modeling coastal processes such as salt marsh mapping, and CWE degradation. For long term projections of coastal wetland coverage dynamics, we recommend that extreme hydrologic events (floods and hurricanes) be incorporated into the model at approximately decadal intervals and that wetland responses to temperature and storm surge events be lagged in time by the values indicated above. Time-lag values such as wetland responses to temperature and storm surge events be lagged in time by 2.7 and 2.2 respectively and the time-lag need to be input for any relevant model development if used as input.

In the data reconstruction models, RF shows much better prediction accuracy than linear regression (LR) in this real-world application. It is not known however, whether RF is the best machine learning model for this task. Based on the literature, it is certainly a justifiable choice but perhaps as more data are collected, an alternative model such as convolutional neural networks may serve as a better choice and promising avenue for future work. TSF method training depends on data availability from the 4 years' time-series. Given more complementary sensors, the prediction accuracy will be improved and therefore data need to be explored for multi-sensor fusion. A critical component of these studies is the ability to capture the present and past states of CW for validation purposes. The present and past states of CW serve as the basis for future projections and the prediction models are highly sensitive to initial conditions of the chosen parameters. TSF can be used to establish these initial states by capturing the spatial variability of CW vegetation health

over time. It can also be used to validate a CW vegetation model's projection as data are collected in the future.

APPENDIX: LIST OF FIGURES
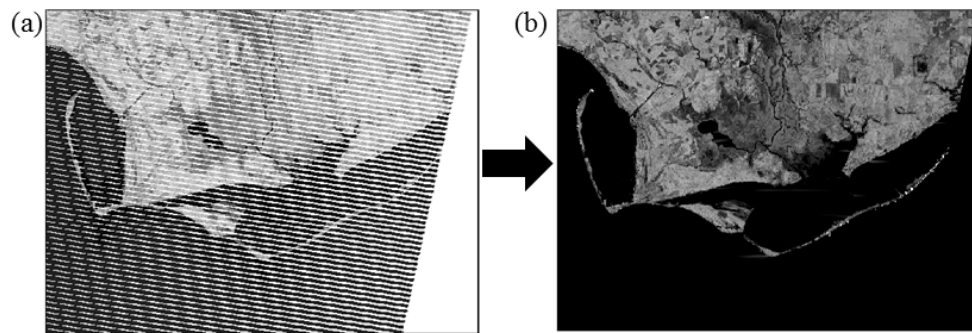
Landsat data pre-processing: a) An example of Landsat-7 NDVI reflectance data obscured by stripping; b) Landsat-7 NDVI de-stripping and regaining missing data beneath the stripes
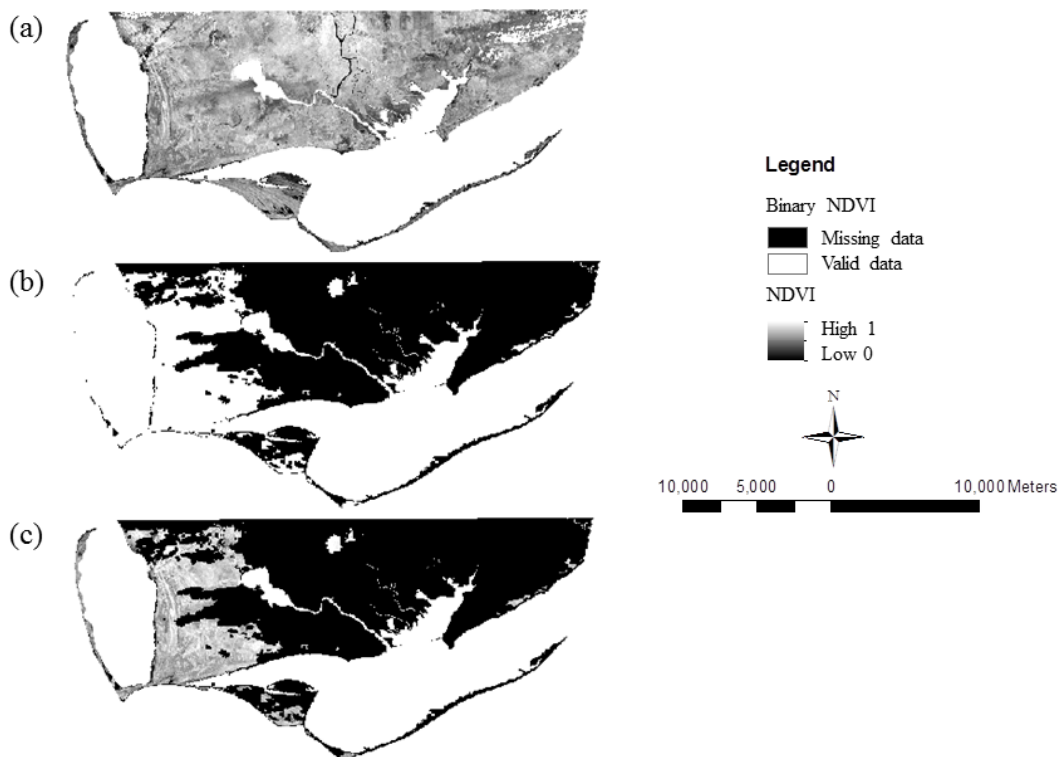
Landsat NDVI reflectance data using "cfmask" layer provided by Landsat NDVI Cloud masking (a) raw NDVI reflectance data (b) binary cloud mask layer (c) final NDVI reflectance after adjusting cloudy and noisy data using "cfmask"
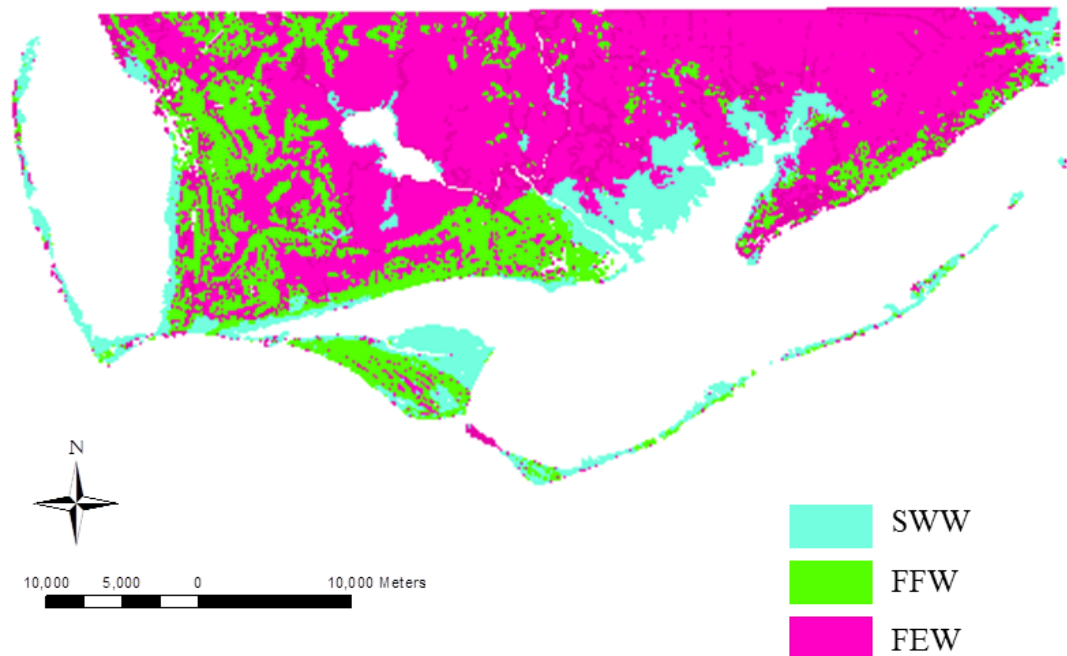
Study area: The Apalachicola Bay in Florida. Wetlands has been re-classified in three classes from the original twenty-four classes defined by National Oceanic and Atmospheric Administration (NOAA) Coastal Change Analysis Program (C-CAP)
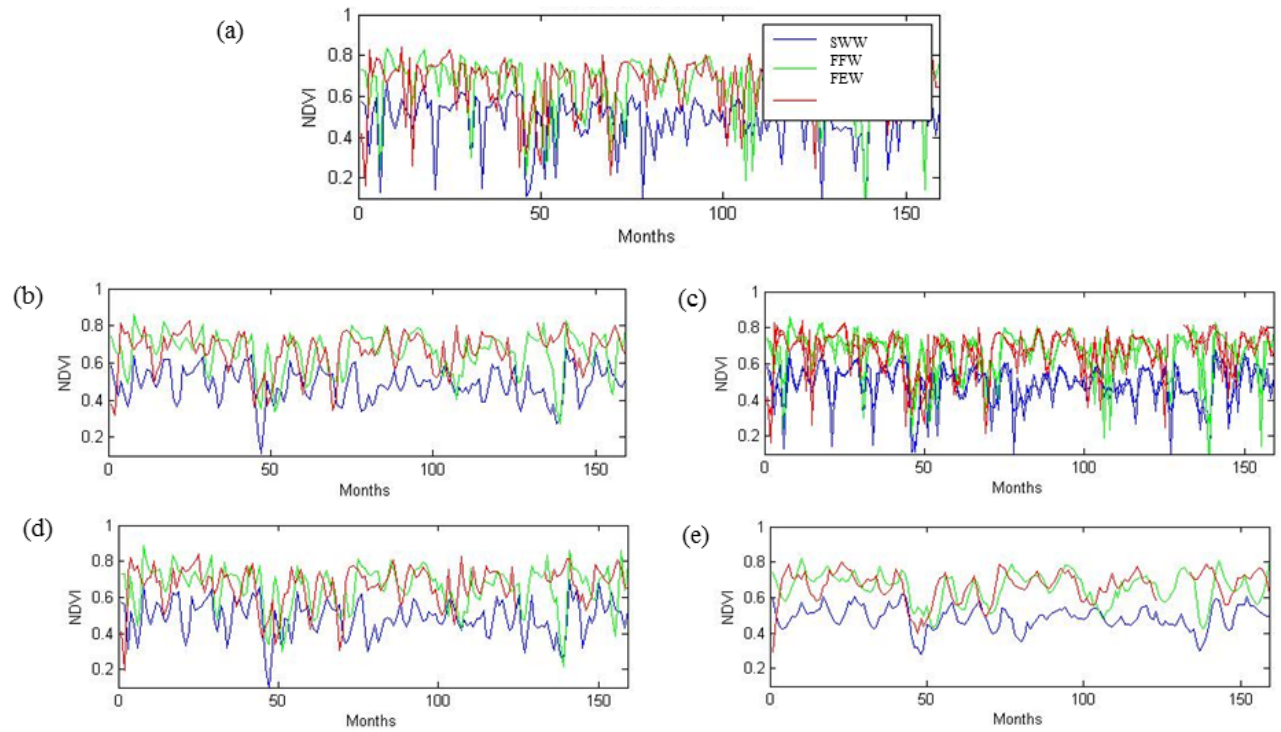
**Comparison of filtered data using S-G filters using different degree and window size. a)
Observed NDVI from time series (2000-2015); b) Filtered NDVI with Degree 3, moving
window size 5; c) Filtered NDVI with Degree 2, moving window size 3; c) Filtered NDVI
with Degree 5, moving window size 7; d) Filtered NDVI with Degree 3, moving window size
9.**

LIST OF REFERENCES

Abed-Elmdoust, A., Miri, M. A., & Singh, A. (2016). Reorganization of river networks under changing spatiotemporal precipitation patterns: An optimal channel network approach. *Water Resources Research*. https://doi.org/10.1002/2015WR018391

Aber, J. (2004). Lighter-than-air Platforms for Small-format Aerial Photography. *Transactions of the Kansas Academy of Science*, *33*(11), 3373–3401. https://doi.org/10.1038/108292b0

Adam, P. (1990). *Saltmarsh ecology. Cambridge University Press*.

Adams, S. M., Friedland, C. J., & Levitanc, M. L. (2009). Unmanned Aerial Vehicle Data Acquisition for Damage Assessment in Hurricane Events. *Remote Sensing for Disaster Management*, *30*. Retrieved from http://www.enveng.titech.ac.jp/midorikawa/rsdm2010_pdf/13_adams_paper.pdf

Aghakouchak, A., Mehran, A., Norouzi, H., & Behrangi, A. (2012). Systematic and random error components in satellite precipitation data sets. *Geophysical Research Letters*. https://doi.org/10.1029/2012GL051592

Alizad, K., Hagen, S. C., Morris, J. T., Bacopoulos, P., Bilskie, M. V., Weishampel, J. F., & Medeiros, S. C. (2016). A coupled, two-dimensional hydrodynamic-marsh model with biological feedback. *Ecological Modelling*, *327*, 29–43. https://doi.org/10.1016/j.ecolmodel.2016.01.013

Alizad, K., Hagen, S. C., Morris, J. T., Medeiros, S. C., Bilskie, M. V., & Weishampel, J. F. (2016). Coastal wetland response to sea-level rise in a fluvial estuarine system. *Earth's Future*, *4*(11), 483–97. https://doi.org/10.1002/2016EF000385

Bak, P., Tang, C., & Wiesenfeld, K. (1987). Self-organized criticality: An explanation of the 1/f noise. *Physical Review Letters*, *59*(4), 381. https://doi.org/10.1103/PhysRevLett.59.381

Bao, Y. H., & Ren, J. (2011). Wetland landscape classification based on the BP neural network in DaLinor Lake area. In *Procedia Environmental Sciences*. https://doi.org/10.1016/j.proenv.2011.09.368

Barbier, E. (2013). Valuing Ecosystem Services for Coastal Wetland Protection and Restoration: Progress and Challenges. *Resources*, *2*(3), 213–230. https://doi.org/10.3390/resources2030213

Barbier, E. B., Hacker, S. D., Kennedy, C., Koch, E. W., Stier, A. C., & Silliman, B. R. (2011). The value of estuarine and coastal ecosystem services. *Ecological Monographs*, *81*(2), 169–193. https://doi.org/10.1890/10-1510.1

Barducci, A., Guzzi, D., Marcoionni, P., & Pippi, I. (2009). Aerospace wetland monitoring by

hyperspectral imaging sensors: A case study in the coastal zone of San Rossore Natural Park. *Journal of Environmental Management*, *90*(7), 2278–2286. https://doi.org/10.1016/j.jenvman.2007.06.033

Barras, J. A., Brock, J. C., Morton, R. A., & Travers, L. J. (2010). *Remotely Sensed Imagery Revealing the Effects of Hurricanes Gustav and Ike on Coastal Louisiana, 2008*. https://doi.org/https://pubs.usgs.gov/ds/566/

Bartsch, a, Wagner, W., Scipal, K., Pathe, C., Sabel, D., & Wolski, P. (2009). Global monitoring of wetlands--the value of ENVISAT ASAR Global mode. *Journal of Environmental Management*, *90*(7), 2226–2233. https://doi.org/10.1016/j.jenvman.2007.06.023

Berhane, T. M., Lane, C. R., Wu, Q., Anenkhonov, O. A., Chepinoga, V. V., Autrey, B. C., & Liu, H. (2018). Comparing pixel- and object-based approaches in effectively classifying wetland-dominated landscapes. *Remote Sensing*. https://doi.org/10.3390/rs10010046

Bilskie, M. V., Hagen, S. C., Alizad, K., Medeiros, S. C., Passeri, D. L., Needham, H. F., & Cox, A. (2016). Dynamic simulation and numerical analysis of hurricane storm surge under sea level rise with geomorphologic changes along the northern Gulf of Mexico. *Earth's Future*, *4*(5), 177–193. https://doi.org/10.1002/2015EF000347

Birkett, C. (1995). The global remote sensing of lakes, wetlands and rivers for hydrological and climate research. In *IGARSS'95.'Quantitative Remote Sensing for Science and Applications* (pp. 1979–1981). Firenze, Italy, Italy: IEEE. https://doi.org/10.1109/IGARSS.1995.524084

Bourgeau-Chavez, L. L., Smith, K. B., Brunzell, S. M., Kasischke, E. S., Romanowicz, E. a., & Richardson, C. J. (2005). Remote monitoring of regional inundation patterns and hydroperiod in the Greater Everglades using Synthetic Aperture Radar. *Wetlands*, *25*(1), 176–191. https://doi.org/10.1672/0277-5212(2005)025[0176:RMORIP]2.0.CO;2

Breiman, L. (2001). Random forests. *Machine Learning*, *45*(1), 5–32.

Byrd, K. B., Ballanti, L., Thomas, N., Nguyen, D., Holmquist, J. R., Simard, M., & Windham-Myers, L. (2018). A remote sensing-based model of tidal marsh aboveground carbon stocks for the conterminous United States. *ISPRS Journal of Photogrammetry and Remote Sensing*, *139*, 255–271. https://doi.org/10.1016/j.isprsjprs.2018.03.019

Cahoon, D. R., Reed, D. J., Day, J. W., Steyer, G. D., Boumans, R. M., Lynch, J. C., et al. (1995). The influence of Hurricane Andrew on sediment distribution in Louisiana coastal marshes. *Journal of Coastal Research*, *1995*, 280–294.

Campbell, A. D. (2018). *Monitoring salt marsh condition and change with satellite remote sensing*. University of Rhode Island. https://doi.org/Paper 793. https://digitalcommons.uri.edu/oa_diss/793

Campbell, J. B., & Mryka Hall-Beyer. (1997). Introduction to remote sensing. *Cartographica* , *34*(1), 70.

La Cecilia, D., Toffolon, M., Woodcock, C. E., & Fagherazzi, S. (2016). Interactions between river stage and wetland vegetation detected with a Seasonality Index derived from LANDSAT images in the Apalachicola delta, Florida. *Advances in Water Resources*, *89*, 10–23. https://doi.org/10.1016/j.advwatres.2015.12.019

Chambers, J. Q., Fisher, J. I., Zeng, H., Chapman, E. L., Baker, D. B., & Hurtt, G. C. (2007). Hurricane Katrina's carbon footprint on U.S. Gulf Coast forests. *Science*, *318*(5853), 1107–1107. https://doi.org/10.1126/science.1148913

Chaouch, N., Temimi, M., Hagen, S., Weishampel, J., Medeiros, S., & Khanbilvardi, R. (2012). A synergetic use of satellite imagery from SAR and optical sensors to improve coastal flood mapping in the Gulf of Mexico. *Hydrological Processes*, *26*(11), 1617–1628. https://doi.org/10.1002/hyp.8268

Chapple, D., & Dronova, I. (2017). Vegetation Development in a Tidal Marsh Restoration Project during a Historic Drought: A Remote Sensing Approach. *Frontiers in Marine Science*. https://doi.org/10.3389/fmars.2017.00243

Chavez, P. S., & Sides, S. C. (2002). Comparison of Three Different Methods to Merge Multiresolution and Multispectral Data: LANDSAT TM and SPOT Panchromatic: ABSTRACT. *AAPG Bulletin*, *57*(3), 295–303. https://doi.org/10.1306/44b4c288-170a-11d7-8645000102c1865d

Chen, X., Zong, Y., Zhang, E., Xu, J., & Li, S. (2001). Human impacts on the Changjiang (Yangtze) River basin, China, with special reference to the impacts on the dry season water discharges into the sea. *Geomorphology*, *41*(2–3), 111–123. https://doi.org/10.1016/S0169-555X(01)00109-X

Cihlar, J. (1996). Identification of contaminated pixels in AVHRR composite images for studies of land biosphere. *Remote Sensing of Environment*, *56*(3), 149–163.

Civco, D., Hurd, J., Prisloe, S., & Gilmore, M. (2006). Characterization of coastal wetland systems using multiple remote sensing data types and analytical techniques. In *IEEE International Symposium on Geoscience and Remote Sensing* (pp. 3442–3446). https://doi.org/10.1109/IGARSS.2006.883

Clinton, N., Yu, L., Fu, H., He, C., & Gong, P. (2014). Global-scale associations of vegetation phenology with rainfall and temperature at a high spatio-temporal resolution. *Remote Sensing*, *6*(8), 7320–7338. https://doi.org/10.3390/rs6087320

Conner, W., & Buford, M. A. (1998). *Southern Forested Wetlands*. (Michael G. Messina & William H. Conner., Eds.). Boca Raton, Boston, New York, Washington, London: CRC Press LLC.

Costa, M. P. F. (2004). Use of SAR satellites for mapping zonation of vegetation communities in the Amazon floodplain. *International Journal of Remote Sensing*, *25*(10), 1817–1835. https://doi.org/10.1080/0143116031000116985

Costa, M. P. F., Niemann, O., Novo, E., & Ahern, F. (2002). Biophysical properties and mapping of aquatic vegetation during the hydrological cycle of the Amazon floodplain using JERS-1 and Radarsat. *International Journal of Remote Sensing*, *23*(7), 1401–1426. https://doi.org/10.1080/01431160110092957

Cowardin, L. M., Carter, V., Golet, F. C., & LaRoe, E. T. (1979). *Classification of wetlands and deepwater habitats of the United States. FGDC-STD-004-2013. Second Edition*. https://doi.org/FWS/OBS-79/31

Dassenakis, M., Paraskevopoulou, V., Cartalis, C., Adaktilou, N., & Katsiabani, K. (2011). Remote sensing in coastal water monitoring: Applications in the eastern Mediterranean Sea (IUPAC Technical Report). *Pure and Applied Chemistry*, *84*(2), 335–375. https://doi.org/10.1351/pac-rep-11-01-11

Day, J. W. J. W. J. W., Christian, R. R. R., Boesch, D. M. D. M., Yáñez-Arancibia, A., Morris, J., Twilley, R. R. R. R., et al. (2008). Consequences of climate change on the ecogeomorphology of coastal wetlands. *Estuaries and Coasts*, *31*(3), 477–491. https://doi.org/10.1007/s12237-008-9047-6

Dinerstein, E., Weakley, A., Noss, R., Snodgrass, R., & Wolfe. K. (2019). Florida sand pine scrub. Retrieved February 19, 2019, from https://www.worldwildlife.org/ecoregions/na0513

Dor, E. Ben, Malthus, T., Plaza, A., & Schläpfer, D. (2012). *Hyperspectral Remote Sensing. Airborne Measurements for Environmental Research: Methods and Instruments*. SPIE.

Ericson, J. P., Vörösmarty, C. J., Dingman, S. L., Ward, L. G., & Meybeck, M. (2006). Effective sea-level rise and deltas: Causes of change and human dimension implications. *Global and Planetary Change*, *50*(1–2), 63–82. https://doi.org/10.1016/j.gloplacha.2005.07.004

Fan, X., & Liu, Y. (2018). Multisensor Normalized Difference Vegetation Index Intercalibration: A Comprehensive Overview of the Causes of and Solutions for Multisensor Differences. *IEEE Geoscience and Remote Sensing Magazine*. 4: 23-45. https://doi.org/10.1109/MGRS.2018.2859814

Feder, J. (1988). *The Fractal Dimension*. Springer. https://doi.org/10.1016/B978-0-12-079061-6.50010-3

Feng, Y., Negron-juarez, R. I., Patricola, C. M., Collins, W. D., Uriarte, M., Hall, J. S., et al. (2018). Rapid remote sensing assessment of impacts from Hurricane Maria on forests of Puerto Rico. *PeerJ Preprints*. https://doi.org/10.7287/peerj.preprints.26597v1

Fensholt, R., Sandholt, I., Proud, S. R., Stisen, S., & Rasmussen, M. O. (2010). Assessment of MODIS sun-sensor geometry variations effect on observed NDVI using MSG SEVIRI geostationary data. *International Journal of Remote Sensing*, *31*(23), 6163–6187. https://doi.org/10.1080/01431160903401387

Flood, N. (2017). Comparing Sentinel-2A and Landsat 7 and 8 using surface reflectance over

Australia. *Remote Sensing*, *9*(7), 659. https://doi.org/10.3390/rs9070659

Foga, S., Scaramuzza, P. L., Guo, S., Zhu, Z., Dilley, R. D., Beckmann, T., et al. (2017). Cloud detection algorithm comparison and validation for operational Landsat data products. *Remote Sensing of Environment*, *194*, 379–390. https://doi.org/10.1016/j.rse.2017.03.026

Foley, J. A., Kutzbach, J. E., Coe, M. T., & Levis, S. (1994). Feedbacks between climate and boreal forests during the Holocene epoch. *Nature*, *371*(6492), 52. https://doi.org/10.1038/371052a0

Galvão, L. S., Vitorello, Í., & Almeida Filho, R. (1999). Effects of band positioning and bandwidth on NDVI measurements of Tropical Savannas. *Remote Sensing of Environment*, *67*(2), 181–193. https://doi.org/10.1016/S0034-4257(98)00085-6

GDAL/OGR contributors. (2012). GDAL/OGR Geospatial Data Abstraction software Library. *Official Web Page*, 87–104. Retrieved from http://www.gdal.org/

Ghamisi, P., Couceiro, M. S., & Benediktsson, J. A. (2015). A novel feature selection approach based on FODPSO and SVM. *IEEE Transactions on Geoscience and Remote Sensing*. https://doi.org/10.1109/TGRS.2014.2367010

Goetz, A. F. H. (2009). Three decades of hyperspectral remote sensing of the Earth: A personal view. *Remote Sensing of Environment*, *113*(1), S5–S16. https://doi.org/10.1016/j.rse.2007.12.014

Goodin, D. G., & Henebry, G. M. (2002). The effect of rescaling on fine spatial resolution NDVI data: A test using multi-resolution aircraft sensor data. *International Journal of Remote Sensing*, *23*(18), 3865–3871. https://doi.org/10.1080/01431160210122303

Gordon, H. R., & Wang, M. (1994). Retrieval of water-leaving radiance and aerosol optical thickness over the oceans with SeaWiFS: a preliminary algorithm. *Applied Optics*, *33*(3), 443–452. https://doi.org/10.1364/AO.33.000443

Gorroño, J., Banks, A. C., Fox, N. P., & Underwood, C. (2017). Radiometric inter-sensor cross-calibration uncertainty using a traceable high accuracy reference hyperspectral imager. *ISPRS Journal of Photogrammetry and Remote Sensing*. https://doi.org/10.1016/j.isprsjprs.2017.07.002

Goyal, A., & Guruprasad, R. B. (2018). A novel blending algorithm for satellite-derived high resolution spatio-temporal normalized difference vegetation index. In *SPIE 10783: Remote Sensing for Agriculture, Ecosystems, and Hydrology XX, 1078307*. Berlin, Germany: SPIE. https://doi.org/10.1117/12.2325308

Grings, F. M., Ferrazzoli, P., Jacobo-Berlles, J. C., Karszenbaum, H., Tiffenberg, J., Pratolongo, P., & Kandus, P. (2006). Monitoring flood condition in marshes using em models and envisat ASAR observations. *IEEE Transactions on Geoscience and Remote Sensing*, *44*(4), 936–942. https://doi.org/10.1109/TGRS.2005.863482

Gunderson, L. H. (2002). Ecological Resilience—In Theory and Application. *Annual Review of Ecology and Systematics*, *31*(1), 425–439. https://doi.org/10.1146/annurev.ecolsys.31.1.425

Guo, M., Li, J., Sheng, C., Xu, J., & Wu, L. (2017). A review of wetland remote sensing. *Sensors*, *17*(4), 777. https://doi.org/10.3390/s17040777

Han, X., Chen, X., & Feng, L. (2015). Four decades of winter wetland changes in Poyang Lake based on Landsat observations between 1973 and 2013. *Remote Sensing of Environment*, *156*(0), 426–437. https://doi.org/10.1016/j.rse.2014.10.003

Hardisky, M. A., Gross, M. F., & Klemas, V. (1986). Remote Sensing of Coastal Wetlands. *BioScience*, *36*(7), 453–460. https://doi.org/10.2307/1310341

Hassan, N., Hamid, J. R. A., Adnan, N. A., & Jaafar, M. (2014). Delineation of wetland areas from high resolution WorldView-2 data by object-based method. In *IOP Conference Series: Earth and Environmental Science, vol. 18, no. 1* (p. 012017). IOP Publishing Ltd. https://doi.org/10.1088/1755-1315/18/1/012017

Hatter, L. (2015). Apalachicola Bay Part 2: Climate Change And Collapse. Retrieved December 23, 2015, from http://news.wfsu.org/post/apalachicola-bay-part-2-climate-change-and-collapse

Hazaymeh, K., & Hassan, Q. K. (2015). Fusion of MODIS and Landsat-8 surface temperature images: A new approach. *PLoS ONE*, *10*(3), p.e0117755. https://doi.org/10.1371/journal.pone.0117755

Henry, J. B., Chastanet, P., Fellah, K., & Desnos, Y. L. (2006). Envisat multi-polarized ASAR data for flood mapping. *International Journal of Remote Sensing*, *27*(10), 1921–1929. https://doi.org/10.1080/01431160500486724

Hess, L. L., Melack, J. M., Melack, J. M., Filoso, S., Wang, Y., & Wang, Y. (1995). Delineation of Inundated Area and Vegetation Along the Amazon Floodplain with the SIR-C Synthetic Aperture Radar. *IEEE Transactions on Geoscience and Remote Sensing*, *33*(4), 896–904. https://doi.org/10.1109/36.406675

Hladik, C., & Alber, M. (2012). Accuracy assessment and correction of a LIDAR-derived salt marsh digital elevation model. *Remote Sensing of Environment*. https://doi.org/10.1016/j.rse.2012.01.018

Ho, L. T. K., Umitsu, M., & Yamaguchi, Y. (2010). Flood hazard mapping by satellite images and SRTM DEM in the Vu Gia-Thu Bon alluvial plain, Central Vietnam. *International Archives of the Photogrammetry, Remote Sensing and Spatial Information Science*, *38*(Part 8), 275–280. https://doi.org/10.1016/j.apgeog.2011.01.005

Van Hoek, M., Jia, L., Zhou, J., Zheng, C., & Menenti, M. (2016). Early drought detection by spectral analysis of satellite time series of precipitation and Normalized Difference Vegetation Index (NDVI). *Remote Sensing*, *8*(5), 422. https://doi.org/10.3390/rs8050422

126

Holden, G. J. (2005). Gauging the Fractal Dimension of Response Times fr. *Contemporary Nonlinear Methods for Behavioral Scientists: A Webbook Tutorial*, 268–318.

Holling C.S. (1973). Resilience and Stability Of Ecological Systems. *Annual Review of Ecology and Systematics,Systematics*, *4*(1), 1–23. https://doi.org/10.1146/annurev.es.04.110173.000245

Honkavaara, E., Saari, H., Kaivosoja, J., Pölönen, I., Hakala, T., Litkey, P., et al. (2013). Processing and assessment of spectrometric, stereoscopic imagery collected using a lightweight UAV spectral camera for precision agriculture. *Remote Sensing*, *5*(10), 5006–5039. https://doi.org/10.3390/rs5105006

Hooshyar, M., Kim, S., Wang, D., & Medeiros, S. C. (2015). Wet channel network extraction by integrating LiDAR intensity and elevation data. *Water Resources Research*, *51*(12), 10029–10046. https://doi.org/10.1002/2015WR018021

Hooshyar, M., Singh, A., & Wang, D. (2017). Hydrologic controls on junction angle of river networks. *Water Resources Research*. https://doi.org/10.1002/2016WR020267

Horritt, M. S., Mason, D. C., & Luckman, A. J. (2001). Flood boundary delineation from synthetic aperture radar imagery using a statistical active contour model. *International Journal of Remote Sensing*, *22*(13), 2489–2507. https://doi.org/10.1080/01431160116902

Huang, C., Peng, Y., Lang, M., Yeo, I.-Y. Y., & McCarty, G. (2014). Wetland inundation mapping and change monitoring using Landsat and airborne LiDAR data. *Remote Sensing of Environment*, *141*, 231–242. https://doi.org/10.1016/j.rse.2013.10.020

Huang, Y., Sun, W., Zhang, W., Yu, Y., Su, Y., & Songw, C. (2010). Marshland conversion to cropland in northeast China from 1950 to 2000 reduced the greenhouse effect. *Global Change Biology*, *16*(2), 680–695. https://doi.org/10.1111/j.1365-2486.2009.01976.x

Huck, A. (2016). Sentinel-3 data benefit users. Retrieved April 3, 2018, from https://sentinel.esa.int/web/sentinel/missions/sentinel-3/news/-/article/sentinel-3-data-benefit-users

Huete, A. R. (1988). A soil-adjusted vegetation index (SAVI). *Remote Sensing of Environment*, *25*(3), 295–309. https://doi.org/10.1016/0034-4257(88)90106-X

Hurricane Research Division. (2012). Chronological List of All Hurricanes which Affected the Continental United States: 1851-2012. Retrieved October 23, 2018, from https://web.archive.org/web/20140210221648/http://www.aoml.noaa.gov/hrd/hurdat/All_U.S._Hurricanes.html

Imhoff, M. L., Vermillon, C., Story, M. H., Choudhury, M. A., & Gafoor, A. (1987). Monsoon flood boundary delineation and damage assessment using space borne imaging radar and Landsat data. *Photogrammetric Engineering and Remote Sensing*, *53*, 405–413.

Irons, J. R. (2018). Landsat Science. Retrieved April 2, 2018, from https://landsat.gsfc.nasa.gov/landsat-9/landsat-9-spectral-bands/

Jagalingam, P., & Hegde, A. V. (2015). A Review of Quality Metrics for Fused Image. *Aquatic Procedia*. https://doi.org/10.1016/j.aqpro.2015.02.019

Jain, S. K., Singh, R. D., Jain, M. K., & Lohani, A. K. (2005). Delineation of flood-prone areas using remote sensing techniques. *Water Resources Management*, *19*(4), 333–347. https://doi.org/10.1007/s11269-005-3281-5

Jain, S. K., Saraf, A. K., Goswami, A., & Ahmad, T. (2006). Flood inundation mapping using NOAA AVHRR data. *Water Resources Management*, *20*(6), 949–959. https://doi.org/10.1007/s11269-006-9016-4

Jarihani, A. A., McVicar, T. R., van Niel, T. G., Emelyanova, I. V., Callow, J. N., & Johansen, K. (2014). Blending landsat and MODIS data to generate multispectral indices: A comparison of "index-then-blend" and "Blend-Then-Index" approaches. *Remote Sensing*, *6*(10), 9213–9238. https://doi.org/10.3390/rs6109213

Ji, L., & Peters, A. J. (2003). Assessing vegetation response to drought in the northern Great Plains using vegetation and drought indices. *Remote Sensing of Environment*, *87*(1), 85–98. https://doi.org/10.1016/S0034-4257(03)00174-3

Jiang, S., & Friedland, C. J. (2016). Automatic urban debris zone extraction from post-hurricane very high-resolution satellite and aerial imagery. *Geomatics, Natural Hazards and Risk*, *7*(3), 933–952. https://doi.org/10.1080/19475705.2014.1003417

Jiang, W., He, G., Long, T., Ni, Y., Liu, H., Peng, Y., et al. (2018). Multilayer perceptron neural network for surface water extraction in landsat 8 OLI satellite images. *Remote Sensing*. https://doi.org/10.3390/rs10050755

Jiang, Z., Huete, A. R., Chen, J., Chen, Y., Li, J., Yan, G., & Zhang, X. (2006). Analysis of NDVI and scaled difference vegetation index retrievals of vegetation fraction. *Remote Sensing of Environment*, *101*(3), 366–378. https://doi.org/10.1016/j.rse.2006.01.003

Jiao, W., Zhang, L., Chang, Q., Fu, D., Cen, Y., & Tong, Q. (2016). Evaluating an enhanced vegetation condition index (VCI) based on VIUPD for drought monitoring in the continental United States. *Remote Sensing*, *8*(3), 224. https://doi.org/10.3390/rs8030224

Jollineau, M., & Howarth, P. (2002). Use of high-resolution imagery to map wetland environments in south-central Ontario, Canada. In *IEEE International Geoscience and Remote Sensing Symposium* (pp. 3089–3091). IEEE. https://doi.org/10.1109/IGARSS.2002.1026878

Jung, H. C. (2011). *Wetland hydrodynamics using interferometric synthetic aperture radar, remote sensing, and modeling*.

Justice, C. O., Vermote, E. F., Townshend, J. R. G., Defries, R. S., Roy, D. P., Hall, D. K., et al.

(1998). The Moderate Resolution Imaging Spectroradiometer (MODIS): land remote sensing for global change research. *Geoscience and Remote Sensing, IEEE Transactions On*, *36*(4), 1228–1249. https://doi.org/10.1109/36.701075

Karnieli, A., Agam, N., Pinker, R. T., Anderson, M., Imhoff, M. L., Gutman, G. G., et al. (2010). Use of NDVI and land surface temperature for drought assessment: Merits and limitations. *Journal of Climate*, *23*(3), 618–633. https://doi.org/10.1175/2009JCLI2900.1

Kayastha, N., Thomas, V., Galbraith, J., & Banskota, A. (2012). Monitoring wetland change using inter-annual landsat time-series data. *Wetlands*, *32*(6), 1149–1162. https://doi.org/10.1007/s13157-012-0345-1

Kentula, M. E. (2015). Wetland Restoration and Creation. *National Water Summary on Wetland Resources, United States Geological Survey Water Supply Paper 2425*, *2425*, 87–92.

Khanna, S., Santos, M. J., Koltunov, A., Shapiro, K. D., Lay, M., & Ustin, S. L. (2017). Marsh loss due to cumulative impacts of hurricane isaac and the DeepWater Horizon oil spill in Louisiana. *Remote Sensing*, *9*(2), 169. https://doi.org/10.3390/rs9020169

Kiage, L. M., Walker, N. D., Balasubramanian, S., Babin, A., & Barras, J. (2005). Applications of Radarsat-1 synthetic aperture radar imagery to assess hurricane-related flooding of coastal Louisiana. *International Journal of Remote Sensing*, *26*(24), 5359–5380. https://doi.org/10.1080/01431160500442438

Kim, S., McGaughey, R. J., Andersen, H.-E., & Schreuder, G. (2009). Tree species differentiation using intensity data derived from leaf-on and leaf-off airborne laser scanner data. *Remote Sensing of Environment*, *113*(8), 1575–1586. https://doi.org/10.1016/j.rse.2009.03.017

Kirilenko, A. P., & Sedjo, R. A. (2007). Climate change impacts on forestry. *Proceedings of the National Academy of Sciences of the United States of America (PNAS)*, *104*(50), 19697–19702. https://doi.org/https://doi.org/10.1073/pnas.0701424104

Klemas, V. (2013a). Remote sensing of emergent and submerged wetlands: an overview. *International Journal of Remote Sensing*, *34*(18), 6286–6320. https://doi.org/10.1080/01431161.2013.800656

Klemas, V. (2013b). Using Remote Sensing to Select and Monitor Wetland Restoration Sites: An Overview. *Journal of Coastal Research*, *29*(4), 958–970. https://doi.org/10.2112/JCOASTRES-D-12-00170.1

Klemas, V., Dobson, J., Ferguson, R., & Haddad, K. (1993). A coastal land cover classification system for the NOAA Coastwatch Change Analysis Project. *Journal of Coastal …*, 862–872.

Kogan, F. N. (1995). Droughts of the Late 1980s in the United States as Derived from NOAA Polar-Orbiting Satellite Data. *Bulletin of the American Meteorological Society*, *76*(5), 655–668. https://doi.org/10.1175/1520-0477(1995)076<0655:DOTLIT>2.0.CO;2

Konisky, D. M., Hughes, L., & Kaylor, C. H. (2016). Extreme weather events and climate change concern. *Climatic Change*, *134*(4), 533–547. https://doi.org/10.1007/s10584-015-1555-3

Krehbiel, C. (2017). Working with ASTER L1T Visible and Near Infrared (VNIR) Data in R.

Kulawardhana, R. W., Thenkabail, P. S., Vithanage, J., Biradar, C., Islam Md. A., Gunasinghe, S., & Alankara, R. (2007). Evaluation of the Wetland Mapping Methods using Landsat ETM+ and SRTM Data. *Journal of Spatial Hydrology*. https://doi.org/10.1017/CBO9780511806049

Kumar, L., & Sinha, P. (2014). Mapping salt-marsh land-cover vegetation using high-spatial and hyperspectral satellite data to assist wetland inventory. *GIScience and Remote Sensing*, *51*(5), 483–497. https://doi.org/10.1080/15481603.2014.947838

Landmann, T., Schramm, M., Huettich, C., & Dech, S. (2013). MODIS-based change vector analysis for assessing wetland dynamics in Southern Africa. *Remote Sensing Letters*, *4*(2), 104–113. https://doi.org/10.1080/2150704X.2012.699201

Langley, J. A., & Megonigal, J. P. (2010). Ecosystem response to elevated CO_2 levels limited by nitrogen-induced plant species shift. *Nature*, *466*(7302), 96. https://doi.org/10.1038/nature09176

Leitman, S., Pine, W. E., & Kiker, G. (2016). Management Options During the 2011–2012 Drought on the Apalachicola River: A Systems Dynamic Model Evaluation. *Environmental Management*, *58*(2), 193–207. https://doi.org/10.1007/s00267-016-0712-4

Lenhardt, C. (2015). Delivering NASA Earth Observing System (EOS) Data with Digital Content Repository Technology. Retrieved January 14, 2019, from https://processing.eos.com/

Levy, R. (2000). Normalized Difference Vegetation Index. Retrieved March 4, 2019, from https://earthobservatory.nasa.gov/features/MeasuringVegetation/measuring_vegetation_2.php

Li, S., Ganguly, S., Dungan, J. L., Wang, W., & Nemani, R. R. (2017). Sentinel-2 MSI Radiometric Characterization and Cross-Calibration with Landsat-8 OLI. *Advances in Remote Sensing*, *6*(2), 147. https://doi.org/10.4236/ars.2017.62011

Li, W., Du, Z., Ling, F., Zhou, D., Wang, H., Gui, Y., et al. (2013). A comparison of land surface water mapping using the normalized difference water index from TM, ETM+ and ALI. *Remote Sensing*, *5*(11), 5530–5549. https://doi.org/10.3390/rs5115530

Liu, Y., Chen, X., Wang, Z., Wang, Z. J., Ward, R. K., & Wang, X. (2018). Deep learning for pixel-level image fusion: Recent advances and future prospects. *Information Fusion*, *42*, 158–173. https://doi.org/10.1016/j.inffus.2017.10.007

Lizárraga-Celaya, C., Watts, C. J., Rodríguez, J. C., Garatuza-Payán, J., Scott, R. L., & Sáiz-Hernández, J. (2010). Spatio-temporal variations in surface characteristics over the North American Monsoon region. *Journal of Arid Environments*, *74*(5), 540–548.

https://doi.org/10.1016/j.jaridenv.2009.09.027

Lo, O., Buchanan, W. J., Griffiths, P., & Macfarlane, R. (2018). Distance Measurement Methods for Improved Insider Threat Detection. *Security and Communication Networks*. https://doi.org/10.1155/2018/5906368

Lynnes, C. (2007). A Simple, Scalable, Script-Based Science Processor. In *Earth Science Satellite Remote Sensing*. https://doi.org/10.1007/978-3-540-37294-3_8

Maignan, F., Bréon, F. M., Bacour, C., Demarty, J., & Poirson, A. (2008). Interannual vegetation phenology estimates from global AVHRR measurements. Comparison with in situ data and applications. *Remote Sensing of Environment*, *112*(2), 496–505. https://doi.org/10.1016/j.rse.2007.05.011

Major, D. J., Baret, F., & Guyot, G. (1990). A ratio vegetation index adjusted for soil brightness. *International Journal of Remote Sensing*, *11*(5), 727–740. https://doi.org/10.1080/01431169008955053

Maktav, D. (Ed. . (2009). *Remote sensing for a changing Europe. Proceedings of the 28th Symposium of the European Association of Remote Sensing Laboratories, Istanbul, Turkey, 2-5 June 2008*. IOS press.

Malamud, B. D., & Turcotte, D. L. (1999). Self-Affine Time Series: I. Generation and Analyses. *Advances in Geophysics*, *40*, 1–90. https://doi.org/10.1016/S0065-2687(08)60293-9

Mandanici, E., & Bitelli, G. (2016). Preliminary comparison of sentinel-2 and landsat 8 imagery for a combined use. *Remote Sensing*, *8*(12), 1014. https://doi.org/10.3390/rs8121014

Mandelbrot, B. B. (1984). The Fractal Geometry of Nature. *The American Mathematical Monthly*, *91*(9), 594–598. https://doi.org/10.2307/2323761

Mandelbrot, B. B., & Ness, V. (1968). Fractional Brownian motions, fractional noises and applications. *SIAM Review*, *10*(4), 422–437.

Marechal, C., Pottier, E., Hubert-Moy, L., & Rapinel, S. (2012). One year wetland survey investigations from quad-pol RADARSAT-2 time-series SAR images. *Canadian Journal of Remote Sensing*, *38*(3), 240–252. https://doi.org/10.5589/m12-017

Martinuzzi, S., Gould, W. W. A., Ramos González, O. M., & González, O. (2007). Creating cloud-free Landsat ETM+ data sets in tropical landscapes: cloud and cloud-shadow removal. *General Technical Report IITF-GTR-32*. https://doi.org/97208-3890

Matsushita, B., Yang, W., Chen, J., Onda, Y., & Qiu, G. (2007). Sensitivity of the Enhanced Vegetation Index (EVI) and Normalized Difference Vegetation Index (NDVI) to topographic effects: A case study in high-density cypress forest. *Sensors*, *7*(11), 2636–2651. https://doi.org/10.3390/s7112636

Medeiros, S.C., Hagen, S.C., Chaouch, N., Feyen, J., Temimi, M., Weishampel, J., et al. (2013). Assessing the Performance of a Northern Gulf of Mexico Tidal Model Using Satellite Imagery. *Remote Sensing*, *5*(11), 5662–5679. https://doi.org/10.3390/rs5115662

Medeiros, S., Hagen, S., Weishampel, J., & Angelo, J. (2015). Adjusting lidar-derived digital terrain models in coastal marshes based on estimated aboveground biomass density. *Remote Sensing*, *7*(4), 3507–3525. https://doi.org/10.3390/rs70403507

Medeiros, S. C., & Hagen, S. C. (2013). Review of wetting and drying algorithms for numerical tidal flow models. *International Journal for Numerical Methods in Fluids*, *71*(4), 473–487. https://doi.org/10.1002/fld.3668

Mezned, N., Abdeljaoued, S., & Boussema, M. R. (2007). Unmixing based landsat ETM+ and ASTER image fusion for hybrid multispectral image analysis. In *International Geoscience and Remote Sensing Symposium (IGARSS)* (pp. 3074–3077). https://doi.org/10.1109/IGARSS.2007.4423494

Michener, W. K., Blood, E. R., Bildstein, K. L., Brinson, M. M., & Gardner, L. R. (1997). Climate change, hurricanes and tropical storms, and rising sea level in coastal wetlands. *Ecological Applications*, *7*(3), 770–801. https://doi.org/10.1890/1051-0761(1997)007[0770:CCHATS]2.0.CO;2

Michishita, R., Gong, P., & Xu, B. (2012). Spectral mixture analysis for bi-sensor wetland mapping using Landsat TM and Terra MODIS data. *International Journal of Remote Sensing*, *33*(11), 3373–3401. https://doi.org/10.1080/01431161.2011.611185

Miramontes, O., & Rohani, P. (2002). Estimating 1/fαscaling exponents from short time-series. *Physica D: Nonlinear Phenomena*, *166*(3–4), 147–154. https://doi.org/10.1016/S0167-2789(02)00429-3

Mo, Y., Kearney, M., & Momen, B. (2017). Drought-associated phenological changes of coastal marshes in Louisiana. *Ecosphere*, *8*(5). https://doi.org/https://doi.org/10.1002/ecs2.1811

Mo, Y., Kearney, M. S., Riter, J. C. A., Zhao, F., & Tilley, D. R. (2018). Assessing biomass of diverse coastal marsh ecosystems using statistical and machine learning models. *International Journal of Applied Earth Observation and Geoinformation*, *68*, 189–201. https://doi.org/https://doi.org/10.1016/j.jag.2017.12.003

Moeslund, J. E., Arge, L., Bøcher, P. K., Nygaard, B., & Svenning, J. C. (2011). Geographically comprehensive assessment of salt-meadow vegetation-elevation relations using LiDAR. *Wetlands*, *31*(3), 471. https://doi.org/10.1007/s13157-011-0179-2

Moomaw, W. R., Chmura, G. L., Davies, G. T., Finlayson, C. M., Middleton, B. A., Natali, S. M., et al. (2018). Wetlands In a Changing Climate: Science, Policy and Management. *Wetlands*. https://doi.org/10.1007/s13157-018-1023-8

Moore, J., Goffin, P., Meyer, M., Lundrigan, P., Patwari, N., Sward, K., & Wiese, J. (2018).

Managing In-home Environments through Sensing, Annotating, and Visualizing Air Quality Data. *Proceedings of the ACM on Interactive, Mobile, Wearable and Ubiquitous Technologies*, *2*(3), 128. https://doi.org/10.1145/3264938

Morgan, J. L., Gergel, S. E., & Coops, N. C. (2010). Aerial Photography: A Rapidly Evolving Tool for Ecological Management. *BioScience*, *60*(1), 47–59. https://doi.org/10.1525/bio.2010.60.1.9

Morris, J. T., Sundareshwar, P. V., Nietch, C. T., Kjerfve, B., & Cahoon, D. R. (2002). Responses of coastal wetlands to rising sea level. *Ecology*, *83*(10), 2869–2877. https://doi.org/10.1890/0012-9658(2002)083[2869:ROCWTR]2.0.CO;2

Mueller-Wilm, U., Devignot, O., & Pessiot, L. (2016). S2 MPC Sen2Cor configuration and user manual. https://doi.org/S2-PDGS-MPC-L2A-SUM-V2.3

Mueller, N., Lewis, A., Roberts, D., Ring, S., Melrose, R., Sixsmith, J., et al. (2016). Water observations from space: Mapping surface water from 25years of Landsat imagery across Australia. *Remote Sensing of Environment*, *174*, 341–352. https://doi.org/10.1016/j.rse.2015.11.003

Müllerová, J., Brůna, J., Bartaloš, T., Dvořák, P., Vítková, M., & Pyšek, P. (2017). Timing Is Important: Unmanned Aircraft vs. Satellite Imagery in Plant Invasion Monitoring. *Frontiers in Plant Science*, *8*, 887. https://doi.org/10.3389/fpls.2017.00887

Muro, J., Canty, M., Conradsen, K., Hüttich, C., Nielsen, A. A., Skriver, H., et al. (2016). Short-term change detection in wetlands using Sentinel-1 time series. *Remote Sensing*, *8*(10), 795. https://doi.org/10.3390/rs8100795

Myneni, R. B., Keeling, C. D., Tucker, C. J., Asrar, G., & Nemani, R. R. (1997). Increased plant growth in the northern high latitudes from 1981 to 1991. *Nature*, *386*(6626), 698–702. https://doi.org/10.1038/386698a0

Nay, J., Burchfield, E., & Gilligan, J. (2018). A machine-learning approach to forecasting remotely sensed vegetation health. *International Journal of Remote Sensing*. https://doi.org/10.1080/01431161.2017.1410296

Nghiem, S. V., Brakenridge, G. R., & Nguyen, D. T. (2017). Hurricanes Harvey and Irma - High-Resolution Flood Mapping and Monitoring from Sentinel SAR with the Depolarization Reduction Algorithm for Global Observations of InundatioN (DRAGON). American Geophysical Union. https://doi.org/2017AGUFMNH23E2873N

Nicholls, R. J., & Cazenave, A. (2010). Sea-level rise and its impact on coastal zones. *Science*, *328*(5985), 1517–1520. https://doi.org/10.1126/science.1185782

NOAA. (2017). *C-CAP Regional Land Cover Classification Scheme*.

Notaro, M., Liu, Z., Gallimore, R. G., Williams, J. W., Gutzler, D. S., & Collins, S. (2010).

Complex seasonal cycle of ecohydrology in the Southwest United States. *Journal of Geophysical Research: Biogeosciences*, *115*(G4). https://doi.org/10.1029/2010JG001382

Nünez, J., Otazu, X., Fors, O., Prades, A., Palà, V., & Arbiol, R. (1999). Multiresolution-based image fusion with additive wavelet decomposition. *IEEE Transactions on Geoscience and Remote Sensing*, *37*(3), 1204–1211. https://doi.org/10.1109/36.763274

Orville, H. D. (1990). AMS statement on meteorological drought. *Bulletin of the American Meteorological Society*, *71*(7), 1021–1023.

Ozesmi, S. L., Bauer, M. E., Tiner, R. W., Lang, M. W., & Klemas, V. V. (2002). Satellite remote sensing of wetlands. *Wetlands Ecology and Management*, *10*(5), 381–402. https://doi.org/10.1023/A:1020908432489

Palmer, D. S., O'Boyle, N. M., Glen, R. C., & Mitchell, J. B. O. (2007). Random forest models to predict aqueous solubility. *Journal of Chemical Information and Modeling*, *47*(1), 150–8. https://doi.org/10.1021/ci060164k

Papa, F., Prigent, C., Durand, F., & Rossow, W. B. (2006). Wetland dynamics using a suite of satellite observations: A case study of application and evaluation for the Indian Subcontinent. *Geophysical Research Letters*, *33*(8). https://doi.org/10.1029/2006GL025767

Park, S. K., & Schowengerdt, R. A. (1983). Image reconstruction by parametric cubic convolution. *Computer Vision, Graphics and Image Processing*. https://doi.org/10.1016/0734-189X(83)90026-9

Passeri, D. L., Hagen, S. C., Plant, N. G., Bilskie, M. V., Medeiros, S. C., & Alizad, K. (2016). Tidal hydrodynamics under future sea level rise and coastal morphology in the Northern Gulf of Mexico. *Earth's Future*, *4*(5), 159–176. https://doi.org/10.1002/2015EF000332

Pedregosa, F., & Varoquaux, G. (2011). Scikit-learn: Machine learning in Python. *Journal of Machine Learning Research*, *12*, 2825–2830. Retrieved from http://dl.acm.org/citation.cfm?id=2078195

Perkins, P., & Heber, S. (2018). Identification of Ribosome Pause Sites Using a Z-Score Based Peak Detection Algorithm. In *IEEE 8th International Conference on Computational Advances in Bio and Medical Sciences (ICCABS)* (pp. 1–6). https://doi.org/978-1-5386-8520-4

Pilgram, B., & Kaplan, D. T. (1998). A comparison of estimators for 1/f noise. *Physica D: Nonlinear Phenomena*, *114*(1–2), 108–122. https://doi.org/10.1016/S0167-2789(97)00188-7

Pohl, C., & Van Genderen, J. L. (1998). Review article Multisensor image fusion in remote sensing: Concepts, methods and applications. *International Journal of Remote Sensing*, *19*(5), 823–854. https://doi.org/10.1080/014311698215748

Porter, D. E., Field, D. W., Klemas, V. V., Jensen, J. R., Malhotra, A., Field, R. T., & Walker, S.

P. (2006). *RESAAP Final Report: NOAA/ NERRS Remote Sensing Applications Assessment Project*. Columbia, South Carolina: University of South Carolina.

Quiring, S. M. (2009). Monitoring drought: An evaluation of meteorological drought indices. *Geography Compass*, *3*(1), 64–88. https://doi.org/10.1111/j.1749-8198.2008.00207.x

Quiring, S. M., & Ganesh, S. (2010). Evaluating the utility of the Vegetation Condition Index (VCI) for monitoring meteorological drought in Texas. *Agricultural and Forest Meteorology*, *150*(3), 330–339. https://doi.org/10.1016/j.agrformet.2009.11.015

Ramsey, I., Spruce, J., Rangoonwala, A., Suzuoki, Y., Smoot, J., Gasser, J., & Bannister, T. (2011). Daily MODIS data trends of hurricane-induced forest impact and early recovery. *Photogrammetric Engineering and Remote Sensing*, *17*(11), 1113–1143. https://doi.org/0099-1112/11/7711–1133/$3.00/0

Ramsey III, E. W., Chappell, D. K., & Baldwin, D. G. (1997). AVHRR lmagery Used to Identify Hurricane Damage in a Forested Wetland of Louisiana. *Photogrammetric Engineering & Remote Sensing*, *63*(3), 293–297. Retrieved from http://www.asprs.org/a/publications/pers/97journal/march/1997_mar_293-297.pdf

Ramsey III, E. W., Nelson, G. A., & Sapkota, S. K. (2001). Coastal change analysis program implemented in Louisiana. *Journal of Coastal Research*, *17*, 53–71.

Ranchin, T., & Wald, L. (1996). Fusion of earth data: Merging point measurements, raster maps, and remotely sensed images. In *Proc. Int. Conf.*. Cannes, France.

Reeder, S. L., & Rankey, E. C. (2009). *A Tale of Two Storms: An Integrated Field, Remote Sensing, and Modeling Study Examining the Impact Of Hurricanes Frances And Jeanne On Carbonate Systems, Bahamas*. (Peter K. Swart, Gregor P. Eberli, Judith A. McKenzie, Ian Jarvis, & Tom Stevens, Eds.), *Perspectives in Carbonate Geology: A Tribute to the Career of Robert Nathan Ginsburg,*. https://doi.org/https://doi.org/10.1002/9781444312065.ch6

Robinove, C. J. (1978). Interpretation of a Landsat image of an unusual flood phenomenon in Australia. *Remote Sensing of Environment*, *7*(3), 219–225. https://doi.org/10.1016/0034-4257(78)90033-0

Roderick, M., Smith, R., & Cridland, S. (1996). The precision of the NDVI derived from AVHRR observations. *Remote Sensing of Environment*, *56*(1), 57–65. https://doi.org/10.1016/0034-4257(95)00213-8

Rodgers, J. C., Murrah, A. W., & Cooke, W. H. (2009). The impact of hurricane katrina on the coastal vegetation of the weeks bay reserve, alabama from NDVI data. *Estuaries and Coasts*, *32*(3), 496–507. https://doi.org/10.1007/s12237-009-9138-z

Rodriguez-Galiano, V. F., Dash, J., & Atkinson, P. M. (2015). Intercomparison of satellite sensor land surface phenology and ground phenology in Europe. *Geophysical Research Letters*, *42*(7), 2253–2260. https://doi.org/10.1002/2015GL063586

Rogan, J., Schneider, L., Christman, Z., Millones, M., Lawrence, D., & Schmook, B. (2011). Hurricane disturbance mapping using MODIS EVI data in the southeastern Yucatán, Mexico. *Remote Sensing Letters*, *2*(3), 259–267. https://doi.org/10.1080/01431161.2010.520344

Roy, D. P., Ju, J., Lewis, P., Schaaf, C., Gao, F., Hansen, M., & Lindquist, E. (2008). Multi-temporal MODIS-Landsat data fusion for relative radiometric normalization, gap filling, and prediction of Landsat data. *Remote Sensing of Environment*, *112*(6), 3112–3130. https://doi.org/10.1016/j.rse.2008.03.009

Rykhus, R., & Lu, Z. (2005). *Hurricane Katrina flooding and oil slicks mapped with satellite imagery*. *Science and the Storms: The USGS Response to the Hurricanes of 2005*.

Sandhu, D., Singh, A., Fan, N., Wang, D., & Duranceau, S. J. (2016). Hydro-geomorphic response of Everglades to changing climate and anthropogenic activities. *Journal of Hydrology*, *543*(2016), 861–872. https://doi.org/10.1016/j.jhydrol.2016.11.004

Scavia, D., Field, J. C., Boesch, D. F., Buddenmeier, R. W., Burkett, V., Cayan, D. R., et al. (2002). Climate Change Impacts on U.S. Coastal and Marine Ecosystems. *Estuaries*, *25*(2), 149–164. https://doi.org/10.1007/BF02691304

Schubel, J. R., & Hirschberg, D. J. (1978). Estuarine Graveyards, Climatic Change, and the Importance of the Estuarine Environment. *Estuarine Interactions* , 285–303.

Seiler, R. A., Kogan, F., & Wei, G. (2000). Monitoring weather impact and crop yield from NOAA AVHRR data in Argentina. *Advances in Space Research*, *26*(7), 1177–1185. https://doi.org/10.1016/S0273-1177(99)01144-8

Seker, D. Z., Direk, S., Musaoglu, N., & Gazioglu, C. (2013). Determination of Effects of Coastal Deformation Caused by Waves and Storms at Black Sea Coast of Turkey utilizing InSAR Technique. In American Geophysical Union (Ed.). https://doi.org/2013AGUFMNH51C1629S

Seo, D. K., Kim, Y. H., Eo, Y. D., Lee, M. H., & Park, W. Y. (2018). Fusion of SAR and Multispectral Images Using Random Forest Regression for Change Detection. *ISPRS International Journal of Geo-Information*, *7*(10), 401. https://doi.org/10.3390/ijgi7100401

Sesnie, S. E., Dickson, B. G., Rosenstock, S. S., & Rundall, J. M. (2012). A comparison of landsat TM and MODIS vegetation indices for estimating forage phenology in desert bighorn sheep (ovis canadensis nelsoni) habitat in the Sonoran desert, USA. *International Journal of Remote Sensing*, *33*(1), 276–286. https://doi.org/10.1080/01431161.2011.592865

Shettigara, V. K. (1992). A generalized component substitution technique for spatial enhancement of multispectral images using a higher resolution data set. *Photogrammetric Engineering & Remote Sensing*, *58*, 561–567. https://doi.org/10.1038/050073a0

Singh, A., Porté-Agel, F., & Foufoula-georgiou, E. (2010). On the influence of gravel bed dynamics on velocity power spectra. *Water Resources Research*, *46*(4).

https://doi.org/10.1029/2009WR008190

Singh, A., Guala, M., Lanzoni, S., & Foufoula-Georgiou, E. (2012). Bedform effect on the reorganization of surface and subsurface grain size distribution in gravel bedded channels. *Acta Geophysica*, *60*(6), 1607–1638. https://doi.org/10.2478/s11600-012-0075-z

Singh, A., Reinhardt, L., & Foufoula-Georgiou, E. (2015). Landscape reorganization under changing climatic forcing: Results from an experimental landscape. *Water Resources Research*. https://doi.org/10.1002/2015WR017161

Sivaperuman, C., & Venkatraman, C. (2015). *Marine Faunal Diversity in India*. Academic Press. https://doi.org/https://doi.org/10.1016/B978-0-12-801948-1.00017-3

Sruthi, S., & Aslam, M. A. M. (2015). Agricultural Drought Analysis Using the NDVI and Land Surface Temperature Data; a Case Study of Raichur District. *Aquatic Procedia*, *4*, 1258–1264. https://doi.org/10.1016/j.aqpro.2015.02.164

Steyer, G. D., Couvillion, B. R., & Barras, J. A. (2013). Monitoring Vegetation Response to Episodic Disturbance Events by using Multitemporal Vegetation Indices. *Journal of Coastal Research*, *63*(sp1), 118–130. https://doi.org/10.2112/SI63-011.1

Stoica, P., & Randolph, L. M. (1997). *Introduction to spectral analysis* (Vol 1). Upper Saddle River, NJ: Prentice hall.

SUN, C. (2015). Salt marsh mapping based on a short-time interval NDVI time-series from HJ-1 CCD imagery. In *AGU*. American Geophysical Union. https://doi.org/abstract id. H53G-1751

Swanson, K. M., Drexler, J. Z., Schoellhamer, D. H., Thorne, K. M., Casazza, M. L., Overton, C. T., et al. (2014). Wetland Accretion Rate Model of Ecosystem Resilience (WARMER) and Its Application to Habitat Sustainability for Endangered Species in the San Francisco Estuary. *Estuaries and Coasts*, *37*(2), 476–492. https://doi.org/10.1007/s12237-013-9694-0

Switzer, T. S., Winner, B. L., Dunham, N. M., Whittington, J. a, & Thomas, M. (2006). Influence of sequential hurricanes on nekton communities in a southeast Florida estuary: short-term effects in the context of historical variations in freshwater inflow. *Estuaries and Coasts*, *29*(6A), 1011–1018.

Szantoi, Z., Malone, S., Escobedo, F., Misas, O., Smith, S., & Dewitt, B. (2012). A tool for rapid post-hurricane urban tree debris estimates using high resolution aerial imagery. *International Journal of Applied Earth Observation and Geoinformation*, *18*, 548–556. https://doi.org/10.1016/j.jag.2011.10.009

Tadesse, T., Demisse, G. B., Zaitchik, B., & Dinku, T. (2014). Satellite-based hybrid drought monitoring tool for prediction of vegetation condition in Eastern Africa: A case study for Ethiopia. *Water Resources Research*, *50*(3), 2176–2190. https://doi.org/10.1002/2013WR014281

Tahsin, S., Medeiros, S. C., & Singh, A. (2016). Resilience of coastal wetlands to extreme hydrologic events in Apalachicola Bay. *Geophysical Research Letters*, *43*(14), 7529–7537. https://doi.org/10.1002/2016GL069594

Tahsin, S., Medeiros, S. C., Hooshyar, M., & Singh, A. (2017). Optical cloud pixel recovery via machine learning. *Remote Sensing*, *9*(6), 527. https://doi.org/10.3390/rs9060527

Tahsin, S., Medeiros, S. C., & Singh, A. (2018). Assessing coastal wetland resiliency to extreme events using remote sensing. *Remote Sensing*, *10*(9), 1390. https://doi.org/https://doi.org/10.3390/rs10091390

Taravat, A., Proud, S., Peronaci, S., Del Frate, F., & Oppelt, N. (2015). Multilayer perceptron neural networks model for meteosat second generation SEVIRI daytime cloud masking. *Remote Sensing*. https://doi.org/10.3390/rs70201529

Telesca, L., & Lasaponara, R. (2006). Quantifying intra-annual persistent behaviour in SPOT-VEGETATION NDVI data for Mediterranean ecosystems of southern Italy. *Remote Sensing of Environment*, *101*(1), 95–10. https://doi.org/10.1016/j.rse.2005.12.007

The NASA Land Processes Distributed Active Archive Center (LP DAAC). (n.d.). The ASTER L1T data product. Retrieved January 22, 2019, from https://lpdaa.usgs.gov/tools/data-pool/

Thomas, R. F., Kingsford, R. T., Lu, Y., Cox, S. J., Sims, N. C., & Hunter, S. J. (2015). Mapping inundation in the heterogeneous floodplain wetlands of the Macquarie Marshes, using Landsat Thematic Mapper. *Journal of Hydrology*, *524*, 194–213. https://doi.org/10.1016/j.jhydrol.2015.02.029

Tian, B., Zhou, Y.-X., Thom, R. M., Diefenderfer, H. L., & Yuan, Q. (2015). Detecting wetland changes in Shanghai, China using FORMOSAT and Landsat TM imagery. *Journal of Hydrology*, *529*(1), 1–10. https://doi.org/10.1016/j.jhydrol.2015.07.007

Tian, Y., Peters-Lidard, C. D., Eylander, J. B., Joyce, R. J., Huffman, G. J., Adler, R. F., et al. (2009). Component analysis of errors in Satellite-based precipitation estimates. *Journal of Geophysical Research Atmospheres*. https://doi.org/10.1029/2009JD011949

Topaloğlu, R. H., Sertel, E., & Musaoğlu, N. (2016). Assessment of classification accuracies of Sentinel-2 and Landsat-8 data for land cover/use mapping. In *International Archives of the Photogrammetry, Remote Sensing and Spatial Information Sciences - ISPRS Archives* (p. 41). https://doi.org/10.5194/isprsarchives-XLI-B8-1055-2016

Townsend, P. A. (2002). Relationships between forest structure and the detection of flood inundation in forested wetlands using C-band SAR. *International Journal of Remote Sensing*, *23*(3), 443–460. https://doi.org/10.1080/01431160010014738

Tu, T. M., Su, S. C., Shyu, H. C., & Huang, P. S. (2001). A new look at IHS-like image fusion methods. *Information Fusion*, *2*(3), 177–186. https://doi.org/10.1016/S1566-2535(01)00036-7

Vivoni, E. R., Moreno, H. A., Mascaro, G., Rodriguez, J. C., Watts, C. J., Garatuza-Payan, J., & Scott, R. L. (2008). Observed relation between evapotranspiration and soil moisture in the North American monsoon region. *Geophysical Research Letters*, *35*(22). https://doi.org/10.1029/2008GL036001

Waite, W. P., & Macdonald, H. C. (1971). "Vegetation Penetration" With K-Band Imaging Radars. *IEEE Transactions on Geoscience Electronics*, *9*(3), 147–155. https://doi.org/10.1109/TGE.1971.271487

Walker, J. J., De Beurs, K. M., Wynne, R. H., & Gao, F. (2012). Evaluation of Landsat and MODIS data fusion products for analysis of dryland forest phenology. *Remote Sensing of Environment*, *117*, 381–393. https://doi.org/10.1016/j.rse.2011.10.014

Wamsley, T. V., Cialone, M. A., Smith, J. M., Atkinson, J. H., & Rosati, J. D. (2010). The potential of wetlands in reducing storm surge. *Ocean Engineering*, *37*(1), 59–68. https://doi.org/10.1016/j.oceaneng.2009.07.018

Wang, F., & D'Sa, E. J. (2010). Potential of MODIS EVI in identifying hurricane disturbance to coastal vegetation in the Northern Gulf of Mexico. *Remote Sensing*, *2*(1), 1–18. https://doi.org/10.3390/rs2010001

Wang, Q., Shi, W., Atkinson, P. M., & Zhao, Y. (2015). Downscaling MODIS images with area-to-point regression kriging. *Remote Sensing of Environment*, *166*, 191–204. https://doi.org/10.1016/j.rse.2015.06.003

Wang, W., Qu, J. J., Hao, X., Liu, Y., & Stanturf, J. A. (2010). Post-hurricane forest damage assessment using satellite remote sensing. *Agricultural and Forest Meteorology*, *150*, 122–132. https://doi.org/10.1016/j.agrformet.2009.09.009

Wang, Y. (2012). *Detecting Vegetation Recovery Patterns After Hurricanes in South Florida Using NDVI Time Series*. University of Miami. Retrieved from http://scholarlyrepository.miami.edu/oa_theses

Webb, E. L., Friess, D. A., Krauss, K. W., Cahoon, D. R., Guntenspergen, G. R., & Phelps, J. (2013). A global standard for monitoring coastal wetland vulnerability to accelerated sea-level rise. *Nature Climate Change*, *3*(5), 458. https://doi.org/10.1038/nclimate1756

Wei, Q., Bioucas-Dias, J., Dobigeon, N., & Tourneret, J. Y. (2015). Hyperspectral and Multispectral Image Fusion Based on a Sparse Representation. *IEEE Transactions on Geoscience and Remote Sensing*, *53*(7), 3658–3668. https://doi.org/10.1109/TGRS.2014.2381272

Weier, J., & Herring, D. (2000). Measuring Vegetation: NDVI & EVI. Retrieved April 4, 2019, from https://earthobservatory.nasa.gov/features/MeasuringVegetation

White, E., & Kaplan, D. (2017). Restore or retreat? Saltwater intrusion and water management in coastal wetlands. *Ecosystem Health and Sustainability*, *3*(1).

https://doi.org/10.1002/ehs2.1258

Wilcox, D. A., & Whillans, T. H. (1999). Techniques for restoration of disturbed coastal wetlands of the Great Lakes. *Wetlands*, *19*(4), 835–857. https://doi.org/10.1007/BF03161787

Witt, A., & Malamud, B. D. (2013). Quantification of Long-Range Persistence in Geophysical Time Series: Conventional and Benchmark-Based Improvement Techniques. *Surveys in Geophysics*, *34*(5), 541–651. https://doi.org/10.1007/s10712-012-9217-8

Wong, C. P., Jiang, B., Bohn, T. J., Lee, K. N., Lettenmaier, D. P., Ma, D., & Ouyang, Z. (2017). Lake and wetland ecosystem services measuring water storage and local climate regulation. *Water Resources Research*, *53*(4), 3197–3223. https://doi.org/10.1002/2016WR019445

Wu, G., & Liu, Y. (2014). Satellite-based detection of water surface variation in China's largest freshwater lake in response to hydro-climatic drought. *International Journal of Remote Sensing*, *35*(11–12), 4544–58. https://doi.org/10.1080/01431161.2014.916444

Wu, W.-T., Zhou, Y.-X., & Tian, B. (2017). Coastal wetlands facing climate change and anthropogenic activities: A remote sensing analysis and modelling application. *Ocean and Coastal Management*, *138*, 1–10. https://doi.org/10.1016/j.ocecoaman.2017.01.005

Wulder, M. A., Hilker, T., White, J. C., Coops, N. C., Masek, J. G., Pflugmacher, D., & Crevier, Y. (2015). Virtual constellations for global terrestrial monitoring. *Remote Sensing of Environment*, *170*, 62–76. https://doi.org/10.1016/j.rse.2015.09.001

Xu, H.-Q., & Zhang, T.-J. (2011). Cross comparison of ASTER and landsat ETM+ multispectral measurements for NDVI and SAVI vegetation indices. *Guang Pu Xue Yu Guang Pu Fen Xi/Spectroscopy and Spectral Analysis*, *31*(7), 1902–1907. https://doi.org/10.3964/j.issn.1000-0593(2011)07-1902-06

Xue, J., & Su, B. (2017). Significant remote sensing vegetation indices: A review of developments and applications. *Journal of Sensors*, *2017*, 17 pages. https://doi.org/10.1155/2017/1353691

Yang, L., Homer, C., Hegge, K., Huang, C., Wylie, B., & Reed, B. (2001). A Landsat 7 scene selection strategy for a National Land Cover Database. *IEEE 2001 International Geoscience and Remote Sensing Symposium (Cat. No. 01CH37217)*, *3*, 1123–1125.

Yu, J., Zhan, C., Li, Y., Zhou, D., Fu, Y., Chu, X., et al. (2016). *Distribution of carbon, nitrogen and phosphorus in coastal wetland soil related land use in the Modern Yellow River Delta*. *Scientific Reports, 6*. https://doi.org/10.1038/srep37940

Zhang, C., Pan, X., Li, H., Gardiner, A., Sargent, I., Hare, J., & Atkinson, P. M. (2018). A hybrid MLP-CNN classifier for very fine resolution remotely sensed image classification. *ISPRS Journal of Photogrammetry and Remote Sensing*. https://doi.org/10.1016/j.isprsjprs.2017.07.014

Zhang, H., Chen, J. M., Huang, B., Song, H., & Li, Y. (2014). Reconstructing seasonal variation

of landsat vegetation index related to leaf area index by fusing with MODIS data. *IEEE Journal of Selected Topics in Applied Earth Observations and Remote Sensing*, *7*(3), 891–901. https://doi.org/10.1109/JSTARS.2013.2284528

Zhang, J. (2010). Multi-source remote sensing data fusion: Status and trends. *International Journal of Image and Data Fusion*, *1*(1), 5–24. https://doi.org/10.1080/19479830903561035

Zhang, K. (2010). Analysis of non-linear inundation from sea-level rise using LIDAR data: a case study for South Florida. *Climatic Change*, *106*(4), 537–565. https://doi.org/10.1007/s10584-010-9987-2

Zhang, X., Yamaguchi, Y., Li, F., He, B., & Chen, Y. (2017). Assessing the Impacts of the 2009 / 2010 Drought on Vegetation Indices , Normalized Difference Water Index , and Land Surface Temperature in Southwestern China. *Advances in Meteorology*, *2017*(Article ID 6837493), 9. https://doi.org/https://doi.org/10.1155/2017/6837493

Zheng, H., Song, W., & Satoh, K. (2010). Detecting long-range correlations in fire sequences with Detrended fluctuation analysis. *Physica A: Statistical Mechanics and Its Applications*, *389*(4), 837–842. https://doi.org/10.1016/j.physa.2009.10.022

Zhou, L., Tucker, C. J., Kaufmann, R. K., Slayback, D., Shabanov, N. V., & Myneni, R. B. (2001). Variations in northern vegetation activity inferred from satellite data of vegetation index during 1981 to 1999. *Journal of Geophysical Research: Atmospheres*, *106*(D17), 20069–20083. https://doi.org/10.1029/2000JD000115

Zhu, W., Pan, Y., He, H., Wang, L., Mou, M., & Liu, J. (2012). A changing-weight filter method for reconstructing a high-quality NDVI time series to preserve the integrity of vegetation phenology. *IEEE Transactions on Geoscience and Remote Sensing*, *50*(4), 1085–1094.

Zhu, Z., Wang, S., & Woodcock, C. E. (2015). Improvement and expansion of the Fmask algorithm: Cloud, cloud shadow, and snow detection for Landsats 4-7, 8, and Sentinel 2 images. *Remote Sensing of Environment*, *159*, 269–277. https://doi.org/10.1016/j.rse.2014.12.014